galaxies

MDPI

Review

Convective Boundary Mixing in Main-Sequence Stars: Theory and Empirical Constraints

Evan H. Anders [1,*,†] and May G. Pedersen [2,3,†]

[1] Center for Interdisciplinary Exploration and Research in Astrophysics (CIERA), Northwestern University, 1800 Sherman Ave, Evanston, IL 60201, USA
[2] Sydney Institute for Astronomy, School of Physics, University of Sydney, Sydney, NSW 2006, Australia
[3] Kavli Institute for Theoretical Physics, Kohn Hall, University of California, Santa Barbara, CA 93106, USA
* Correspondence: evan.anders@northwestern.edu
† These authors contributed equally to this work.

Abstract: The convective envelopes of solar-type stars and the convective cores of intermediate- and high-mass stars share boundaries with stable radiative zones. Through a host of processes we collectively refer to as "convective boundary mixing" (CBM), convection can drive efficient mixing in these nominally stable regions. In this review, we discuss the current state of CBM research in the context of main-sequence stars through three lenses. (1) We examine the most frequently implemented 1D prescriptions of CBM—exponential overshoot, step overshoot, and convective penetration—and we include a discussion of implementation degeneracies and how to convert between various prescriptions. (2) Next, we examine the literature of CBM from a fluid dynamical perspective, with a focus on three distinct processes: convective overshoot, entrainment, and convective penetration. (3) Finally, we discuss observational inferences regarding how much mixing should occur in the cores of intermediate- and high-mass stars as well as the implied constraints that these observations place on 1D CBM implementations. We conclude with a discussion of pathways forward for future studies to place better constraints on this difficult challenge in stellar evolution modeling.

Keywords: stellar evolution (1599); stellar evolutionary models (2046); stellar convection zones (301); stellar cores (1592); hydrodynamical simulations (767); star clusters (1567); apsidal motion (62); asteroseismology (73); stellar oscillations (1617); binary stars (154)

Citation: Anders, E.H.; Pedersen, M.G. Convective Boundary Mixing in Main-Sequence Stars: Theory and Empirical Constraints. *Galaxies* **2023**, *11*, 56. https://doi.org/10.3390/galaxies11020056

Academic Editors: Jorick Sandor Vink, Dominic Bowman and Jennifer Van Saders

Received: 10 February 2023
Revised: 15 March 2023
Accepted: 20 March 2023
Published: 14 April 2023

1. Introduction

Convection occurs in all main-sequence stars, and there is broad agreement that widely used prescriptions such as the mixing length theory (MLT, ref. [1], discussed in Section 1 in this series) adequately describe many properties of bulk convection in stellar interiors. There is, however, a great deal of disagreement and uncertainty regarding how to model the boundaries of convection zones, where the stellar stratification changes from being convectively unstable to stable. Convective boundaries exist at radial coordinates where the buoyant force changes sign (from acceleration to deceleration [2]), but most models and MLT unphysically assume that the convective velocity vanishes at these locations. The true boundary of a convection zone—the location where the convective velocity is zero—lies beyond the traditional "convective boundary," and some parameterization of "convective boundary mixing" (CBM) is generally employed alongside MLT to allow convective motions to extend outside of the MLT convection zone.

While low-mass stars are fully convective, stars such as the Sun with masses $0.35M_\odot \lesssim M_* \lesssim 1.2M_\odot$ develop stable interiors and turbulent convective envelopes [3–5]. Convective motions can "undershoot" from the unstable envelope into the stable interior and cause mixing, which can alter surface lithium abundances [6–8] and the sound speed below the convection zone [9–11]. In "massive stars" with masses $M_* \gtrsim 1.1M_\odot$, efficient nuclear burning from the CNO cycle destabilizes the core to convection, while the envelope

becomes convectively stable [5,12]; some of these stars also have opacity-driven convection zones near the surface [13,14]. CBM from the core convection zone injects fresh hydrogen fuel into the high-temperature central burning region of the star, thereby extending the stellar lifetime and increasing the size of the helium core at the end of the main sequence. Unfortunately, observations cannot be uniformly explained with one standard CBM prescription [15], leading to uncertainty in how to include CBM in stellar evolution calculations. These uncertainties are not subtle: evolving a 15 $M_{\odot}$ model using differing mixing prescriptions can significantly alter the main sequence lifetime by $\sim$25% and the helium core mass by $\sim$40%, with consequences that ripple beyond the main sequence, such as in determining what type of remnant the star eventually leaves behind [16,17]. Fortunately, there seems to be a tight relationship between a star's core mass, its envelope mass, and its core composition if the star is to remain in equilibrium [18], which may limit the range of feasible CBM prescriptions to characterize.

Observations of massive stars cannot be explained without CBM, which increases the convective core size compared to "standard" stellar models. For example, radial profiles of the Brunt-Väisälä frequency measured via asteroseismology demonstrate substantial mixing outside the standard core boundary [19]. The population of observed eclipsing binaries [20] and the width of the main sequence in the temperature–luminosity plane observed in stellar clusters [21–24] can be partially explained by introducing a mass-dependent CBM into stellar models. Simulations of 3D turbulent convection whose initial conditions are based on 1D stellar evolution models consistently report significant entrainment at convective boundaries and expansion of the convection zone (e.g., [25–31]), so the picture from numerical simulations aligns with that inferred from observations.

In this review, we discuss CBM in stars. Our goals in writing this review are:

1. To provide context for investigators who need to employ CBM in their own studies.
2. To summarize past works and provide launching points for future studies aimed at improving CBM prescriptions.
3. To facilitate communication between observers, 1D modelers, and 3D numericists.

In Section 2, we describe 1D parameterizations of CBM. In Section 3, we describe the results of numerical simulations exhibiting CBM. In Section 4, we describe observations and empirical calibrations of CBM. We conclude with a discussion in Section 5.

2. Theoretical (1D) Parametrizations

2.1. How Does CBM Modify Stellar Evolution?

In stellar evolution software instruments, the mixing caused by convection, CBM, and other mixing processes are generally parameterized as a turbulent diffusivity [32]. That is, for some chemical composition (e.g., hydrogen, X), time evolution is assumed to follow,

$$\partial_t X = \nabla \cdot [(D_{\rm conv} + D_{\rm CBM} + D_{\rm other}) \nabla X], \quad (1)$$

when changes to the composition from nuclear reactions are ignored. Here, each D is a diffusion coefficient. In this formalism, it is impossible to distinguish between CBM and other mixing processes which could occur in the vicinity of a convective boundary (e.g., shear, rotation, etc.). This formalism generally allows us to probe the shape and magnitude of the radial profile of mixing but not the fundamental process at work. Regardless, within this review, we will assume that excess mixing which connects to and extends beyond the convective boundary are convection-induced CBM processes. We additionally limit the scope of this review to purely hydrodynamical CBM processes, complicating effects of, e.g., magnetism or radiative transfer are not considered.

In Figure 1, we briefly demonstrate how CBM affects the evolution of stars with convective cores. Panel a shows that increasing the radial extent of mixing beyond the convective boundary (going from light to darker lines) decreases a star's effective temperature (panel b) and increases its luminosity (panel c) at the TAMS (terminal-age main sequence). This increased mixing also increases the length of the main sequence (panel d) by providing

more fuel and significantly increases the helium core mass at the end of the main sequence (panel e); these latter changes introduce uncertainty into the star's post-main-sequence evolution and into the eventual remnant that the star leaves behind. While not pictured here, vectors in the mass–luminosity plane can help disentangle the effects of mass loss and internal mixing on the evolutionary tracks of very massive stars [22,24]. The slope of the vector is set by the mass-loss rate, while the length of the vector is set by the age and internal mixing; see Figure 1 in Higgins and Vink [24]. If the star's rotational velocity is known, the CBM parameter can be directly derived from the length of the vector.

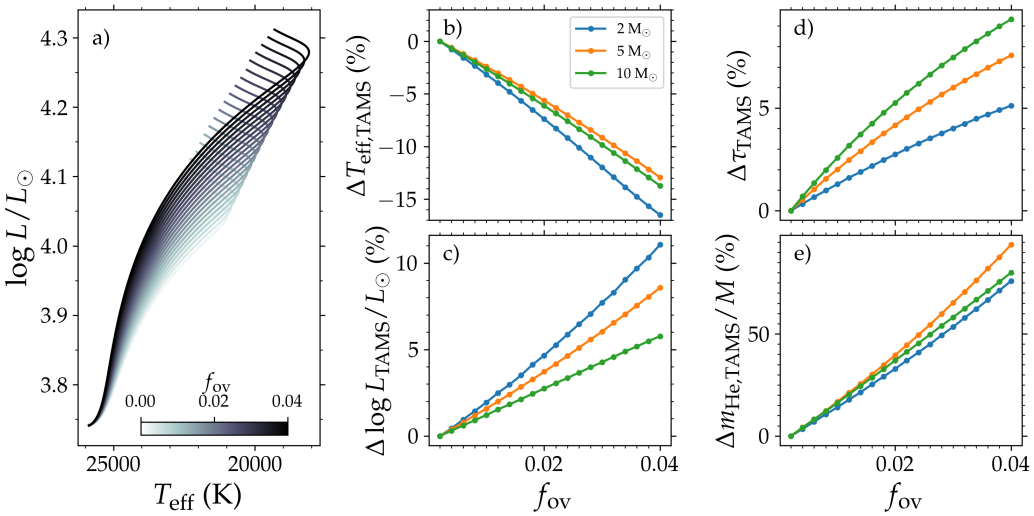

Figure 1. Illustration of the effect of increasing the size of the CBM region assuming exponential diffusive overshoot. (**a**) HR diagram showing the evolutionary tracks for a 10 $M_\odot$ star with different extents of the CBM region. $f_{ov} = 0.002$ is a low value, whereas $f_{ov} = 0.04$ is considered a high value for this parameter. (**b**) Percentage change in the effective temperature at the TAMS compared to the $f_{ov} = 0.002$ case for three different initial masses. The f_{ov} parameter sets the extent of the CBM region and how rapidly the mixing decreases with distance from the convective core boundary; see Section 2.4. (**c**) Same as (**b**) but for the luminosity at the TAMS. (**d**) Same as (**b**) but for the age at the TAMS. (**e**) Same as (**b**) but for the helium core mass obtained at the TAMS. Figure made by the authors using `MESA` models. `MESA` inlists and data used to generate the figure are available on Zenodo [33].

2.2. Convective Boundaries

In 1D stellar evolution software instruments, convection zone boundaries coincide with a sign change in a determinant $\mathcal{Y}$ ([34], Section 2). We define regions with $\mathcal{Y} < 0$ to be stable to convection. The simplest convective stability criterion is the Schwarzschild criterion,

$$\mathcal{Y}_S \equiv \nabla_{rad} - \nabla_{ad} < 0. \quad (2)$$

here, the logarithmic temperature gradient is $\nabla \equiv d \ln P / d \ln T$ (pressure P and temperature T). When ∇ is evaluated at constant entropy and mean molecular weight, its value is the adiabatic gradient ∇_{ad}. The gradient required to radiatively transport the full stellar luminosity is ∇_{rad}.

In the presence of gradients in the mean molecular weight μ, a better convective stability criterion is the Ledoux criterion,

$$\mathcal{Y}_L \equiv \mathcal{Y}_S + \frac{\chi_\mu}{\chi_T} \nabla_\mu < 0. \quad (3)$$

The Ledoux criterion includes the composition gradient $\nabla_\mu = d \ln \mu / d \ln P$, where $\chi_T = (d \ln P / d \ln T)_{\rho,\mu}$, $\chi_\mu = (d \ln P / d \ln \mu)_{\rho,T}$, and ρ is the density. The composition term is generally stabilizing when the radial gradient of μ is negative.

In this review, we are interested in cases where an unstable convection zone (CZ) with $\mathcal{Y}_{\rm L} \geq 0$ borders a stable radiative zone (RZ) with $\mathcal{Y}_{\rm L} \leq \mathcal{Y}_{\rm S} < 0$. We therefore do not consider, e.g., semiconvection or thermohaline mixing (see Chapters 2 and 3 of Garaud [35] as well as Section 3 and Figure 3 of Salaris and Cassisi [36]). We note that evolutionary timescales are much longer than the convective overturn timescale on the main sequence [37]. In this regime, both the Ledoux criterion and the Schwarzschild criterion should retrieve the same location for the convective boundary, as argued by Gabriel et al. [38] and shown using hydrodynamical simulations by Anders et al. [2]. Therefore, we will refer to the convective boundary and the Schwarzschild boundary interchangeably. The Schwarzschild boundary ($\mathcal{Y}_{\rm S} = 0$) generally corresponds to an interface where the entropy gradient goes from being marginally stable (or unstable, $\nabla s \leq 0$) to being stable ($\nabla s > 0$). "Convective boundaries" defined by $\mathcal{Y}$ therefore specify where the radial buoyancy force changes from destabilizing (in the convection zone) to stabilizing (in the radiative zone). The location where convective velocity goes to zero therefore always lies "outside" of the convective boundaries defined by $\mathcal{Y}_{\rm S}$. The CBM prescriptions that we discuss below therefore attempt in spirit to estimate the size of the region in which convective velocities decelerate beyond the convective boundary.

2.3. Internal Mixing Profiles

The time evolution of the mass fraction X_i of chemical element i depends on nuclear reactions $\mathcal{R}_i$ and mixing processes $\mathcal{M}_i$. The 1D stellar evolution software instruments typically treat element mixing as a diffusive process, so the time evolution equation is

$$\begin{aligned} \frac{\partial X_i}{\partial t} &= \mathcal{R}_i + \mathcal{M}_i, \\ &= \mathcal{R}_i + \frac{1}{\rho r^2}\frac{\partial}{\partial r}\left[\rho r^2 D_{\rm mix}\frac{\partial X_i}{\partial r}\right] + \mathcal{M}_i^{\rm micro}, \end{aligned} \tag{4}$$

where ρ is the density and r is the radius coordinate. We group extra microscopic atomic diffusion effects such as radiative levitation or gravitational settling into $\mathcal{M}_i^{\rm micro}$. The mass fraction X_i diffuses with a diffusivity of $D_{\rm mix}$ in units of $\rm cm^2\,s^{-1}$.

The sum of a variety of different physical processes such as convection, rotation, magnetic fields, and waves all contribute to $D_{\rm mix}(r)$ in different regions and at different magnitudes. We decompose the turbulent diffusivity based on whether or not convection is present,

$$D_{\rm mix}(r) = D_{\rm conv}(r) + D_{\rm CBM}(r) + D_{\rm env}(r), \tag{5}$$

where $D_{\rm conv}(r)$ is the contribution from convective regions, $D_{\rm CBM}(r)$ characterizes convective boundary mixing regions, and $D_{\rm env}(r)$ is the mixing profile in the radiative envelope. Parameterizing mixing into diffusion profiles in this way discards information about the specific processes that cause mixing, which makes it difficult to disentangle the individual mixing contributions of CBM, rotational mixing, and other processes that occur at the same radial coordinate. Examples of four $D_{\rm mix}(r)$ profiles are illustrated in the top panels of Figure 2. The associated stratification produced by these mixing coefficients is shown in the bottom panels of Figure 2.

The remainder of this section will focus on the different $D_{\rm CBM}(r)$ parameterizations that are commonly used in 1D stellar evolution codes. We use the term CBM to refer to any boundary mixing process. We adopt a terminology where convective overshoot only mixes the chemical composition so that ($\nabla_{\rm T} = \nabla_{\rm rad}$) in the CBM region, and convective penetration mixes both chemical composition and entropy so that ($\nabla_{\rm T} = \nabla_{\rm ad}$) in the CBM region.

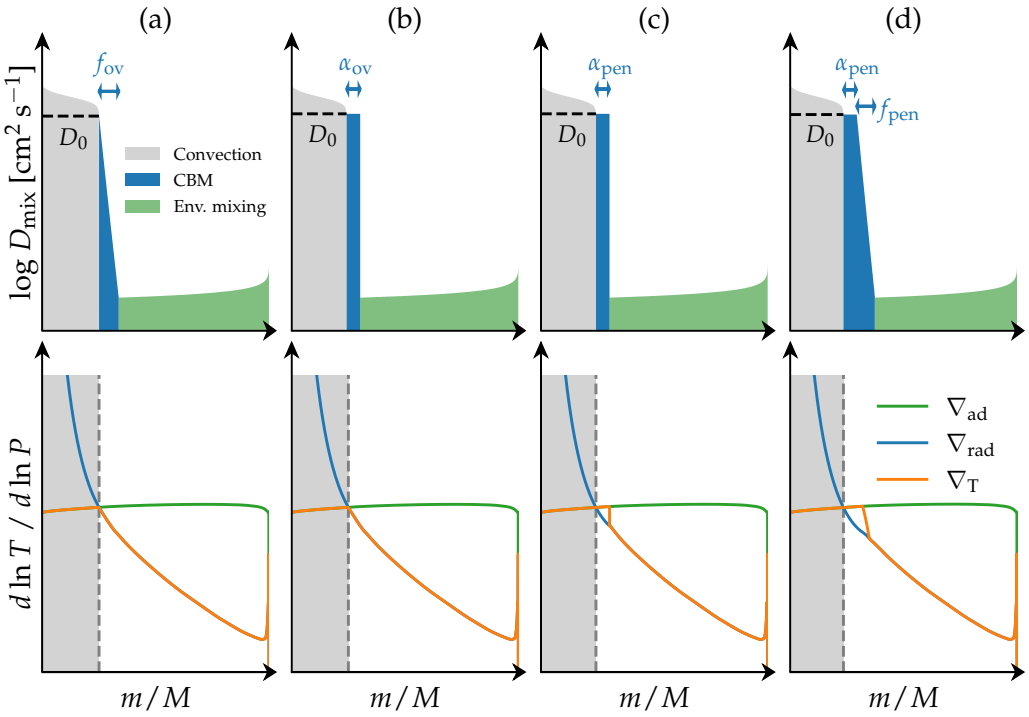

Figure 2. Illustration of four different convective boundary mixing prescriptions in 1D. Internal mixing profiles are shown in the top panels, while the corresponding temperature gradients are given in the bottom panels. (**a**) Exponential diffusive overshoot, (**b**) step overshoot, (**c**) convective penetration, and (**d**) extended convective penetration. Convective regions are indicated in gray. $D_{\rm CBM}(r)$ and $D_{\rm env}(r)$ are shown, respectively, in blue and green in the top panels. In the bottom panels, the plotted curves show the adiabatic temperature gradient (green), the radiative temperature gradient (blue), and the adopted temperature gradient (orange). Figure made by the authors using `MESA models`. The data used to generate the figure are available on Zenodo [33].

2.4. Overshoot or Overmixing

Overshooting (e.g., [39]) or overmixing (e.g., [40]) occurs when fluid motions beyond the convective boundary transport elements but not heat and thereby do not alter the temperature gradient. Two prescriptions for convective overshooting are common in 1D stellar evolution codes.

Exponential diffusive overshoot [41,42], see Figure 2a, is a 1D parameterization of results from 2D hydrodynamical simulations of surface convection zones in solar-type stars, main-sequence A-type stars, and cool DA white dwarfs. It is used by the stellar evolution code `GARSTEC` [43], and it used to be the default overshoot option in `MESA` [34,44–47]. Exponential diffusive overshoot is a mixing efficiency which decreases exponentially with distance from the convective boundary,

$$D_{\rm CBM}(r) = D_0 \exp\left[\frac{-2(r-r_0)}{f_{\rm ov} H_{\rm p,0}}\right] \qquad \text{with} \qquad \nabla_T = \nabla_{\rm rad}. \tag{6}$$

In this formalism, the free parameter $f_{\rm ov}$ determines what fraction of a pressure scale height corresponds to the the e-folding length scale of the mixing efficiency, and thereby, it indirectly sets the extent of the CBM region; CBM models based on the scale height based on the scale height have been used as long as CBM has been considered [48,49]. Here, r is the radial coordinate and H_p is the pressure scale height. The convective boundary occurs at $r_{\rm cc}$ and has scale height $H_{p,\rm cc}$, but MLT assumes that the convective velocity and mixing are both zero at $r_{\rm cc}$. As a result, the exponential diffusive overshoot is calibrated at $r_0 = r_{\rm cc} - f_0 H_{p,\rm cc}$, where f_0 is usually fixed to a value between 0.002 and 0.005. At r_0, the

convective mixing efficiency is $D_0 = D_{\rm mix}(r_0)$ and the pressure scale height is $H_{p,0}$. The mixing efficiency follows the MLT value for $r < r_0$, and it follows Equation (6) for $r \geq r_0$.[1]

Step overshoot provides a simpler mixing profile in the CBM region (see Figure 2b),

$$D_{\rm CBM}(r) = D_0 \qquad \text{for } r_0 \leq r \leq r_{\rm ov}, \qquad \text{with} \qquad \nabla_T = \nabla_{\rm rad}. \tag{7}$$

Here, the free parameter $\alpha_{\rm ov}$ determines the extent $r_{\rm ov} = r_0 + (\alpha_{\rm ov} + f_0)H_{\rm p,\,0}$ of the overshoot region which is characterized by a constant mixing efficiency D_0. This CBM formalism is adopted in the stellar evolution codes `DSEP` [50,51], `BaSTI` [52–58], `TGEC` [59,60], and `YREC` [61], and is available in `MESA`.

2.5. Convective Penetration

Convective Penetration occurs when convection mixes chemicals and entropy beyond the convective boundary [39], see Figure 2c. Convective penetration is identical to step overshoot, except the adiabatic temperature gradient is adopted in the CBM region:

$$D_{\rm CBM}(r) = D_0 \qquad \text{for } r_0 \leq r \leq r_{\rm pen}, \qquad \text{with} \qquad \nabla_T = \nabla_{\rm ad}. \tag{8}$$

Here, $r_{\rm pen} = r_0 + (\alpha_{\rm pen} + f_0)H_{\rm p,\,0}$, and $\alpha_{\rm pen}$ is the free CBM parameter. The convective penetration formalism is adopted in the stellar evolution code `GENEC` [62], and a similar option is available for the `YREC` code. We caution that the names "step overshoot" and "convective penetration" are often used interchangeably in the literature. We distinguish between the two based on the temperature gradient in the CBM region (e.g., [39,63]).

2.6. Extended Convective Penetration

Extended convective penetration [64,65] combines convective penetration and diffusive exponential overshooting; see Figure 2d. In this formalism, the convective boundary mixing region has two components. The convection zone is adjacent to a convective penetrative region with constant mixing and an adiabatic temperature gradient. Further from the convective boundary, the mixing exponentially decays and the temperature gradient gradually transitions from $\nabla_{\rm ad}$ to $\nabla_{\rm rad}$. The exact mixing coefficients are

$$\begin{aligned} D_{\rm CBM}(r) &= D_{\rm pen} && \text{for } r_0 \leq r \leq r_{\rm pen} \\ D_{\rm CBM}(r) &= D_{\rm pen} \exp\left[\frac{-2(r - r_{\rm pen})}{f_{\rm pen} H_{\rm p,pen}}\right] && \text{for } r_{\rm pen} < r \leq r_{\rm CBM}, \end{aligned} \tag{9}$$

where $H_{\rm p,pen} = H_{\rm p}(r_{\rm pen})$ and $r_{\rm CBM}$ is the radius at the outer boundary of the CBM region. The thermal stratification is [64]

$$\begin{aligned} \nabla_{\rm T} &= \nabla_{\rm ad} && \text{for } r_0 \leq r \leq r_{\rm pen} \\ \nabla_{\rm T} &= f^t(r)\nabla_{\rm ad} + \left[1 - f^t(r)\right]\nabla_{\rm rad} && \text{for } r_{\rm pen} < r \leq r_{\rm CBM}, \end{aligned} \tag{10}$$

There are two free parameters: $\alpha_{\rm pen}$ and $f_{\rm pen}$. $f^t(r)$ is a radial profile which varies from one in the convection zone to zero in the stable radiative envelope. $f^t(r)$ has been prescribed in two ways in the literature. Its first implementation was based on the amount of mass in $r_{\rm pen} < r \leq r_{\rm CBM}$ [64]. Another implementation define it as $f^t(r) = [\log Pe(r) + 2]/4$ for values of $10^{-2} < Pe < 10^2$, where the Péclet number Pe [65], which is the ratio between the time scales of the radiative and advective heat transport, can be estimated from, e.g., MLT velocities.

To our knowledge, extended convective penetration is not currently a standard option in any stellar evolution codes, but it has been studied using a modified version of `MESA` [64,65]. However, the option of changing the temperature gradient within the CBM region is available in existing codes. For example, the `ASTEC` code [66] uses the same mixing profile $D_{\rm CBM}$ as the

step overshoot and convective penetration schemes wherein mixing efficiency is considered constant for a certain distance $\alpha_{\rm CBM} H_p$ beyond the convective boundary, but `ASTEC` can smoothly vary the temperature gradient within this region [66,67].

2.7. Limiting the Extent of the CBM Region

The diffusive overshoot, convective penetration, and extended convective penetration prescriptions listed above all rely on a free CBM parameter multiplied by the pressure scale height to define the extent of the CBM region. As a result, small convective cores (with $r_{\rm cc} \to 0$ and $H_{\rm p} \to \infty$) can produce unphysically large CBM regions. This problem primarily arises in lower mass stars that start off with small convective cores on the main sequence. To circumvent this issue, some stellar evolution codes implement a mass-dependent CBM parameter which is zero at low stellar mass, constant at high mass, and smoothly increases at intermediate mass. Such an approach is partially validated by observational evidence of a relationship between CBM mixing parameters and stellar mass, but the observational evidence is ambiguous; see Section 4. Mass-dependent CBM parameters were used to compute the `YREC` Y^2 isochrones [68], the YaPSI isochrones [69], a set of isochrones computed with `GARSTEC` and used to fit the open cluster M67 [70], and a grid of stellar models with derived internal structure constants computed with `MESA` [71].

Various alternative approaches limit the size of CBM regions based on the size of the convection zone. The `ASTEC` and `Cesam2k` codes enforce that the size of the CBM region is $\beta_{\rm CBM} \times \min(r_{\rm cc}, H_{\rm p,cc})$ [66,72]. The `YREC` code defines the actual radius of the CBM region as $r_{\rm CBM} = \beta_{\rm CBM} / (H_{\rm p}^{-1} + r_{\rm cc}^{-1})$ which simplifies to $r_{\rm CBM} = \beta_{\rm CBM} H_{\rm p}$ for large convective cores [73]. The `GARSTEC` code uses a modified pressure scale height $\widetilde{H_{\rm p}} = H_{\rm p} \times \min\left[1, \left(r_{\rm cc}/H_{\rm p}\right)^2\right]$ [43,70] and as a default `MESA` uses $\beta_{\rm CBM} \times \min\left(H_{\rm p}, r_{\rm cc}/\alpha_{\rm MLT}\right)$ where $\alpha_{\rm MLT}$ is the mixing length parameter. Here, we use $\beta_{\rm CBM}$ to collectively refer to the free parameter assumed for a given CBM prescription, so it could be, e.g., $f_{\rm ov}$ or $\alpha_{\rm ov}$. A result of these constraints is that the input $\beta_{\rm CBM}$ parameter in the code can be different from the effective $\beta_{\rm CBM}$ used to set the size of the CBM region (see Ref. [73], Figures 2 and 5 for examples of this). A further problem is that inconsistent implementations between different codes produce CBM regions with different sizes even if the same $\alpha_{\rm CBM}$ parameter and CBM prescription are nominally employed. These subtle differences impede direct comparisons between results obtained using different codes when the sizes of the convective cores are small as is the case for stars around 1.2 $M_\odot$ [74].

2.8. Comparing Different CBM Parameters

In order to make comparisons between results obtained using different CBM prescriptions (e.g., exponential vs. step overshooting), a robust conversion between their input parameters must be established. Such conversions can be achieved in two ways.

The first is to compare observations to models generated using different CBM prescriptions and find the CBM parameters which best reproduce the observed diagnostics. Such comparisons have previously been achieved through, e.g., the asteroseismic modeling of the slowly pulsating B star KIC 7760680 where comparisons between results using exponential diffusive and step overshoot suggested a relation of $\alpha_{\rm ov}/f_{\rm ov} = 13.33$ for this 3.25 $M_\odot$ star [75]; see also Section 4.4. Similarly, comparisons have been made using detached, double-lined, eclipsing binary stars (see also Section 4.3). As an example, the study of 29 such systems with component masses between 1.2 and 4.4 $M_\odot$ revealed a relation of $\alpha_{\rm pen}/f_{\rm ov} = 11.36 \pm 0.22$ between models using convective penetration and exponential diffusive overshoot [76]. The comparison suggested that there is a slight dependence of this ratio on surface gravity $\log g$, metallicity Z, mass M, or effective temperature $T_{\rm eff}$. Splitting the sample in two groups depending on either the effective temperature or surface gravity resulted in $\alpha_{\rm pen}/f_{\rm ov} = 10.50 \pm 0.25$ for cooler giant stars and $\alpha_{\rm pen}/f_{\rm ov} = 11.71 \pm 0.27$ for hotter dwarf stars [76]. A similar study of 12 binary systems with component masses between 4.58 and 17.07 $M_\odot$ likewise suggests a conversion factor between $f_{\rm ov}$ and $\alpha_{\rm pen}$ larger than 10 [77][2].

Another method for deriving conversions between different CBM parameters is to directly compare models which use different CBM prescriptions. Magic et al. [70] suggested a conversion factor of $\alpha_{\rm ov}/f_{\rm ov} \approx 11$ using models with masses between 2 and 6 $M_\odot$. Noels et al. [78] compared two evolutionary tracks of a 10 $M_\odot$ star using either step overshoot or convective penetration, finding that an $\alpha_{\rm pen} = 0.175$ achieved a similar result to the step overshoot case with $\alpha_{\rm ov} = 0.2$, i.e., $\alpha_{\rm ov}/\alpha_{\rm pen} = 1.14$.

Here, we provide a comparison between models computed with the stellar structure and evolution code `MESA` v22.05.1 for a 2 $M_\odot$ and 10 $M_\odot$ star assuming (1) exponential diffusive overshoot and (2) diffusive step overshoot. Using these models, we investigate what $\alpha_{\rm ov}$ parameter is required to reproduce the same luminosity and convective core mass (m_{cc}, the mass coordinate of the Schwarzschild boundary of the convection zone) of the star with exponential diffusive overshoot at a fixed value of $f_{\rm ov}$. These comparisons are carried out at fixed main-sequence age ($X_{\rm c}/X_{\rm ini}$) and stellar mass. In other words, we look for solutions to the relations $\log L_1(X_{\rm c}/X_{\rm ini}, f_{\rm ov}) = \log L_2(X_{\rm c}/X_{\rm ini}, \alpha_{\rm ov})$ and $m_{cc,1}(X_{\rm c}/X_{\rm ini}, f_{\rm ov})/M = m_{cc,2}(X_{\rm c}/X_{\rm ini}, \alpha_{\rm ov})/M$. Here, $X_{\rm c}$ is the current core hydrogen mass fraction and $X_{\rm ini}$ is the initial hydrogen mass fraction. An example of these solutions is shown for the 10 $M_\odot$ star in Figure 3. Panels a and b show the derived relations for the luminosity and convective core mass, respectively, at different main-sequence ages indicated by the color of the lines. The black dashed curve shows the expected trend assuming the standard "rule-of-thumb" $\alpha_{\rm ov} \approx 10 f_{\rm ov}$, whereas the black dotted line shows the linear fit to the derived relations. The differences between the linear fits and relations derived at different ages are shown in panel (c) and (d), where the gray shaded region gives the $3\sigma_{\rm std}$ uncertainty regions for the relations. As seen in the figure, the relations are not strictly linear and also show a small dependence on the chosen $X_{\rm c}$ in the current core hydrogen mass fraction and $X_{\rm ini}$ value.

In summary, we find a general relation of the form

$$\alpha_{\rm ov} = A + B f_{\rm ov}. \tag{11}$$

For the 2 $M_\odot$ star, we find $A = (0.042 \pm 0.004)$ and $B = (14.11 \pm 0.25)$ when fitting for luminosity and $A = (0.036 \pm 0.01)$ and $B = (14.05 \pm 0.71)$ when fitting for core mass. For the 10 $M_\odot$ star, we find $A = (0.0256 \pm 0.0008)$ and $B = (10.75 \pm 0.04)$ when fitting for luminosity and $A = (0.0256 \pm 0.001)$ and $B = (10.74 \pm 0.05)$ when fitting for core mass. The reported errors are the $3\sigma_{\rm std}$ errors.

We note three important observations for the four relations given above. The first is that relations between $\alpha_{\rm ov}$ and $f_{\rm ov}$ for a given mass are same within the errors independently of whether they are derived based on the luminosity or the convective core mass. The second observation is that the errors on the parameters for the relations for the 2 $M_\odot$ star are larger than for the 10 $M_\odot$, implying a stronger age dependence on the relations for the 2 $M_\odot$ star. Finally, the slopes (B) of the relations are steeper for the 2 $M_\odot$ star than the 10 $M_\odot$ one and cannot be reconciled within the $3\sigma_{\rm std}$ errors, showing that the exact conversions to use are also mass dependent. We emphasize that making direct comparisons between absolute values of different CBM parameters is non-trivial. Therefore, when studying CBM and the extent of the CBM region, carrying out an ensemble study of a group of stars using the same stellar evolution code and the same CBM prescription is recommended.

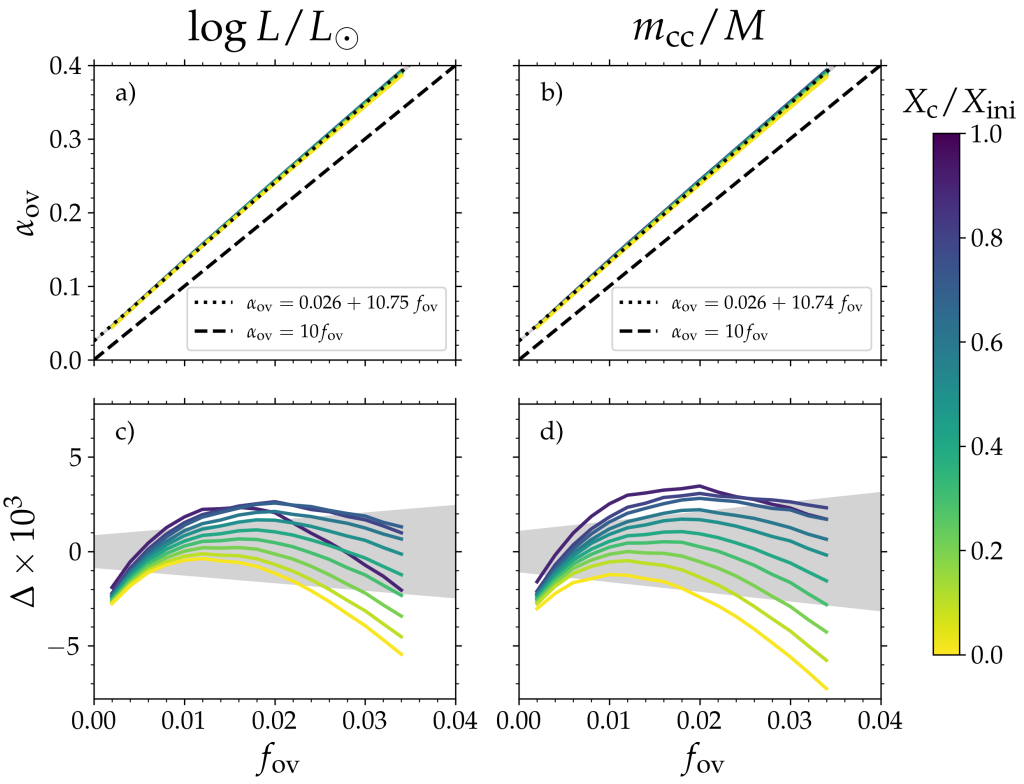

Figure 3. Derived correlations between α_{ov} and f_{ov} for a $10\,M_\odot$ star at different main-sequence ages given as X_c/X_{ini}. (**a**) The colored curves show the relation between α_{ov} and f_{ov} required to obtain $\log L_1(X_c/X_{ini}, f_{ov}) = \log L_2(X_c/X_{ini}, \alpha_{ov})$. The black dashed curve shows the expected trend assuming $\alpha_{ov} = 10 f_{ov}$, while the black dotted lines shows the combined linear fit to the colored lines. (**b**) Same as (**a**) but fulfilling $m_{cc,1}(X_c/X_{ini}, f_{ov})/M = m_{cc,2}(X_c/X_{ini}, \alpha_{ov})/M$. (**c**) Differences between the derived α_{ov} versus f_{ov} relation for a given X_c/X_{ini} and the linear fit shown by the dotted black line in panel (**a**). The gray shaded region gives the $3\,\sigma_{std}$ uncertainty region of the linear fit. (**d**) Same as (**c**) but for the comparison between the α_{ov} and f_{ov} parameters needed to obtain the same convective core masses. Figure made by the authors using `MESA` models. `MESA` inlists and data used to generate the figure are available on Zenodo [33].

2.9. The 1D Models Not Covered in This Review

A full discussion of physically motivated 1D models of CBM is beyond the scope of this review. Techniques not discussed here include CBM models based on linear or fundamental mode analysis [79–81], nonlinear modal expansion [82], models of overshooting bubbles based on local MLT [48,83], nonlocal MLT models [84–90], non-MLT multiscale models [91], "turbulent convection models" (e.g., [92,93]), Canuto's stellar mixing model (e.g., [94]), and nonlocal "turbulent kinetic energy models" (e.g., [95,96]). We briefly also note that there exist models which aim to characterize overshooting convective motions in the optically thin atmosphere of stars such as the Sun [79,97], reviewed briefly in Nordlund [86], but we focus here on convection confined to optically thick portions of the star.

In this section, we have focused on the most frequently used techniques in the stellar modeling literature; we note that these MLT-based implementations may not necessarily be logically consistent [98], but their ease of implementation and use has made them widespread in the stellar structure literature. Other local-MLT-based CBM prescriptions or profiles such as diffusive Gumbel overshooting [99,100] and diffusive double exponential overshoot [101] have been proposed, but a full discussion of them is likewise beyond the scope of this review.

3. 3D Hydrodynamical Perspectives of Convective Boundary Mixing

We now describe convective boundary mixing from its fluid dynamical roots. Many simulations have examined a convective layer interacting with a stable layer in a variety of natural contexts (e.g., stellar envelope convection, core convection, and even atmospheric convection). In order to paint the most complete picture of convective boundary mixing, we will discuss the results of these studies from a perspective that is impartial to the motivation or setup.

Hydrodynamical CBM simulations often employ simplified equation sets (e.g., the Boussinesq [102] or Anelastic [103–106] approximations[3]). For generality, we will use the equation formulation most applicable to stellar interiors, the Fully Compressible Navier–Stokes equations (ref. [107], §15 and §49), which are

$$\partial_t \rho + \nabla \cdot (\rho \boldsymbol{u}) = 0, \tag{12}$$

$$\partial_t \boldsymbol{u} + \boldsymbol{u} \cdot \nabla \boldsymbol{u} = -\frac{1}{\rho}\nabla P + \boldsymbol{g} + \frac{1}{\rho}\nabla \cdot \overline{\boldsymbol{\Pi}}, \tag{13}$$

$$\partial_t s + \boldsymbol{u} \cdot \nabla s = \frac{1}{\rho T}(\nabla \cdot (k \nabla T) + \rho\epsilon + \Phi), \tag{14}$$

where ρ is the density, $\boldsymbol{u}$ is the velocity, T is the temperature, s is the specific entropy, $\boldsymbol{g}$ is the gravitational acceleration vector, k is the radiative conductivity, and ϵ is the specific energy production rate (erg $\mathrm{g}^{-1}\,\mathrm{s}^{-1}$) from nuclear burning. The viscous stress tensor, viscous heating, and rate-of-strain tensor are, respectively, defined

$$\Pi_{ij} = 2\rho\nu\left[e_{ij} - \frac{1}{3}\nabla \cdot \boldsymbol{u}\delta_{ij}\right], \tag{15}$$

$$\Phi = 2\rho\nu\left[e_{ij}e_{ij} - \frac{1}{3}(\nabla \cdot \boldsymbol{u})^2\right] = 2\rho\nu\left[\mathrm{Tr}(\bar{e}\cdot\bar{e}) - \frac{1}{3}(\nabla \cdot \boldsymbol{u})^2\right], \tag{16}$$

$$e_{ij} = \frac{1}{2}(\nabla \boldsymbol{u} + [\nabla \boldsymbol{u}]^T). \tag{17}$$

where ν is the viscous diffusivity (kinematic viscosity). Stars are composed of magnetized plasmas, and thus, magnetohydrodynamic effects should in general be accounted for, but for simplicity, we will restrict our discussion to the hydrodynamic case in this review.

Arguments about CBM processes are often rooted in energetics. The kinetic energy equation is obtained by dotting Equation (13) with $\rho\boldsymbol{u}$ and applying Equation (12) to retrieve

$$\partial_t(\mathcal{KE} + \mathcal{PE}) + \nabla \cdot (\boldsymbol{u}(\mathcal{KE} + \mathcal{PE} + P) + \boldsymbol{u} \cdot \overline{\boldsymbol{\Pi}}) = P\nabla \cdot \boldsymbol{u} - \Phi. \tag{18}$$

Here, the kinetic energy is $\mathcal{KE} = \rho|\boldsymbol{u}|^2/2$ and the potential energy is $\mathcal{PE} = \rho\phi$, and we have assumed time invariance $\partial_t\phi = 0$ of the gravitational potential ϕ (defined from $\boldsymbol{g} = -\nabla\phi$). Equation (18) is written in conservation form, with the time derivative and divergence of energy fluxes on the left-hand side and the sources and sinks of energy on the right-hand side. An entropy equation is obtained by multiplying Equation (14) by ρ and applying Equation (12),

$$\partial_t(\rho s) + \nabla \cdot (\boldsymbol{u}\rho s) = \frac{1}{T}(\nabla \cdot (k\nabla T) + \rho\epsilon + \Phi). \tag{19}$$

We note that we could have instead multiplied by ρT to obtain the internal energy equation, but that would generally return the same constraints as the kinetic energy equation, so a different thermal energy constraint is needed.

We next take a volume integral of Equations (18) and (19) over the full convection zone and any important CBM region. We apply the divergence theorem to the flux terms

and assume that the volume we are examining is bounded by regions where $\boldsymbol{u} \approx 0$, so the integral of the fluxes can be neglected. We are left with

$$\partial_t(\langle \mathcal{KE} \rangle + \langle \mathcal{PE} \rangle) = \langle P\nabla \cdot \boldsymbol{u} \rangle - \langle \Phi \rangle, \tag{20}$$

$$\partial_t \langle \rho s \rangle = \left\langle \frac{1}{T}[\nabla \cdot (k\nabla T) + \rho\epsilon] \right\rangle + \left\langle \frac{1}{T}\Phi \right\rangle. \tag{21}$$

Equation (20) states that the evolution of the total (kinetic and potential) energy of the convection zone is determined by the fraction of $P\mathrm{d}V$ work ($\langle P\nabla \cdot \boldsymbol{u} \rangle$) that is not consumed by dissipative processes ($\langle \Phi \rangle$) on small scales.

Equation (21) forms the basis for deriving thermal scaling laws for convective regions [108,109] and also serves as a basis for the integral constraint of Roxburgh [110].

We will use this energetics framework to describe three *processes* that can occur in hydrodynamical CBM. These processes are depicted in Figure 4, and parallels can be drawn between these processes and the prescriptions in Section 2. The first process is a small-scale conversion of convective kinetic energy into potential energy beyond the boundary, which is referred to as "convective overshoot". The second is a process wherein either kinetic energy or buoyant work are used to increase the potential energy of the convection zone, which is referred to as "entrainment". The third process occurs in a statistically stationary state where $\partial_t(\langle \mathcal{KE} \rangle + \langle \mathcal{PE} \rangle) = 0$, and a balance between work producing energy and dissipation is achieved; this process is called "convective penetration". We note that there is a great deal of degeneracy in the literature studying these processes, and these terms (in particular "overshoot" and "penetration") are often used interchangeably; note that when we use these terms in this review, we are referring to distinct processes. As in the bottom panel of Figure 4, we will assume that the stellar structure consists of a convection zone (CZ, $\nabla \approx \nabla_{\mathrm{ad}} < \nabla_{\mathrm{rad}}$) and a radiative zone (RZ, $\nabla \approx \nabla_{\mathrm{rad}} < \nabla_{\mathrm{ad}}$), and that the CBM region consists of both a penetrative zone (PZ, $\nabla \approx \nabla_{\mathrm{ad}} > \nabla_{\mathrm{rad}}$) and an overshoot zone (OZ, $\nabla \approx \nabla_{\mathrm{rad}} < \nabla_{\mathrm{ad}}$). We note that the convection zone itself could also have an additional structure (e.g., "Deardorff zones", see Ref. [111]), but we do not include that level of detail here.

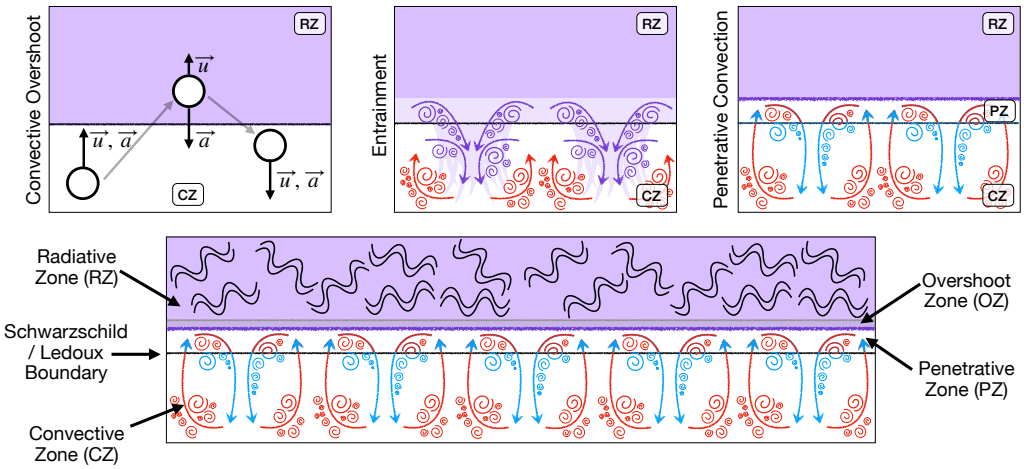

Figure 4. Three CBM processes are shown schematically in the top row. White fluid represents the well-mixed CZ, while purple fluid is the stable RZ. (Left) Convective overshoot (Section 3.2) occurs when a fluid parcel from the CZ crosses into the RZ; a positive entropy gradient in the RZ accelerates the parcel back toward the CZ. (Middle) Shear flows and overshooting motions drag RZ fluid into the CZ in a process called entrainment (Section 3.4). (Right) Convective penetration occurs when convection maintains a well-mixed region of fluid beyond the Schwarzschild boundary (Section 3.5). The bottom panel shows the structure of a statistically stationary convective boundary, which resembles the 1D "extended convective penetration" prescription (Section 2.6). This figure was originally published online under a CC BY license in Anders et al. [112].

3.1. Nondimensional Fluid Parameters

Many hydrodynamical studies of convective boundary mixing processes seek a description of how a CBM length scale or rate varies as a nondimensional fluid parameter is changed. Commonly measured nondimensional numbers are the bulk Richardson number, Ri_B, and the stiffness or relative stability, $\mathcal{S}$. These parameters compare the buoyancy stability of the RZ to how unstable or vigorous the convection is in the CZ.

The Richardson number was first examined in the astrophysical context by Meakin and Arnett [25] and is typically defined

$$\mathrm{Ri}_B = \frac{\Delta b L}{\sigma^2}, \qquad \text{with} \qquad \Delta b = \int_{r_1}^{r_2} N^2 \, dr, \tag{22}$$

where σ is the root-mean-square turbulent velocity in the convective region near the interface, N^2 is the Brunt-Väisälä frequency, L is a typical length scale for turbulent motions, and the convective interface is assumed to span some radial extent ranging from r_1 to r_2. There is degeneracy in how r_1, r_2, and L are defined in the literature.

An alternative approach is to measure the "stiffness" or "relative stability" $\mathcal{S}$ of the radiative–convective interface. This has historically been defined in two ways. Early simulations defined a structure-based $\mathcal{S}$ [113][4],

$$\mathcal{S}_{\mathrm{struct}} \approx \frac{|\nabla_{\mathrm{rad}} - \nabla_{\mathrm{ad}}|_{\mathrm{RZ}}}{|\nabla_{\mathrm{rad}} - \nabla_{\mathrm{ad}}|_{\mathrm{CZ}}}, \tag{23}$$

where the logarithmic temperature gradients are defined in Section 2.2. This definition is useful in simulations where convection is driven by an unstable temperature gradient which achieves $\nabla = \nabla_{\mathrm{rad}}$ by, e.g., an enforced boundary condition, but it is less useful in describing convection in the cores of massive stars where $\nabla \approx \nabla_{\mathrm{ad}} \ll \nabla_{\mathrm{rad}}$. Recently, a dynamical definition of the stiffness has been favored by some authors [114–116],

$$\mathcal{S}_{\mathrm{dyn}} = \frac{N^2_{\mathrm{RZ}}}{\omega^2_{\mathrm{conv}}}, \tag{24}$$

where N^2_{RZ} is the typical value of the Brunt-Väisälä frequency in the stable radiative zone and $\omega^2_{\mathrm{conv}} = [2\pi u_{\mathrm{conv}}/L]^2$ is the square angular convective frequency, where u_{conv} is the average turbulent convective velocity and L is a typical convective length scale. We then see that $\mathcal{S}_{\mathrm{dyn}} \approx \mathrm{Ri}_B$, aside from the length scales which are used. It is generally expected that stiff convective interfaces (with large values of $\mathcal{S}$ or Ri_B) should have very small CBM regions. Stellar evolution models [5] and asteroseismic inferences [117] expect the stiffness value at the core boundaries of massive stars to be very large ($\mathcal{S}_{\mathrm{dyn}} \sim 10^{6-8}$).

We also note that there is an explicit link between the Mach number $\mathrm{Ma}^2 = u^2_{\mathrm{conv}}/c_s^2$ of convection and $\mathcal{S}_{\mathrm{dyn}}$; knowledge of Ma in a convection zone therefore provides information about CBM. Take $c_s^2 = P/\rho = gH_P$ to be the sound speed in a star in hydrostatic equilibrium, where H_P is the pressure scale height and g is the gravitational acceleration. Neglecting composition gradients, and assuming $N^2 = (g/H_P)(\nabla_{\mathrm{ad}} - \nabla_{\mathrm{rad}})$ in the RZ (Equation (6.18); [118]) and $\omega_c^2 = [2\pi u_{\mathrm{conv}}/H_P]^2$ in the CZ, it can be shown that

$$\mathcal{S}_{\mathrm{dyn}} = \mathrm{Ma}^{-2} \frac{(\nabla_{\mathrm{ad}} - \nabla_{\mathrm{rad}})_{\mathrm{RZ}}}{(2\pi)^2}. \tag{25}$$

Anders et al. [116] recently introduced a new "penetration parameter" $\mathcal{P}$ to the zoo of parameters that describe CBM. The extent of an adiabatic penetration zone is assumed to be determined by the magnitude of the negative buoyant work performed within this zone [39,110]. Therefore, a luminosity (or flux) based parameter can be defined [116],

$$\mathcal{P} = -\frac{(L_{\mathrm{rad}} - L_{\mathrm{ad}})_{\mathrm{CZ}}}{(L_{\mathrm{rad}} - L_{\mathrm{ad}})_{\mathrm{RZ}}}, \tag{26}$$

where the numerator (CZ) is averaged over some part of the convective zone and the denominator (RZ) is averaged over some part of the region that would be a radiative zone if not for convective penetration. Here, $L_{\rm ad}$ is the radiative luminosity that would be carried if the stratification were adiabatic $\nabla = \nabla_{\rm ad}$, and $L_{\rm rad}$ is the radiative luminosity that would be carried if the stratification were $\nabla = \nabla_{\rm rad}$. Since $(L_{\rm rad} - L_{\rm ad})_{\rm RZ} < 0$, $\mathcal{P} > 0$ always. Large penetrative regions are expected when $\mathcal{P}$ is large. There is an implicit link between the penetration parameter and the structural relative stability parameter, $\mathcal{P} \sim \mathcal{S}_{\rm struct}^{-1}$. It therefore makes sense that simulations (e.g., [119,120]) see negligible penetration when they use $\mathcal{S}_{\rm struct} \gg 1$. Note that the dependence of convective penetration on $\mathcal{P}$ or $\mathcal{S}_{\rm struct}$ is why we distinguish between $\mathcal{S}_{\rm struct}$ and $\mathcal{S}_{\rm dyn}$. Many simulations are set up in such a manner that $\mathcal{S}_{\rm struct} \sim \mathcal{S}_{\rm dyn}$; however, stars can have $\mathcal{P} \sim \mathcal{S}_{\rm struct} \sim 1$ and $\mathcal{S}_{\rm dyn} \gg 1$ simultaneously.

We finally note that studies dating back to Zahn [39] and Hurlburt et al. [113] ponder the importance of the Péclet number on CBM (e.g., [63,119,121–124]). The Péclet number measures the ratio of the thermal diffusion timescale to the convective overturn timescale,

$$\mathrm{Pe} = \frac{\tau_{\rm therm}}{\tau_{\rm conv}} = \frac{u_{\rm conv} L}{\chi_{\rm rad}}, \tag{27}$$

where $\chi_{\rm rad}$ is the radiative diffusivity of the fluid. The associated argument suggests that CBM regions have an adiabatic penetration zone where Pe is large as well as a "thermal adjustment layer" where Pe ~ 1. The size of the CBM region is expected to scale like $\mathcal{S}_{\rm struct}^{-1}$ for the adiabatic penetration zone and like $\mathcal{S}_{\rm struct}^{-1/4}$ for the thermal adjustment layer [113]. While these scalings were observed by early simulations (e.g., [125,126]), they have not appeared in more recent simulations [119,120]. Main-sequence convection is very turbulent with bulk Pe $\gg 1$ [5], so it is hard to imagine that a large thermal adjustment layer should appear at the radial location where convective flows have damped to the point of becoming laminar (Pe ~ 1).

3.2. Convective Overshoot

Convective overshoot is a process which occurs on the scale of an individual convective flow when the flow traverses the convective boundary. We define the convective boundary as the location where the entropy gradient becomes positive. In the bulk convection zone, buoyancy forces act in the expected sense (low entropy blobs accelerate upwards and high entropy blobs accelerate downwards). Beyond the convective boundary, buoyancy forces act in the opposite sense and motions become wave-like (low entropy blobs are accelerated downwards and vice versa). A "hot" upflow in the convection zone therefore accelerates downward after passing the convective boundary. This wave-like restoring motion of a convective parcel beyond the convective boundary is convective overshoot. Convective overshoot is visualized in Figure 5.

Convective overshoot occurs in all simulations which include a convection zone bordered by a radiative zone. First seen by Hurlburt et al. [127], many studies have observed overshooting and have generally sought to understand how it depends on Pe and $\mathcal{S}_{\rm struct}$ (e.g., [113,119,120,128–132]). Others sought to understand how the imposed convective flux determined the depth of overshoot [125,133,134].

Recently, an energetics-based model of convective overshoot has emerged. This model is laid out in Korre et al. [135], Equations (30)–(35), and it is also described in Lecoanet et al. [114]. They argue that a convective blob passing the convective boundary will overshoot adiabatically until the parcel's kinetic energy is converted into potential energy. This argument was presented in the context of a simplified Boussinesq model; here, we briefly recreate it in the context of the fully compressible Equations (12)–(14). The conversion of kinetic energy into gravitational potential energy occurs through the action of buoyant work,

$$\frac{1}{2}\rho_{\rm CB} u_{\rm conv}^2 = \int_{r_{\rm CB}}^{r_{\rm CB}+\delta_{\rm ov}} F_{\rm buoy}\, dr \sim \delta_{\rm ov} \left\langle F_{\rm buoy} \right\rangle, \tag{28}$$

where ρ_{CB} is the density near the convective boundary, u_{conv} is the bulk convective velocity, r_{CB} is the radial location of the convective boundary, δ_{ov} is the overshoot distance, and F_{buoy} is the radial component of the buoyancy force. In the limit of low-Mach number flows applicable to core convection or deep envelope convection on the main sequence [5], and for an ideal gas [136], the buoyant force in this limit becomes

$$\boldsymbol{F}_{buoy} = -\rho \boldsymbol{g} \frac{s}{c_p}, \tag{29}$$

where s is the specific entropy and c_p is the specific heat at constant pressure. The buoyant force near the convective boundary for a parcel traveling adiabatically is approximately

$$\left\langle F_{buoy} \right\rangle \sim \int \rho \frac{g}{c_p} \frac{ds}{dr} dr = \int \rho N^2 dr. \tag{30}$$

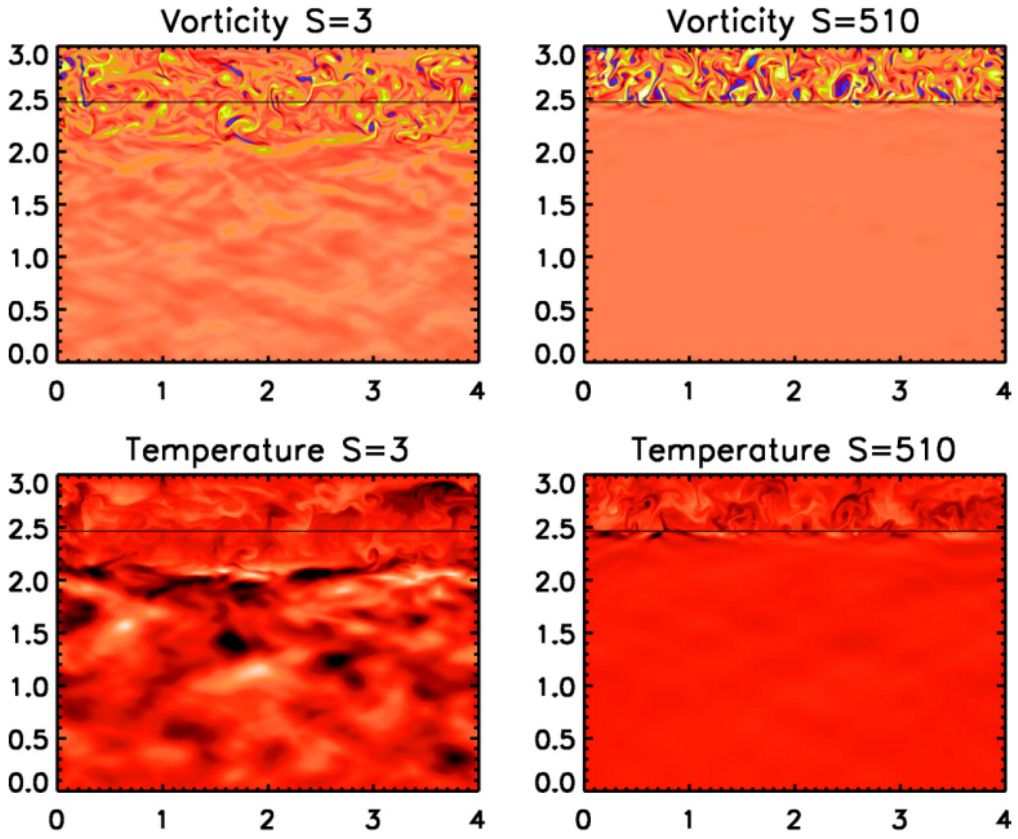

Figure 5. The vorticity (top) and temperature (bottom) are shown for simulations whose values of $\mathcal{S}_{struct}$ are small (left) and large (right). The black line marks the Schwarzschild boundary of the simulations. Note that increasing $\mathcal{S}$ decreases the depth to which dynamics overshoot beyond the Schwarzschild boundary. Note also that as stiffness increases, the internal gravity wave amplitude in the stable region decreases with respect to the convection amplitude. Figure 2 of Rogers and Glatzmaier [120]; © AAS. Reproduced with permission.

Assuming that the density is roughly the background density and does not vary sharply near the convective boundary provides

$$\frac{1}{2} \rho_{CB} u_{cz}^2 \sim \delta_{ov} \rho_{CB} \int N^2 dr. \tag{31}$$

Dividing by a characteristic length scale L, $\rho_{\rm CB}$, and $\Delta b = \int N^2 dr$ provides

$$\frac{\delta_{\rm ov}}{L} \sim {\rm Ri}_B^{-1}, \tag{32}$$

i.e., the overshoot depth is inversely proportional to the Richardson number or similarly the dynamical stiffness $\mathcal{S}_{\rm dyn}$. Korre et al. [135] take this argument one step further for a more direct comparison with simplified models of overshoot in convective simulations. They derive how they expect the overshoot distance to scale with $\mathcal{S}_{\rm dyn}$. For a stratification near the convective boundary such as $N^2 = N_0^2 (r - r_{\rm cb})^\alpha$ (where $r_{\rm cb}$ is the radial coordinate of the convective boundary), they evaluate Δb and rearrange Equation (31) to find

$$\Delta b = \frac{N_0^2}{1+\alpha} \frac{\delta_{\rm ov}^{1+\alpha}}{L^\alpha} \;\Rightarrow\; \frac{1+\alpha}{2} \frac{u_{\rm cz}^2}{L^2 N_0^2} \sim \left(\frac{\delta_{\rm ov}}{L}\right)^{2+\alpha} \;\Rightarrow\; \left(\frac{\delta_{\rm ov}}{L}\right) \sim \mathcal{S}_{\rm dyn}^{-1/(2+\alpha)}. \tag{33}$$

So, e.g., for a simulation where N^2 is a constant above the convective boundary, $(\delta_{\rm ov}/L) \sim \mathcal{S}_{\rm dyn}^{-1/2}$, and for a simulation where it increases linearly, it should scale as $(\delta_{\rm ov}/L) \sim \mathcal{S}_{\rm dyn}^{-1/3}$, which is the case examined by Lecoanet et al. [114]. A stratification which is well approximated by $N^2 \sim r^2$ in a small region outside of the convection zone would therefore reproduce the $\mathcal{S}^{1/4}$ observed by early simulations [113,119].

We note briefly that one fairly robust result from the literature of overshooting convection is that overshoot depths are almost universally seen to decrease as $\mathcal{S}_{\rm struct}$ (and $\mathcal{S}_{\rm dyn}$) increases. One exception is the recent result of Cai [132], who observed that convective exit velocities increased in the very high $\mathcal{S}_{\rm struct}$ regime, which in turn produced increasing overshoot depths; the process which would drive these increased velocities is not clear.

3.3. Convective Overshoot as Turbulent Diffusion

Overshooting has been incorporated into 1D stellar evolution models by parameterizing convective mixing using a diffusivity profile (see Section 2.3). An exponential diffusive profile was observed in the early simulations of Freytag et al. [41]; this profile was adopted by Herwig [42], and this has been the standard choice in the field ever since. More recently, Jones et al. [28] found that an exponential turbulent diffusivity described the turbulent diffusion measured in their simulations well. Herwig et al. [137] have noted that convective velocities start to fall off before reaching the CZ boundary, which complicates the implementation of this exponential diffusivity. Separately, Lecoanet et al. [114] see a fast decrease of turbulent diffusivity outside of their convection zone, but they argue that it is better parameterized as step overshooting (Section 2.4).

We note that there are two separate questions which must be answered to robustly describe convective overshoot as a turbulent diffusivity. First, how do the convective velocities decrease beyond the convective boundary? Korre et al. [135] find that the kinetic energy is well defined by a Gaussian beyond the convective boundary (e.g., their Figure 4), while Pratt et al. [99] use extreme value statistics to characterize the maximum depth that convective plumes overshoot to at any point in time, and they find their results best described by a Gumbel distribution ($\exp(-\exp(-x))$). Once the velocity profile beyond the convective boundary is understood, we must then ask how the velocity profile relates to the mixing produced by overshooting convection.

3.4. Entrainment

Entrainment is the process by which convection "scrapes" material from an adjacent stable layer into the convective region and then mixes that material. Entrainment is caused by multiple processes (e.g., splashing from convective overshoot or shear instabilities driven by horizontal convective flow [138]); for simplicity, we consider entrainment to be any process accompanied by a measurable mixing of the mean radial entropy or chemical profile at the convective boundary. Energetically, entrainment occurs when convection

exerts buoyancy work on the adjacent stable fluid. This work raises the potential energy of a portion of the adjacent fluid enough to dislodge it and drag it into the convecting region.

The earliest entrainment studies examined a stable, linear composition gradient which was destabilized by heating from below, resulting in the emergence of a convection zone which grows by entrainment. This simple setup has been studied both in the lab and numerically for the past 60 years [139–146]. These studies proposed and observed a $E \propto \mathrm{Ri}_B^{-1}$ relationship, where $E = u_e/u_t$ is the entrainment efficiency, u_e is the entraiment velocity (the rate at which the convective boundary advances) and u_t is the turbulent convective velocity [141]. These studies measured the height of the convective boundary vs. time $h(t)$ and found generally $h(t) \propto t^{1/2}$ (e.g., [139,143,146]) or $h(t) \propto t^{1/3}$ [141]. Entrainment has also been observed and studied in other simulations of Boussinesq convection bounded by a stable region; these studies further established the dependence of the entrainment rate on Ri_B or $\mathcal{S}$ [115,147].

More recently, Meakin and Arnett [25] introduced the concept of turbulent entrainment into studies of stellar astrophysics. They perform 3D hydrodynamic simulations of stellar convection using stellar structure models as initial conditions and find significant turbulent entrainment and advancement of the convective boundary (see Figure 6). They find that the entrainment efficiency follows a power law scaling of $E = A\mathrm{Ri}_B^{-n}$, where $A \sim 10^{-1}$–10^{-2} and $n \approx 1$, which is well in line with previous geophysical studies. These results have been corroborated by many hydrodynamical studies over the past decade (e.g., [26,28,31,148–150]), typically finding power laws with $n \approx 1$ and $A \in [10^{-2}, 1]$ (see Figure 7). These results have inspired Staritsin [151] and Scott et al. [152] to include power-law implementations of turbulent entrainment into stellar models, but they find that the entrainment law calibrated to simulations leads to the entire star being engulfed by the convection zone on evolutionary timescales. They do find decent agreement with other forms of boundary mixing using $A \sim 10^{-4}$, but to date, no dynamical simulations have revealed a value of A this small.

We interpret the state of the astrophysical entrainment literature as follows. Stellar models *underestimate* the size of convection zones consistently. As a result, when stellar models are used as initial conditions for 3D hydrodynamical simulations, significant turbulent entrainment is observed as the convecting regions expand to an equilibrium size. Unfortunately, most simulations are not long enough to observe the equilibrium sizes of convecting regions, so the saturation size of convective zones is uncertain. Anders et al. [2] studied a simulation under the Boussinesq approximation in which the Ledoux and Schwarzschild criteria initially disagree regarding the location of the convective boundary. Convection entrains material at the Ledoux boundary until the two criteria agree, after which point entrainment stops. Unfortunately, we are unaware of any studies which both employ the fully compressible equations and allow the size of the convection zone to fully saturate through entrainment, so these findings should be confirmed in more complex setups.

One may ask if entrainment should be included in standard stellar evolution models, just like exponential and step overshoot prescriptions. We believe that a precise implementation of entrainment is not necessary during the main sequence or other phases of evolution where the evolutionary timescale is very long compared to the entrainment rate [2]. However, proper entrainment implementations will improve stellar evolution calculations of short-lived phases of evolution where the size of convection zones are changing rapidly and where time-dependent convection implementations are necessary [153].

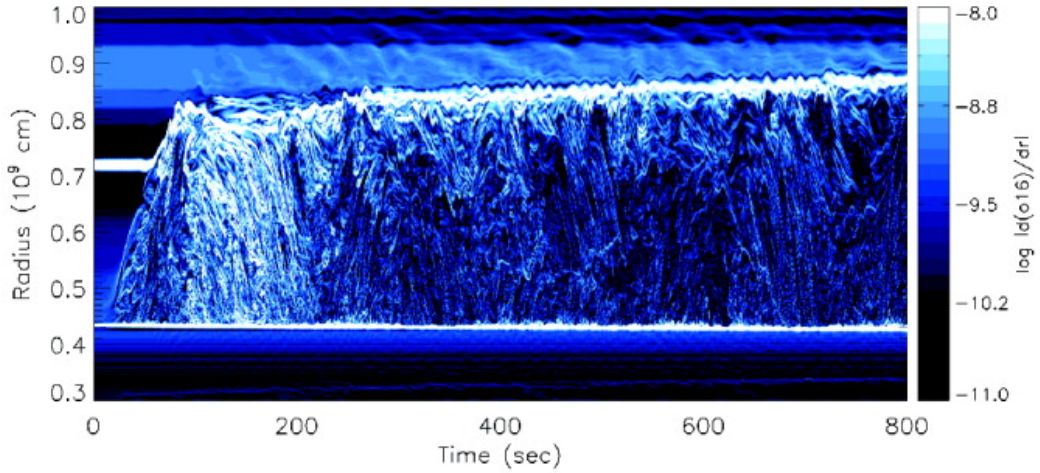

Figure 6. Data are from a hydrodynamical simulation of an oxygen-burning shell; radial coordinate is on the y-axis and time coordinate is on the x-axis. Color shows the radial gradient of the oxygen concentration profile at each time; the thick bright lines denote the top and bottom boundaries of the convective region. Turbulent convection occurs at times $t \gtrsim 50$, and entrainment causes measurable movement of the convective boundary. Figure 4 of Meakin and Arnett [25]; © AAS. Reproduced with permission.

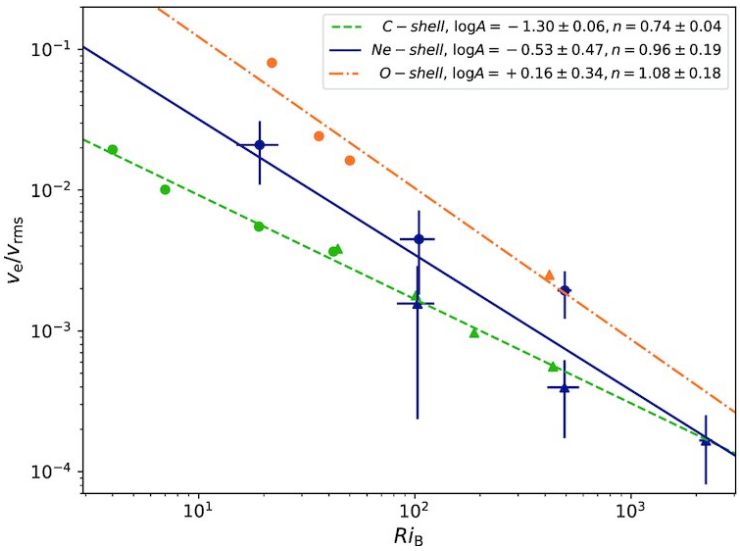

Figure 7. Entrainment rate is plotted against the bulk Richardson number for simulations of neon burning shells [31], oxygen burning shells [25], and carbon burning shells [150]. Entrainment laws ARi_B^{-n} with $A \sim (0.05, 1)$ and $n \sim 1$ are reported. Figure 5 of Rizzuti et al. [31]; © Oxford University Press. Reproduced with permission.

3.5. Convective Penetration

The boundary of a well-mixed convective region can advance by entrainment significantly beyond the Schwarzschild boundary. When this occurs, we refer to the process as convective penetration, which is characterized by a nearly adiabatic and chemically homogeneous region which is part of the convection zone but which is characterized by $\nabla_{rad} < \nabla_{ad}$.

Convective penetration was hypothesized by Roxburgh and Zahn [39,110,154,155], but it has been elusive in simulations and experiments. The hallmark of penetrative convection is mixing of the entropy gradient beyond the Schwarzschild boundary. Entropy mixing beyond the initial convective boundary has often been reported [113,119,120,123,126,156,157],

but it is often unclear if the reported process is convective penetration or if it is movement of the Schwarzschild boundary by entrainment. Another hallmark of penetrative convection is substantial negative convective flux (and excess radiative flux) beyond the Schwarzschild boundary; this is frequently observed [99,121,127,158,159] but also often seen in studies of non-penetrative overshooting convection.

Unfortunately, studies aimed at understanding convective penetration have found inconsistent or contradictory results regarding how penetration depends on, e.g., $\mathcal{S}$ or Ri_B. Early studies [113,158] suggested that penetration and $\mathcal{S}_{\mathrm{struct}}$ were linked at low values of $\mathcal{S}_{\mathrm{struct}}$ (a regime that produces a dynamical $\mathcal{S}_{\mathrm{dyn}}$ which is not relevant for core convection, see Couston et al. [115]), but later studies [119,120] found no link between $\mathcal{S}_{\mathrm{struct}}$ and convective penetration. However, many simulations have found that penetration lengths can depend on the magnitude of energy fluxes [125,133,134,160,161].

Robust evidence of convective penetration in numerical simulations was observed by Anders et al. [116] in 3D Cartesian and Baraffe et al. [162] in 2D spherical simulations. The dynamics of penetrative convection are shown in the top two panels of Figure 8. The thermal structure of a convective region with a penetration region is shown in the bottom left panel of Figure 8. The extent of the penetration region scales strongly with the penetration parameter $\mathcal{P}$, as shown in the bottom right panel of Figure 8.

Convective penetration occurs in the stationary state, so Equation (21) becomes

$$-\left\langle \frac{1}{T}\left(\nabla(k\nabla T)+\rho\epsilon\right)\right\rangle = \left\langle \frac{1}{T}\Phi\right\rangle. \tag{34}$$

This can be rearranged into the integral constraint of Roxburgh [110,154,155],

$$\int_V -(F_{\mathrm{tot}}-F_{\mathrm{rad}})\frac{1}{T_0^2}\frac{dT_0}{dr}dV = \int_V \frac{\Phi}{T_0}dV, \tag{35}$$

where F_{tot} is the total flux, F_{rad} is the radiative flux, and T_0 is the temperature stratification. We follow Anders et al. [2] and break up constraint integrals into a CZ (convective zone) and PZ (penetrative zone) portion. Noting that $F_{\mathrm{conv}} = F_{\mathrm{tot}} - F_{\mathrm{rad}}$, and that $dT_0/dr < 0$, we obtain

$$\int_{\mathrm{CZ}} F_{\mathrm{conv}}\left|\frac{1}{T_0^2}\frac{dT_0}{dr}\right|dV = \int_{\mathrm{CZ}}\frac{\Phi}{T_0}dV + \left[-\int_{\mathrm{PZ}} F_{\mathrm{conv}}\left|\frac{1}{T_0^2}\frac{dT_0}{dr}\right|dV + \int_{\mathrm{PZ}}\frac{\Phi}{T_0}dV\right]. \tag{36}$$

The left-hand side (LHS) of Equation (36) is a buoyant "engine" which quantifies the buoyant work completed by the convection in the bulk CZ. In a energetically stationary state, this positive work must be balanced out by the terms on the right-hand side (RHS) of the equation. We note that in an adiabatically mixed PZ, where $\nabla \approx \nabla_{\mathrm{ad}}$ but $\nabla_{\mathrm{ad}} > \nabla_{\mathrm{rad}}$, radiation carries too much flux $F_{\mathrm{rad}} > F_{\mathrm{tot}}$, so $F_{\mathrm{conv}} < 0$ is required for equilibrium. Therefore, all terms on the RHS of Equation (36) are positive and contribute to consumption of the LHS work. We therefore see that either dissipation is highly efficient in the convection zone, or a penetrative region characterized by negative buoyant work is required to achieve energy conservation. Zahn [39] noted that the size of a penetrative region is controlled by how drastically ∇_{rad} departs from ∇_{ad} in the PZ. This intuition appears mathematically here: a rapid departure where $\nabla_{\mathrm{rad}} \ll \nabla_{\mathrm{ad}}$ (small $\mathcal{P}$) leads to a large negative F_{conv}, so only a small PZ is required for balance in Equation (36). A very gradual departure where $\nabla_{\mathrm{rad}} \sim \nabla_{\mathrm{ad}}$ (large $\mathcal{P}$) leads to $F_{\mathrm{conv}} \sim 0$ in the PZ, and so its size is set by the turbulent dissipative properties of the convection.

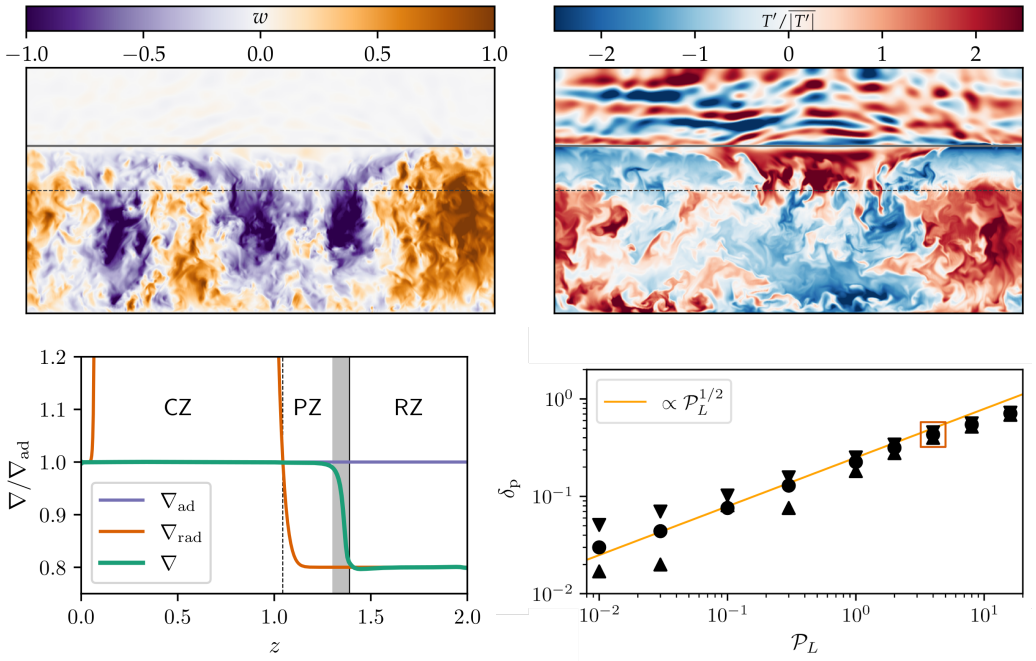

Figure 8. A snapshot in time of a 3D hydrodynamic simulation is displayed in the upper two panels with the velocity (left) and scaled temperature anomaly (right) shown. The Schwarzschild boundary is shown as a dashed line, and height where ∇ departs from $\nabla_{\rm ad}$ is plotted as a thick horizontal line. Note in the upper right panel that hot CZ upwellings turn cold in the penetration zone between the dashed and solid lines. (Bottom left) The time and horizontally averaged ∇ profiles from a simulation such as the one in the top panel; a distinct convection zone (CZ), nearly adiabatic penetration zone (PZ), overshoot zone (gray shaded region) and radiative zone (RZ) are seen. (Bottom right) The extent of the PZ is plotted against the penetration parameter, with the expected scaling overplotted in orange; $\mathcal{P}$ is found to be the most important parameter for determining the size of the PZ. Figure 1 (upper two panels), Figure 2 (bottom left panel) and part of Figure 7 (bottom right panel) are from Anders et al. [116]; these figures were originally published online under a CC BY license.

We note that it is unintuitive for dissipation (Φ) to play an important role in astrophysical convection, where viscosities are very small. In turbulent flows, the so-called "zeroth law of turbulence" states that energy which is injected into a turbulent cascade at large scales must eventually be dissipated at small scales. Therefore, the rate of turbulent dissipation is not determined by the magnitude of viscosity but rather by the rate of energy transfer from the largest eddies into the cascade, which scales something like U^3/ℓ ([163], Section 6.1.1). We also note that astrophysical convection occurs in a magnetized plasma, where additional dissipation processes (e.g., Ohmic dissipation) complicate this picture, but a full discussion of this work is beyond the scope of this review. We simply note that dissipation is expected to be substantial, and this has been shown in direct numerical simulations (e.g., [158,164,165]), although a satisfying model for the magnitude of viscous dissipation in astrophysical convection has not yet been created. This is an idea that appears both in the literature of convective penetration and in the other fields such as gravity wave mixing [96], and it should be examined in more detail.

3.6. Rotational Constraint and Magnetic Pumping

In this review, we focused on results from hydrodynamical (not magnetohydrodynamical), nonrotating fluid simulations. All stars rotate, and this rotation often strongly influences convective dynamics [5]. It is generally believed that rotation should *decrease* the extent of CBM (although it may create, e.g., meridional circulations which themselves separately increase mixing). There is evidence that rotation increases the dissipation in convective flows [166–168], which would decrease the extent of a penetration zone; analytic work

by Augustson and Mathis [100] also predicts that rotation should decrease the extent of penetration zones. Brummell et al. [119] find that rotation decreases overshoot, while Dietrich and Wicht [130] find that only $\mathcal{S}$ affects overshoot and not rotation. Browning et al. [121] studied 3D rotating core convection and found prolate penetration zones aligned with the rotation axis, which is consistent with the local box simulations of Pal et al. [169], who found less penetration at the equator than at the poles. The effects of magnetism are even less studied, but convection can pump magnetic fields out of the convection zone and into CBM regions; this process was discovered by Drobyshevski and Yuferev [170] and has been observed in simulations [171,172]; magnetic pumping has been suggested as a mechanism for solar active region formation [173] and has been used to study the structure of the Sun's magnetic field below the convection zone [174]. The manner in which rotation and magnetism affect CBM remains unclear, and future studies should explore the importance of these effects on each of the processes discussed in this review.

4. Empirical Calibrations

4.1. Stellar Clusters

Early observational inferences on CBM dating back to 1971 come from the studies of the old open cluster M67. Both Racine [175] and Torres-Peimbert [176] reported that the observed gap above the main-sequence turnoff could not be reproduced by isochrones computed with standard models [176]. A hook is seen in the isochrone at the main-sequence turnoff and the rapid evolution caused by hydrogen exhaustion results in a gap in the number of stars observed above the turnoff. By including CBM in the models, Prather and Demarque [49] demonstrated that this hook and hence gap can persist to much greater ages and thereby explain the observed gap in M67. Similar discrepancies between observations and standard model predictions were found around the same time for the open clusters NGC 752 [177] and NGC 2420 [178]. For the latter cluster, an update in the adopted opacity tables remained insufficient to explain the gap, and the inclusion of CBM in the models was required [179]. In comparison, Maeder and Mermilliod [180] considered a sample of 34 open clusters, finding that the inclusion of CBM is required to explain the extension of the core-hydrogen burning phase beyond the theoretical sequence predicted by standard models.

Several additional open and globular clusters have been studied in detail to investigate whether CBM is required to explain their morphology and distribution of stars in the color-magnitude diagram (CMD) (e.g., NGC 3680 [181], IC 4651 [182], NGC 2164 [183], NGC 1831 [184], NGC 1866 [185], NGC 6134 [186], NGC 2173 [187], SL 556 [187], NGC 2155 [187], NGC 1783 [188], NGC 419 [189]). Meaningful inferences on the CBM from these types of studies requires non-cluster and binary members to be properly identified [182,190]. Isochrones including CBM improve model agreement with observations for these clusters. The inclusion of improved opacity tables in the models generally tends to decrease the amount of required CBM, and in some cases, it may be sufficient to explain the observations without requiring any additional CBM [191].

Demarque et al. [68] were some of the first to consider a mass-dependent CBM in the calculation of model isochrones. The Y^2 isochrones included a gradual increase in the CBM parameter up to a critical mass above which a constant value was assumed, finding good fits to the observed CMDs of the seven considered open clusters including M67. However, the need for CBM is not unambiguous. Michaud et al. [192] argued that no CBM is required to reproduce the observed CMD of either M67 or NGC 188 if microscopic diffusion is included in the models. A similar conclusion for M67 was later found by Viani and Basu [193].

A similar mass-dependent CBM to the one adopted by Demarque et al. [68] has since been included in other isochrones such as the `PARSEC` isochrones [194], while others such as the `MIST` isochrones [195,196] adopt a single value for the CBM parameter. Recently, Johnston et al. [197] introduced the concept of an isochrone cloud, which shows what an isochrone would look like if the internal mixing were allowed to vary on a star-by-star basis without assuming, e.g., a mass-dependent CBM. In this case, the isochrone is no longer

a thin line but fans out for masses with convective cores. Same age models with higher mixing will be less evolved due to the extended main-sequence lifetime and define the blue edge of the isochrone cloud, whereas models with less mixing will be further evolved and therefore have lower temperatures corresponding to the red edge of the isochrone cloud; see Figure 3 of Johnston et al. [198]. The isochrone clouds were later used to model two younger stellar clusters showing extended main-sequence turnoffs (eMSTOs) [198]. eMSTOs are a broadening of the main-sequence of a cluster near its turn-off for $M \gtrsim 1.4\,M_{\odot}$, and they are common in young and intermediate age clusters (e.g., [199,200]). Age spreads [201], binary interactions [202], rotation [203], and variations in CBM [204] have been suggested as possible explanations for the eMSTOs. Spectroscopic observations focusing on measuring projected rotational velocities, $v \sin i$, of stars in the eMSTO have shown in recent years that the spread appears to coincide with a spread in $v \sin i$ amongst the stars, with faster rotating stars being redder and cooler than those with lower projected rotational velocities [205–209]. These observations suggest that rotation is the dominant effect behind the eMSTO, and that the eMSTO is caused by the combined effects of gravity darkening [210,211], where rotation causes the equators of the stars to be cooler than the poles, and there is a spread in inclination angles. Lipatov et al. [212] recently provided a tool for accounting for these effects in the model isochrones. Note that the effects on the positions of the stars in the CMD caused by gravity darkening and spreads in inclination angles are opposite to those caused by internal mixing, where faster rotating stars are expected to have higher amounts of internal mixing. Knowing the inclination angles of the stars could help disentangling the relative importance of these different effects on the morphology of the eMSTO.

4.2. Apsidal Motion

Apsidal motion, the change in the position of the periastron of a binary orbit, provides direct evidence of the internal density concentration of the stars in the binary system [213]. Measurements of Apsidal motion are based on the calculation of the apsidal constant k_j ($j = 2, 3, 4$), which is also known as the density or internal structure constant. From an observational standpoint, only the second-order apsidal motion constant k_2 is usually important [214], and it takes on a value of $k_2 = 0.75$ for a homogeneous density distribution [213,214]. In reality, rather than deriving the individual component apsidal constants, one instead works with a weighted average value $\overline{k_2}$ of the two binary components [214].

Figure 9a illustrates how the size of the CBM region affects $\log k_2$ throughout the main-sequence evolution for three different initial stellar masses. The decrease in $\log k_2$ during the main-sequence evolution is caused by the fusion of hydrogen to helium, resulting in the stars becoming more centrally condensed as they evolve. Aside from CBM, changing the opacity and metallicity of the models likewise changes the predicted k_2 values [215]; see panel b of Figure 9. Stellar rotation also impacts the derived k_2 values by making the stars more centrally condensed [216]. Finally, both CBM and stellar winds lead to more centrally condensed models but impact the stellar luminosities differently by making the models more (less) luminous when CBM (mass loss) is included [214].

The binary system Spica (α Virginis) is one of the first systems where the measured apsidal motion constants implied a need for CBM to reconcile models with observations [217,218]. Initial studies of this system showed that the observed luminosities and effective temperatures could be matched to the models by varying the initial mass and helium content, but the predicted apsidal constant was a factor of two too high compared to the observed value. Including CBM allowed L, $T_{\rm eff}$, and k_2 to simultaneously be reconciled. However, the use of different opacity tables could potentially reconcile these quantities without CBM [216]. Further constraints could potentially be obtained by studying the primary star, which is a known β Cep pulsator. While the oscillations of this star have previously been studied using both photometry and spectroscopy [219–224], no detailed asteroseismic modeling has so far been achieved. Given that the primary β Cep star has been selected as a priority 1A target for the future asteroseismic CubeSpec space mission [225], this might change in the future.

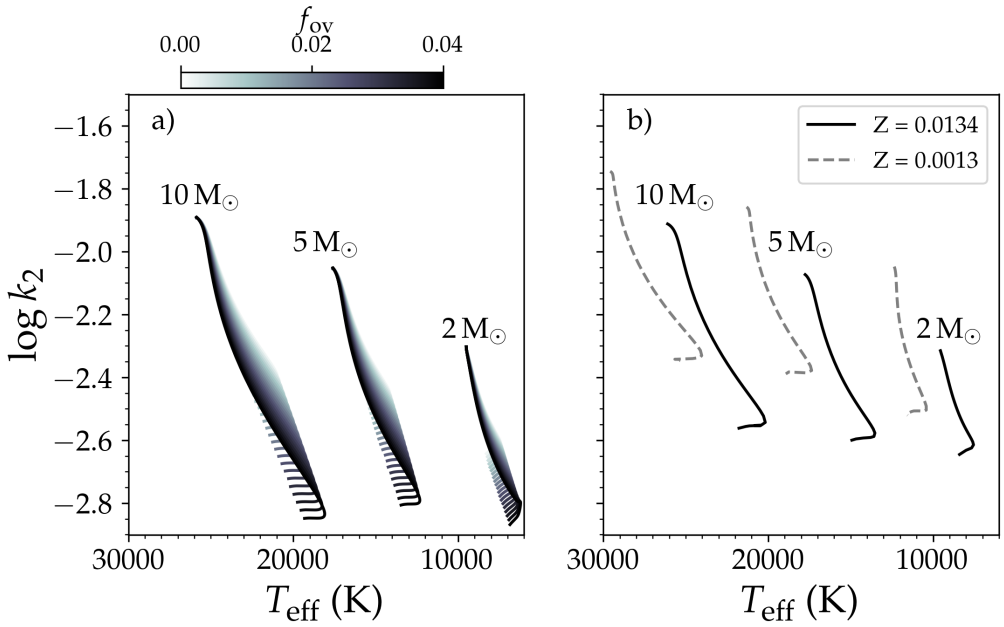

Figure 9. Evolution of the apsidal constant k_2 for three different initial stellar masses. (**a**) Variation in k_2 resulting from varying the extent of the CBM region assuming exponential diffusive overshoot and a fixed initial chemical composition of $X = 0.71$, $Y = 0.276$, and $Z = 0.014$. (**b**) Variation in k_2 resulting from changing the initial metallicity of the stars, assuming a mass-dependent CBM [71]. Figure made by the authors using `MESA` models (panel **a**) and pre-existing model grids by Claret [71] (panel **b**). `MESA` inlists and data used to generate panel (**a**) are available on Zenodo [33].

The need for CBM to reconcile the observed apsidal constants with theoretical values is not unambiguous. Claret and Gimenez [226] studied 14 eclipsing binaries in the mass range of 1.5–23 $M_\odot$ and showed that a rotation correction to k_2 could reconcile the observed and theoretical values. For the binary system PV Cas, however, the inclusion of rotation was insufficient to reconcile the observed and theoretical k_2 values [227]. Several studies which employ a single value of the CBM parameter for all masses find good agreements between modeled and observed apsidal motion constants within the observational errors (e.g., [228–234]), while others find the theoretical values to be either larger (e.g., [229,234–237]) or smaller (e.g., [230,238,239]) than observations. More recent studies rely on model grids where a mass-dependent CBM was assumed (see Section 4.3.1), and they find good agreement between theory and observations [240]. A few studies have tried to optimize the CBM parameters of individual binary components based on the apsidal constant. One such study of 27 double-lined eclipsing binaries found good agreement with a predetermined mass-dependent overshooting.[5] The only outlier was the moderately evolved, high mass ($M_1 \approx 14\,M_\odot$, $M_2 \approx 11\,M_\odot$) system V453 Cyg, where more CBM was favored. This is not the only example of systems requiring higher CBM parameters. The study of the apsidal motion of the high mass binary system V380 Cyg indicated the need for a high overshooting parameter of $\alpha_{ov} \approx 0.6 \pm 0.1$ for the primary component [242], although the errors on the estimate were later suggested to be larger [243]. Finally, a separate study of two massive, eccentric binary systems in the open cluster NGC 6231 required enhanced internal mixing either from CBM or turbulent diffusion to reconcile the theoretical apsidal constants with the observed values [244].

4.3. Mass Discrepancy

The mass discrepancy problem is a disagreement between spectroscopically derived stellar masses[6] and those obtained from stellar evolution models. This disagreement appears on the HR diagram because stars and their expected evolutionary tracks do not overlap [245,246]. Derived spectroscopic masses are systematically lower than evolutionary

masses (see Figure 10a), hinting toward missing or inadequate physics in the standard stellar structure and evolution models used. In stellar binaries, the mass discrepancy is a disagreement between dynamically derived component masses and evolutionary masses from standard models when a common age is enforced (see Figure 10b). This problem was first seen for the binary systems SZ Cen [182,247], BW Aqr [248], and BK Peg [248], where the inclusion of CBM is needed in order to obtain satisfactory fits to the more massive components of the systems. These early studies did not consider a difference in CBM parameters between the components of the systems.

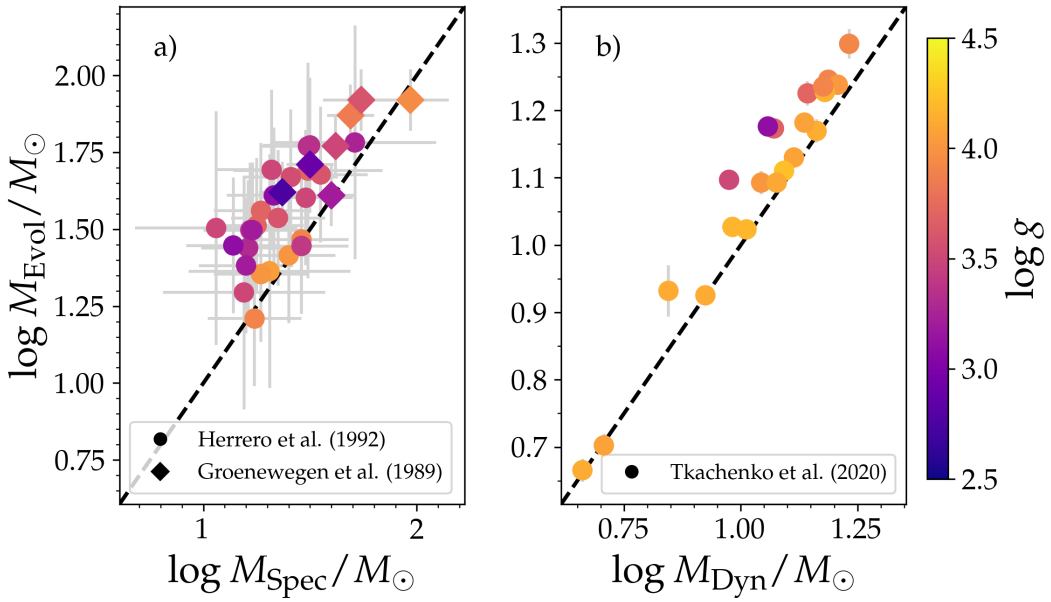

Figure 10. Examples of observed mass discrepancies. Better agreement between both $M_{\rm Evol}$-$M_{\rm Spec}$ and $M_{\rm Evol}$-$M_{\rm Dyn}$ is generally found for less evolved stars. (**a**) Observed mass discrepancy between spectroscopic (x-axis) and evolutionary (y-axis) masses derived for a sample of 32 high-mass stars [245,246]. Similar errors to those for $M_{\rm Spec}$ were assumed for $M_{\rm Evol}$ for the round data points. (**b**) Observed mass discrepancy between dynamical (x-axis) and evolutionary (y-axis) masses derived for a sample of 11 double-lined eclipsing binaries [77]. Errors on the measurements are typically smaller than the size of the data points. Figure made by the authors using data from Groenewegen et al. [245], Herrero et al. [246], and Tkachenko et al. [77].

Large CBM parameters (primary $\alpha_{\rm ov} = 0.3$–0.5; secondary $\alpha_{\rm ov} = 0.1$–0.4) derived from vectors in the mass–luminosity plane were found for the high-mass ($M_1 = 39.5\,{\rm M}_\odot$, $M_2 = 33.5\,{\rm M}_\odot$) detached eclipsing binary system HD166734 [22]. These stars are blue supergiants (BSGs), and explaining the population of BSGs is a long-standing problem for stellar structure and evolution theory. The area in the HR diagram where the BSGs are found is expected to be scarcely populated due to rapid post-MS stellar evolution, but the opposite is observed [249]. There are two likely explanations for this: (1) the main sequence is extended compared to standard models and BSGs are core-hydrogen-burning stars, or (2) BSGs are post-MS stars undergoing core helium burning. The mass–luminosity plane inference of high CBM parameters suggests that most blue supergiants (BSGs) are on the main sequence close to the TAMS [24]. However, the fact that BSGs are slow rotators ($v \sin i \leq 50\,{\rm km\,s^{-1}}$) compared to hotter massive stars with $v \sin i \lesssim 400\,{\rm km\,s^{-1}}$ seemingly supports the core helium burning scenario, because rotational velocity should decrease after the main sequence as the stellar envelope expands [250]. This expansion is tied to the star's $\log g$ value, and Brott et al. [251] used $\log g$ values to calibrate the CBM parameter at $16\,{\rm M}_\odot$, finding $\alpha_{\rm ov} = 0.335$. However, the drop from $v \sin i \approx 400\,{\rm km\,s^{-1}}$ to $\leq 50\,{\rm km\,s^{-1}}$ coincides with the effective temperature of ≈22,000 K, where rotational braking due to

enhanced mass loss may occur [252]. Such braking requires a CBM parameter $\alpha_{ov} \geq 0.335$ to occur at masses as low as $10\,M_{\odot}$.

Another binary system which suggests the importance of CBM is V380 Cyg. The primary component's mass discrepancy is extreme and may be in excess of 10–30% [77,242,253,254]. One solution to this problem is to use a CBM parameter of $\alpha_{pen} = 0.6 \pm 0.1$ for the primary component, with no CBM required to reconcile the less evolved near-ZAMS secondary component [242]. Recent updated component parameters show that a discrepancy also exists for the secondary component, which can be fixed by decreasing the metallicity and increasing the mass of the star within its 3σ error [254]. For the primary component, a mass at the 3σ limit combined with a high rotation ($v_{ZAMS} = 241\,km\,s^{-1}$) and strong level of CBM ($\alpha_{pen} = 0.6$) was required to reconcile the evolutionary models with the observations [254]. Another complication is that the primary has high microturbulence velocity ($\xi = 15\,km\,s^{-1}$), and neglecting this in the spectroscopic analysis causes the effective temperature to be overestimated by ≈1700 K (≈8%)[7] [77]. This would likewise impact the derived T_{eff} of the secondary both from spectroscopic disentangling and photometric analysis of the light curve. Appropriately accounting for the effect of microturbulence in the spectroscopic analysis in combination with the inclusion of CBM could fully explain the mass discrepancy of this system. Such an analysis has yet to be carried out.

In comparison to the four binary systems discussed above, excellent fits to the observations were found for the binary systems V792 Her [255], AI Phe [256], and UX Men [257] using standard models without CBM. These systems cover the mass range 1.2–1.5 $M_{\odot}$, whereas the more massive components of SZ Cen, BW Aqr, BK Peg, and V380 Cyg have masses between 1.43 and 11.43 $M_{\odot}$. These seven systems provide some indication that a mass dependence may exist for CBM.

4.3.1. A Search for Mass-Dependent CBM Using Binary Systems

Detached double-lined eclipsing binaries (DDLEB) provide great test beds for stellar structure and evolution models. The component masses, radii, and effective temperatures of DDLEBs can be precisely and accurately measured, and the components can reasonably be assumed to share a common age and composition. The advantage of using DDLEBs over single stars can clearly be seen from a comparison of the errors between panels a and b in Figure 10.

The largest sample of DDLEBs that have been used to investigate the presence of a mass dependence of CBM consists of 50 systems (100 stars) in the mass range of 1.2 to 4.4 $M_{\odot}$ [258]. For all of these systems, the masses and radii are known to a 3% accuracy or better, while the effective temperatures are known to a 5% accuracy. An ensemble study of these stars revealed that the extent of the CBM region appears to be steadily increasing with mass from 1.2 to 2 $M_{\odot}$ and reaches a plateau that persists up the upper limit of the mass in the sample of 4.4 $M_{\odot}$; see gray data points in Figure 11. The associated by-eye fit to the data [20] is shown by the solid blue line in Figure 11, while an earlier result by the same authors for a smaller sub-sample of 33 DDLEBs and where convective penetration was used instead of exponential diffusive overshoot is indicated by the orange dotted line [258]. The switch from using convective penetration to exponential diffusive overshoot was mainly a result of a change in the adopted stellar structure and evolution codes, and it also allowed for derivation of a relation $\alpha_{pen}/f_{ov} = 11.36 \pm 0.22$ [76] that could be used to perform a conversion between the two CBM parameters; see also Section 2.8. The small offset between the orange dotted and solid blue line in Figure 11 for $M > 2\,M_{\odot}$ is caused by differences in the assumed primordial helium abundance [76].

One of the first studies of DDLEBs where a mass-dependent CBM was investigated relied on a sample of three ζ Aurigae systems (wide eclipsing binaries where the primary component is a late-type bright giant or supergiant) and three related non-eclipsing binaries also containing an evolved primary component [259]. As indicated in Figure 1, the effects of CBM on evolutionary tracks become more pronounced as stars age, so these systems

were suggested as ideal test beds for CBM. The size of the CBM region was found to slightly increase with mass from ≈0.24 $H_{p,cc}$ at 2.5 $M_\odot$ to ≈0.32 $H_{p,cc}$ at 6.5 $M_\odot$; see the yellow dotted curve in Figure 11. Ribas et al. [260] relied on a sample of eight DDLEBs with masses between 2 and 12 $M_\odot$, and they likewise found an increase in the extent of the CBM region with mass but with a steeper slope for the increase toward higher masses; see the black dashed line in Figure 11. This latter result was largely guided by V380 Cyg, which was one out of only two systems in the sample with masses above 3.4 $M_\odot$. Like the studies mentioned above, a large CBM parameter $\alpha_{ov} \approx 0.6$ was found for this system, whereas a lower $\alpha_{ov} \sim 0.2$–0.5 was needed for the similar mass system HV 2274. An age dependence of the CBM parameter was suggested as a possible solution to this difference in α_{ov}. Ribas et al. [260] also used data from prior studies of lower mass stars for the construction of their mass versus CBM relation partly shown by the black dashed line in Figure 11. A similar study with a significant overlap (eight out of 13) in the considered sample of DDLEBs with masses between 1.35 and 27.27 $M_\odot$ also arrived at a mass-dependent CBM but with a much shallower slope for stars with masses above ≈2 $M_\odot$ [261]; see the green dashed–dotted curve in Figure 11. In this case, the errors on the derived CBM parameters are large, and the CBM–mass relation is therefore ambiguous.

If BSGs are core-hydrogen-burning stars, their distribution in the HR diagram provides some evidence for a mass-dependent CBM. Castro et al. [21] provided the first observational spectroscopic HR diagram[8] of massive stars in the Milky Way, and they compared the main-sequence density distributions to non-rotating model grids with two values of the CBM parameter. They find evidence of the CBM increasing from $\alpha_{ov} = 0.1$ at 8 $M_\odot$ to $\alpha_{ov} = 0.335$ at ≈15 $M_\odot$, and a larger α_{ov} is needed for higher masses. The inclusion of rotation in their models still showed that CBM is required, but mass dependence is not unambiguous.

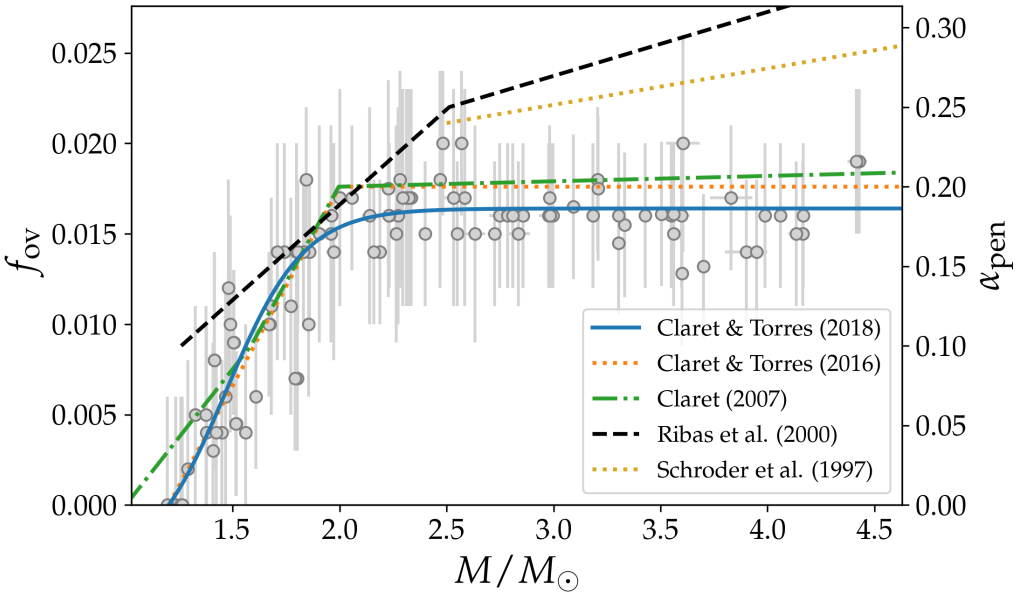

Figure 11. Inferred mass versus CBM obtained for a sample of 50 DDLEBs (gray points with errors) [262] compared to different empirical relations available in the literature obtained from modeling different samples of DDLEBs. Conversion factors of $\alpha_{pen}/f_{ov} = 11.36$ [76] and $\alpha_{pen}/\alpha_{ov} = 1$ were assumed for the inclusion of the individual curves in the figure. The plotted range is limited to the mass range of the 50 DDLEBs. Errors of $\sigma_{f_{ov}} = 0.006$ were assumed for main-sequence stars, while $\sigma_{f_{ov}} = 0.004$ were used for giants [262]. Figure made by the authors using data from Claret and Torres [262], Claret and Torres [20], Claret and Torres [76], Claret and Torres [258], Claret [261], Ribas et al. [260], and Schroder et al. [259].

4.3.2. Evidence against Mass-Dependent CBM and Complications

The detection of a mass-dependent CBM relying on ensembles of DDLEBs is not unambiguous, and the reliability of the result has been questioned in several cases. Costa et al. [263] studied an earlier sample of 38 out of the 50 DDLEBs mentioned above, using stellar models including both CBM and rotational mixing and applied a Bayesian analysis to investigate the mass dependence of CBM [263]. Due to the wide scatter and large errors on the derived CBM parameters, the authors do not find a clear mass dependence on the CBM but rather identify a wide distribution of valid CBM parameters between ≈0.15 and 0.4 $H_{p,cc}$ for $M > 1.9\,M_\odot$, which is contrary to the constant value shown for the solid blue and dotted orange curves in Figure 11. They suggest that the distribution could be explained using models with a constant CBM parameter $\alpha_{ov} = 0.2$ and initial rotational velocities between 0 and 80% break-up velocity. Constantino and Baraffe [264] analyzed a different subset of eight representative systems out of the 50 DDLEBs to determine whether or not the derived CBM parameters for each system are unique. They found that the uncertainties on the derived f_{ov} values are high and a single value of the CBM parameter could be used for the entire mass range of 1.3–3.7 $M_\odot$. No mass dependence on the CBM was found, but the results did indicate that CBM was needed for $M > 2\,M_\odot$. The derived uncertainties may be too pessimistic, as this work did not take into account additional constraints available from including the effective temperatures in the analysis [262]. Uncertainties could be further reduced if more precise effective temperatures and metallicities were obtained [264].

Meng and Zhang [265] considered a sample of four eclipsing binary systems relying on a CBM formalism that did not use the pressure scale height to determine the extent of the CBM region, and they found no CBM dependence on the mass in the range 1.2 to 2.5 $M_\odot$. Stancliffe et al. [266] also found no CBM dependence on mass or metallicity for their sample of nine eclipsing binaries with M = 1.3–6.2 $M_\odot$ using both exponential diffusive overshoot and a non-traditional CBM formalism where an adjustment was made directly to the Schwarzschield criterion based on the ratio between the radiation and gas pressure and a free CBM parameter [266]. A more recent study relied on a sample of 11 DDLEBs with M= 4.6–17.1 $M_\odot$ where the fundamental and atmospheric parameters were all derived using the same methodology in contrast to the ensemble studies mentioned above [77]. No mass dependence on the CBM parameter was found for this sample, but the observed mass discrepancy could be explained by a combination of a need for higher core masses and the lack of proper treatment of microturbulent velocities in the spectroscopic analysis of the stars.

Discussions dating back more than 30 years argue that in order to constrain helium abundances, opacity tables, mixing length and/or CBM parameters, the binary star parameters must be known to accuracies of at least 1% (for radii), 2% (for mass and temperature), and 25% (for metallicity) [267]. These numbers have been backed up by more recent statistical studies on using binary systems to constrain CBM. Valle et al. [268] argue that systems with masses between 1.1 and 1.6 $M_\odot$ where both components are on the main sequence cannot be used to calibrate CBM when the errors on the component masses are appropriately accounted for. The only exception is when the primary is in the last 5% of its main-sequence evolution. This study assumed errors on the effective temperature, metallicity, component masses, and radii of 100 K, 0.1 dex, 1%, and 0.5% respectively. The observed biases and uncertainties are reduced when the errors on observed parameters are reduced. In comparison, a similar statistical analysis using the more evolved binary system TZ Fornacis ($M_{primary} = 2.057 \pm 0.001\,M_\odot$, $M_{secondary} = 1.958 \pm 0.001\,M_\odot$) found that good constraints on CBM could be obtained, owing to the low errors on the component masses [269]. Biases were also found from a subsequent statistical analysis assuming a $M = 2.50\,M_\odot$ primary star in three different post-main-sequence evolutionary stages and a $M = 2.38\,M_\odot$ secondary [270]. However, differentiating between cases of no and mild CBM is generally possible, unless the primary is undergoing central helium burning. For the 50 DDLEBs in Figure 11, 59% of the component masses are known to better than a 1% accuracy, while for 20% and 2% of the stars, the masses are known to a 0.5% and 0.1%

accuracy, respectively. The errors on the component masses were not taken into account when deriving the CBM parameters for the 50 DDLEBs in Figure 11, but the metallicity was allowed to vary within the observed errors [20,76,262].

The results of the statistical analyses mentioned above seem backed up by earlier attempts at studying CBM using 49 DDLEBs, which found that both models with and without CBM provide satisfactory fits to the observations of 80% of the systems, but models with CBM provide better fits for systems with components in the post-main-sequence stage of stellar evolution [271]. This once again points toward the complications arising from using main-sequence DDLEBs to constrain CBM.

Finally, all of the studies discussed above have been conducted under the same assumption that the evolution of the binary systems can be treated as the evolution of two single stars without accounting for impacts from binary interactions on the stellar models. Such an assumption has been shown to be reasonable for the evolution of well-detached preinteraction binary systems at least when rotational mixing in single versus binary stars is considered (e.g., [272]). For detached, short-period ($P_{\rm orb} < 2$ d) binaries with strong tidal interactions, the conclusions appear to be mixed. Some studies suggest an enhanced rotation mixing in the presence of strong dynamical tides [273]. Others suggest that the effects of tides are limited in detached systems [272,274], while another recent study indicates that internal mixing is less efficient in detached binary systems than for single stars ([275], $P_{\rm orb} = 1.46$–6.32 d for 10 of the considered binary systems, and $P_{\rm orb} = 12.43$–33 d for the remaining three). For the sample of 50 DDLEBs shown in Figure 11, 21% and 31% have orbital periods below 5 and 10 d, respectively, while 52%, 23%, and 9.6% have $P_{\rm orb}$ in excess of 100 d, 200 d, and 500 d [276–287].

4.4. Asteroseismology

Asteroseismology is the study and interpretation of stellar pulsations, and it provides a powerful tool for studying stellar interiors. The pulsations are observed as variations in the surface brightness of the stars and extend deep into the stellar interiors, thereby carrying information about the conditions within. Modifications to the interior structure result in changes to the expected oscillation frequencies, and confronting predicted oscillation frequencies with observations in a process known as asteroseismic modeling provides important constraints on stellar structure and evolution theory. Such constraints have especially been made possible in the past couple of decades since the advent of space telescopes including WIRE (e.g., [288]), MOST [289], CoRoT [290,291], Kepler [292,293], K2 [294], BRITE [295], and TESS [296], which provide high-precision, high-cadence, and long-time baseline photometric light curves. These high-quality data resulted in a drastic increase in the number of detected oscillation frequencies in stars all across the HR diagram and provided the high-frequency resolution needed for mode identification required for asteroseismic modeling. Several review papers and books on asteroseismology already exist (e.g., [297–305], and references therein). Therefore, we refer to these papers for details on different types of pulsators, analysis methods, new discoveries, and procedures for asteroseismic modeling, and we focus here on the inferences made on the CBM from asteroseismic studies of both single and binary stars.

4.4.1. Onset of the Convective Core

One avenue to place constraints on CBM is studying stars in the mass regime where the transition between radiative to convective cores is expected to occur ($\approx$1.1 $M_\odot$). In this regime, we find the solar-like oscillators that oscillate in pressure (p) modes. These oscillations are an excellent probe of the convective core size, because they are modified by the presence of acoustic glitches in the sound speed profile caused by the sharp chemical gradient at the convective boundary [306–309]. As an example, a convective core with either little or a moderate amount of overshooting was found for the 1.18 ± 0.04 $M_\odot$ star KIC 12009504, whereas no convective core could unambiguously be found for KIC 6106415

($1.11 \pm 0.04\,M_\odot$) [310]. Another example is HD 203608 ($0.94 \pm 0.09\,M_\odot$), for which models with convective cores agree better with the observations than models without [311].

Stars such as the Sun arrive at the zero-age main-sequence (ZAMS) with a small convective core, which quickly disappears during the main-sequence evolution. The presence of the convective core is caused by an excess of ^{3}He and ^{12}C at the ZAMS, which are transformed to ^{4}He and ^{14}N through highly exothermic nuclear burning capable of sustaining a convective core [312]. The inclusion of CBM extends the lifetime of the convective cores [312], possibly even until the end of the main sequence if sufficiently high CBM parameters are considered [313] (see also Roxburgh [312] for a detailed discussion). For HD 203608, such overshooting ($\alpha_{ov} = 0.17 \pm 0.03$) allows the convective core to survive until the present age of the star [311]. For this particular star, the convective core would have disappeared at an age of 200 Myr without CBM, whereas it is expected to survive until ≈7 Gyr with overshooting. Stars of similar masses where no convective cores are found are of equal interest as they provide an upper limit for the extent of the CBM region.

4.4.2. Extent of the CBM Region across the Main-Sequence

To compare asteroseismic inferences on CBM to the results presented in Figure 11 for the study of binary stars, we compiled a sample of pulsating main-sequence stars for which a mass and CBM parameter has been derived asteroseismically. This full sample is shown in panel a of Figure 12, including also three of the CBM–mass relations from Figure 11 for reference. The asteroseismic CBM parameters were all converted to α_{pen} assuming $\alpha_{pen} \approx \alpha_{ov}$ and $\alpha_{pen} \approx 11.36\, f_{ov}$. The lack of measurements between ≈2 and ≈3 $M_\odot$ corresponds to the gap between the δ Sct and SPB instability strips. For 13 stars in this sample, only a lower (upright triangle) and upper (inverted triangle) limit on the CBM are available. Nine of the 13 stars are located in the open cluster NGC 6910 [314]. As seen in panel a, there is a general trend of increasing CBM parameters with increasing stellar mass for stars with $M \lesssim 2.5\,M_\odot$[9]; however, the scatter is larger and the CBM parameters are generally higher than the values found for the sample of 50 DDLEB in Figure 11. For the higher mass stars, a wide range in CBM paramaters are found with no clear dependence on stellar mass and inconsistent with a single value of the CBM parameter as previously found for the DDLEBs. We note that for a few of the stars, no CBM was needed to match the models to the observations.

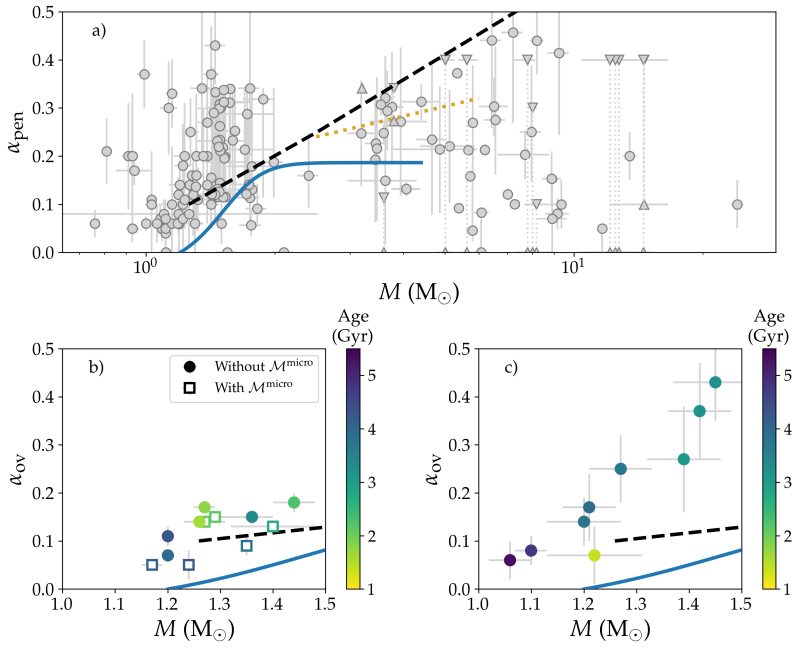

Figure 12. *Cont.*

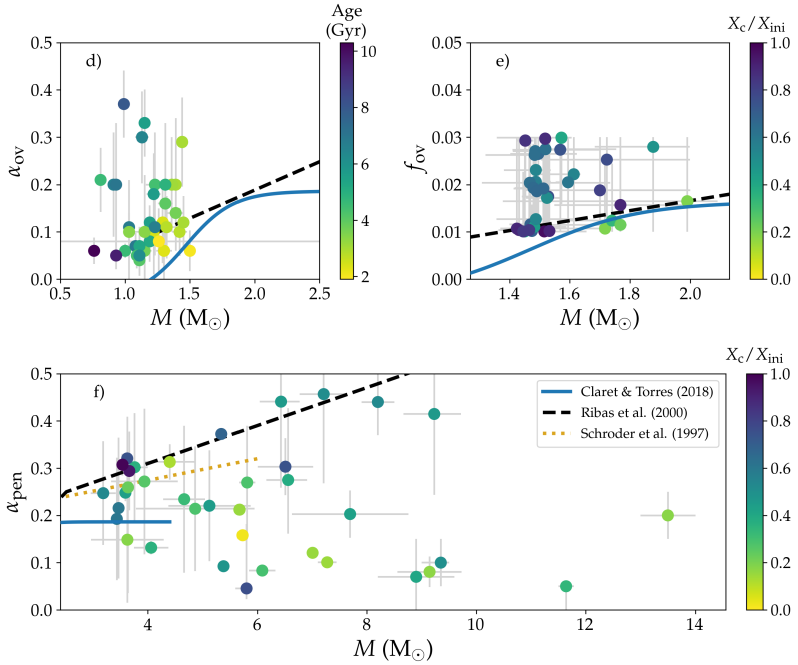

Figure 12. Asteroseismically derived CBM parameters available in the literature for 154 pulsating main-sequence stars. To combine the data from all sources in panel (**a**–**f**), we assumed $\alpha_{ov} \approx \alpha_{pen}$ and $11.36 f_{ov} \approx \alpha_{pen}$. Panels (**b**–**d**) show sub-samples of the stars from panel (**a**), where an ensemble study was carried out using the same stellar structure and evolution code and modeling methodology [73,315–317]. In panel (**f**), only $M \geq 3\,M_\odot$ stars from panel (**a**) with a known X_c/X_{ini} value are shown. For stars without estimated errors on the initial mass and CBM parameter, we adopt the average fractional errors from the sample with error estimates. Figure made by the authors using data from the following sources: [19,20,65,73,75,259,260,310,311,314–340].

The CBM parameters shown in Figure 12 were derived using a variety of different stellar structure and evolution codes and different 1D prescriptions for the CBM. As discussed in Sections 2.7 and 2.8, making direct comparisons and conversions between CBM parameters obtained from different sources is non-trivial. For this reason, we show in panels b–e four different sub-samples of the stars in panel a where a consistent stellar structure and evolution code and modeling methodology was applied to each sample. The data are color-coded according to the age of the stars either measured in Gyrs or taken as the ratio between the current and initial core hydrogen mass fraction X_c/X_{ini}. In panel f, we show all stars with $M \geq 3\,M_\odot$ for which an estimate of X_c/X_{ini} is available irrespective of the adopted code and modeling procedure. As the main-sequence lifetime is largely dependent on both the initial stellar mass and internal mixing properties of the stars, X_c/X_{ini} provides a much better age indicator when conducting comparison studies [341]. For this high-mass sample, we expect the differences in CBM prescription to be largely insignificant (cf. Section 2.7).

Panels b and c of Figure 12 show two different ensemble studies of solar-like oscillating stars, which both indicate an increase in the CBM parameter with mass albeit at different levels. For both samples, the derived CBM parameters are higher than the relation derived by Claret and Torres [20] from DDLEBs. The sample in panel b was modeled using the `Cesam2k` code both with (open squares) and without (filled circles) microscopic diffusion, indicating that less CBM is needed to explain the observations if microscopic diffusion is taken into account [315]. This is in line with previous results from the open cluster M67 [192,193]. In comparison, the sample in panel c was modeled using the `YREC` code, using the concept of an effective overshoot parameter which accounts for the automatic adjustment of the size of the CBM region to avoid nonsensical core sizes [73]. A similar study also derived the effective overshoot parameters for a sample of solar-like oscillators,

finding the current effective overshoot parameter to be zero up to ≈1.1 $M_\odot$ above which a scatter in the effective α_{ov} values appears and increases toward higher masses [342].

Both of the samples of pulsating stars in panels d and e were modeled using different versions of the MESA code and using machine learning algorithms to derive the stellar parameters from the observed oscillation properties of the stars. For the sample of solar-like stars in panel d, the majority of the stars show an increase in CBM parameter with mass and generally higher CBM parameters than the relation predicted by Claret and Torres [20]. For the sample of γ Dor stars in panel (e), no clear mass dependence is found. However, the errors on the CBM parameter are large and span the entire parameter range considered [317]. This is likely caused by the inability of the neural network to capture the fine details of the pulsation properties of the models, which are important for constraining this parameter.

The final panel f of Figure 12 focuses on the $M \geq 3\,M_\odot$ stars in the sample where a common X_c/X_{ini} age indicator is available. For 26 of the stars shown here, an ensemble study was carried out, whereas the remaining stars were studied individually. As already mentioned earlier, a much larger scatter in the CBM parameter is seen here with no indication that a single parameter fits all of the stars. No clear dependence on age is seen, either. One possible explanation for the observed scatter is that additional interior physical processes are influencing the measured and required CBM. As an example, envelope mixing arising from, e.g., internal rotation has a similar effect in bringing additional hydrogen to the core and can therefore enhance the effective core size. This gives rise to some degeneracies between the CBM and envelope mixing, which can be difficult to disentangle. On the other hand, internal magnetic fields can inhibit CBM. As an example, the low amount of overshooting ($f_{ov} = 0.004^{+0.012}_{-0.002}$) found for the pulsating magnetic B-type star HD 43317 suggests that the magnetic fields of the star might be suppressing the mixing near the core boundary [331]. The lack of observed high-radial order gravity (g) modes suggests that a near-core magnetic field of at least 500 kG is suppressing these modes in the star [343]. Prior to these results, the asteroseismic modeling of the magnetic β Cep star V2052 Ophiuchi revealed a lower overshoot parameter ($\alpha_{ov} = 0.07^{0.08}_{0.07}$, [325]) compared to its similar mass β Cep counterpart θ Ophiuchi ($\alpha_{ov} = 0.44 \pm 0.07$, [321]), indicating that magnetic fields are likely inhibiting the CBM for this star as well. For the lower mass ($M = 2.4\,M_\odot$) magnetic pulsating Ap star, a CBM parameter of $f_{ov} = 0.014$ was found [333] with no clear indication of inhibition of the CBM by the magnetic fields of the star.

4.4.3. Differentiating between Different CBM Prescriptions

Gravity mode oscillators are of particular interest for studying CBM, as g modes have their main probing power in the near core regions of the stars. SPB stars (3–10 $M_\odot$, g-modes) have been shown to be capable of distinguishing not only between different shapes of $D_{CBM}(r)$ profiles [64,344] but also between different choices of temperature gradients in the CBM region [64]. A higher-frequency precision corresponding to longer light curves (>1 yr) is needed to distinguish between different shapes of the mixing profiles compared to between radiative and adiabatic temperature gradients (>90 d) [64]. Oscillations in β Cep variables (10–25 $M_\odot$, p- and g-modes) can also distinguish between different CBM profiles and temperature gradients, but they require the mass of the star to be known to at least 1 % precision. Similar theoretical studies have not yet been carried out for γ Dor (g-modes) or δ Sct (p-modes) stars, while it was found for solar-like oscillators that their p-modes could not be used to differentiate between exponential diffusive overshoot and step overshoot [315].

So far, asteroseismic inferences on the shape of $D_{CBM}(r)$ and choice of ∇_T have only been attempted in a few cases, with the majority of studies focusing on estimating "just" the extent of the CBM region as discussed in the previous section. KIC 10526294 and KIC 7760680 are the first two SPB stars where a comparison between results assuming a step and exponential diffusive overshoot prescription was made [75,327]. For both stars, it was found that models with exponential diffusive overshoot provide better matches

to the observed period spacing pattern compared to models with step overshoot. In a subsequent study of KIC 7760680, the CBM profile was fixed to that of an extended convective penetration, while the temperature gradient was varied between a purely radiative gradient and one gradually changing from adiabatic to radiative based on the Peclet number (see Section 2.6) [65]. For this star, a radiative temperature gradient in the CBM region was preferred. However, it was also found that models without CBM were statistically preferred over models including CBM when the number of additional free parameters was taken into account. A comparison between step and exponential overshoot was briefly made for the SPB star KIC 8264293. The difference between the two was found to be minor, which was likely because the star is near the ZAMS and thereby lacks a significant chemical gradient at the core boundary, and the more extensive asteroseismic modeling of the star focused only on the exponential diffusive overshoot [340]. Finally, an ensemble asteroseismic study of 26 SPB stars revealed that 54.9% of the stars preferred convective penetration, whereas for 45.1%, the exponential diffusive overshoot prescription did better at reproducing the observed period spacing pattern [19,338].

5. Discussion and Future Work

In this review, we provided an overview of convective boundary mixing (CBM) in the main sequence stars. We discussed the most frequently used prescriptions for including CBM in 1D stellar evolution models. We described CBM from a hydrodynamics perspective with an emphasis on lessons learned from simulations. We provided an overview of the observations that are at odds with "standard" 1D models and showed how excess (often mass-dependent) mixing can better align models and observations.

Despite great progress in recent years, there remains plenty of work to do before a complete understanding of CBM will be achieved. In particular, most CBM processes described hydrodynamically and in simulations still lack robust parameterizations in 1D models. We encourage 1D modelers and 3D numericists to forge partnerships to derive, test, and apply new simulation-based prescriptions. We note in particular that there is a great deal of degeneracy in the language which is used to describe CBM processes in the literature (e.g., "overshoot" and "penetration" are often used interchangeably), and our community must adopt language which clearly differentiates between the various physical mechanisms at work. Below, we enumerate suggestions for future work and recommendations for future experiments which we believe will help to sort out the decades-old problem of CBM in stellar evolution.

From the perspective of 1D modeling and applying those models to observations, we have the following suggestions:

1. First and foremost, it is valuable to "grow the catalogue" of CBM observations. More observational constraints will allow us to not only test and verify new models but also may allow us to understand how complications such as, e.g., rotation affect CBM.
2. A uniform analysis of past observations using a consistent stellar structure and boundary mixing scheme should be performed.
3. To ease comparisons in future work, authors should clearly state which quantities their CBM prescriptions mix. Specifically, does CBM adjust ∇_{T} or not?
4. Evidence for extended convective penetration (Section 2.6) is seen in hydrodynamical simulations, and this prescription should be included in more stellar structure codes and models.
5. In main sequence intermediate- to high-mass stars, the mass and radius of the convective core should be clearly reported along with the mass and size of the CBM region. Whether the reported convective core mass does or does not include the mass in the CBM region should also be specified. This circumvents difficulties associated with making comparisons between codes using different CBM prescriptions and methods of limiting the size of the CBM region.
6. When reporting ages of stars on the main sequence, also report a quantity such as the core hydrogen fraction X_c / X_{init} for easier comparison across works.

We also recommend that the following experiments be performed and prescriptions be derived from 3D hydrodynamical simulations:

1. Whenever possible, 3D hydrodynamical simulations should strive to provide prescriptions that do not have free parameters but instead rely on stellar structure.
2. For example, overshoot depth and turbulent diffusive mixing profiles should be carefully calibrated and parameterized so that overshoot can be evaluated as a function of stellar structure rather than a specified $f_{\rm ov}$.
3. The 1D prescriptions derived from 3D simulation data should be validated using the same initial conditions employed in the 3D simulations. If the 1D prescription produces a different result from the 3D data, this should be explored in detail.
4. Simulations probing the thermal structure near a convective boundary should be evolved until thermal equilibrium is achieved. Performing short simulations which are initialized with CBM regions of various sizes can however qualitatively answer the question, "Which way does the convective boundary move?"
5. It is not clear how to properly parameterize dissipation, but dissipation sets the size of a convective penetration region. Future studies should answer the following: what sets the magnitude of the viscous dissipation? How does rotation affect it? How does magnetism and the presence of Ohmic dissipation affect it?
6. Entrainment is important when convective regions are first forming or when the convective luminosity or nuclear burning change rapidly compared to the convective overturn timescale. These evolutionary stages should be modeled by time-dependent convection (TDC) prescriptions [153]. Future work should test whether TDC models reproduce the entrainment rates at convective boundaries observed in simulations, and TDC models should be improved where they disagree with simulations.

A long-standing problem for stellar modelers and observers is the uncertainty that convective boundary mixing introduces into 1D stellar models. The uncertainties associated with CBM not only affect studies focused on stars but also ripple through other astrophysical disciplines which depend on state-of-the-art stellar models. Great strides have been made in the past few decades in understanding CBM both from observations, 1D, and 3D simulations. By combining the efforts of these often disparate lines of work, we can create and validate new mixing prescriptions and solve this long-lived problem.

Author Contributions: E.H.A. and M.G.P. contributed equally to all aspects to this manuscript. All authors have read and agreed to the published version of the manuscript.

Funding: E.H.A. was supported by a CIERA Postdoctoral Fellowship. This research was supported in part by the National Science Foundation under Grant No. NSF PHY-1748958 as well as through the TESS Guest Investigator program Cycle 4 under Grant No. 80NSSC22K0743 from NASA and by the Professor Harry Messel Research Fellowship in Physics Endowment, at the University of Sydney (M.G.P.).

Data Availability Statement: Inlists used to generate MESA stellar models in this work and data plotted in original figures are available online in the supplementary materials Zenodo [33].

Acknowledgments: E.H.A. thanks Adam Jermyn, Daniel Lecoanet, Benjamin Brown, Jeffrey Oishi, Adrian Fraser, and Rafa Fuentes for years of discussions on topics related to CBM. We thank Raphael Hirschi, Casey Meakin, Federico Rizzuti, and Tami Rogers for allowing us to reproduce figures from their past work. We also thank Jorick Vink, Dominic Bowman, and Jennifer van Saders for inviting and organizing us in writing this review. We are grateful to the participants of KITP's "Probes of Transport in Stars" program from Fall 2021, where we had many useful discussions regarding CBM.

Conflicts of Interest: The authors declare no conflict of interest. The funders had no role in the design of the study; in the collection, analyses, or interpretation of data; in the writing of the manuscript; or in the decision to publish the results.

Abbreviations

The following abbreviations are used in this manuscript:

BSG	Blue supergiant
CBM	Convective boundary mixing
CZ	Convection zone
DDLEB	Detached double-lined eclipsing binary
eMSTO	Extended main-sequence turnoff
LHS	Left-hand side
RHS	Right-hand side
RZ	Radiative zone
PZ	Penetrative zone
TAMS	Terminal age main sequence
ZAMS	Zero-age main sequence

Notes

1 To account for the step $f_0 H_{\mathrm{p,cc}}$ taken inside of the convective core, one would usually add f_0 to the overshooting parameter. As an example, in `MESA` one would use `overshoot_f`$= f_{\mathrm{ov}} + f_0$, where `overshoot_f` is the name of the overshoot parameter in `MESA`.

2 We note that the authors of both of these studies of detached double-lined eclipsing binary systems [76,77] use α_{ov} in their notation, but they are actually assuming an adiabatic temperature gradient in the CBM region. In other words, while they talk about a step-based overshooting using the free parameter α_{ov}, they are in fact referring to convective penetration.

3 The Anelastic approximation models low Mach number flows and assumes that Equation (12) reduces to $\nabla \cdot (\rho_0 \boldsymbol{u}) = 0$ where ρ_0 is the "background" density. The Boussinesq approximation goes one step further and assumes incompressibility, or that ρ_0 is constant everywhere so that Equation (12) becomes $\nabla \cdot \boldsymbol{u} = 0$; under the Boussinesq approximation, small-density perturbations are allowed to exist in the buoyancy term in the momentum equation.

4 $\mathcal{S}_{\mathrm{struct}}$ was often defined in terms of polytropic indices; thus, we use $\approx$ instead of $=$ in our definition here.

5 Similar to Equation 2 of Claret & Torres [20], which is discussed in our Section 4.3.1 [241].

6 The spectroscopic masses M_{Spec} are obtained from the spectroscopic $\log g$ values in combination with radius estimates from, e.g., relations between T_{eff} values, bolometric corrections, and spectral types (see [245]).

7 $\log g$ can be derived from the component masses and radii and was therefore held fixed for this comparison.

8 In the spectroscopic HR diagram, the luminosity is calculated as $\mathcal{L} = \frac{T_{\mathrm{eff}}^4}{g}$, thereby becoming independent of distance and extinction measurements.

9 The Spearman's rank correlation coefficient for this sub-sample is 0.324 with a p-value of 0.0011, corresponding to strong evidence for a positive correlation between the CBM parameter and stellar mass.

References

1. Böhm-Vitense, E. Über die Wasserstoffkonvektionszone in Sternen verschiedener Effektivtemperaturen und Leuchtkräfte. Mit 5 Textabbildungen. *Z. Astrophys.* **1958**, *46*, 108.
2. Anders, E.H.; Jermyn, A.S.; Lecoanet, D.; Fraser, A.E.; Cresswell, I.G.; Joyce, M.; Fuentes, J.R. Schwarzschild and Ledoux are Equivalent on Evolutionary Timescales. *Astrophys. J. Lett.* **2022**, *928*, L10.
3. Chabrier, G.; Baraffe, I. Structure and evolution of low-mass stars. *Astron. Astrophys.* **1997**, *327*, 1039–1053.
4. Chabrier, G.; Baraffe, I. Theory of Low-Mass Stars and Substellar Objects. *Annu. Rev. Astron. Astrophys.* **2000**, *38*, 337–377.
5. Jermyn, A.S.; Anders, E.H.; Lecoanet, D.; Cantiello, M. An Atlas of Convection in Main-sequence Stars. *Astrophys. J. Suppl. Ser.* **2022**, *262*, 19.
6. Pinsonneault, M. Mixing in Stars. *Annu. Rev. Astron. Astrophys.* **1997**, *35*, 557–605. [CrossRef]
7. Carlos, M.; Meléndez, J.; Spina, L.; dos Santos, L.A.; Bedell, M.; Ramirez, I.; Asplund, M.; Bean, J.L.; Yong, D.; Yana Galarza, J.; et al. The Li-age correlation: The Sun is unusually Li deficient for its age. *Mon. Not. R. Astron. Soc.* **2019**, *485*, 4052–4059.
8. Dumont, T.; Palacios, A.; Charbonnel, C.; Richard, O.; Amard, L.; Augustson, K.; Mathis, S. Lithium depletion and angular momentum transport in solar-type stars. *Astron. Astrophys.* **2021**, *646*, A48.
9. Christensen-Dalsgaard, J.; Monteiro, M.J.P.F.G.; Rempel, M.; Thompson, M.J. A more realistic representation of overshoot at the base of the solar convective envelope as seen by helioseismology. *Mon. Not. R. Astron. Soc.* **2011**, *414*, 1158–1174.
10. Bergemann, M.; Serenelli, A. Solar Abundance Problem. In *Determination of Atmospheric Parameters of B*;Springer: Cham, Switzerland, 2014; pp. 245–258. [CrossRef]
11. Basu, S. Global seismology of the Sun. *Living Rev. Sol. Phys.* **2016**, *13*, 2.
12. Hansen, C.J.; Kawaler, S.D.; Trimble, V. *Stellar Interiors: Physical Principles, Structure, and Evolution*; Springer: Cham, Switzerland, 2004.

13. Cantiello, M.; Braithwaite, J. Envelope Convection, Surface Magnetism, and Spots in A and Late B-type Stars. *Astrophys. J.* **2019**, *883*, 106.
14. Jermyn, A.S.; Anders, E.H.; Cantiello, M. A Transparent Window into Early-type Stellar Variability. *Astrophys. J.* **2022**, *926*, 221.
15. Johnston, C. One size does not fit all: Evidence for a range of mixing efficiencies in stellar evolution calculations. *Astron. Astrophys.* **2021**, *655*, A29.
16. Kaiser, E.A.; Hirschi, R.; Arnett, W.D.; Georgy, C.; Scott, L.J.A.; Cristini, A. Relative importance of convective uncertainties in massive stars. *Mon. Not. R. Astron. Soc.* **2020**, *496*, 1967–1989.
17. Schootemeijer, A.; Langer, N.; Grin, N.J.; Wang, C. Constraining mixing in massive stars in the Small Magellanic Cloud. *Astron. Astrophys.* **2019**, *625*, A132.
18. Farrell, E.J.; Groh, J.H.; Meynet, G.; Eldridge, J.J.; Ekström, S.; Georgy, C. SNAPSHOT: Connections between internal and surface properties of massive stars. *Mon. Not. R. Astron. Soc.* **2020**, *495*, 4659–4680.
19. Pedersen, M.G.; Aerts, C.; Pápics, P.I.; Michielsen, M.; Gebruers, S.; Rogers, T.M.; Molenberghs, G.; Burssens, S.; Garcia, S.; Bowman, D.M. Internal mixing of rotating stars inferred from dipole gravity modes. *Nat. Astron.* **2021**, *5*, 715–722.
20. Claret, A.; Torres, G. The Dependence of Convective Core Overshooting on Stellar Mass: Additional Binary Systems and Improved Calibration. *Astrophys. J.* **2018**, *859*, 100.
21. Castro, N.; Fossati, L.; Langer, N.; Simón-Díaz, S.; Schneider, F.R.N.; Izzard, R.G. The spectroscopic Hertzsprung-Russell diagram of Galactic massive stars. *Astron. Astrophys.* **2014**, *570*, L13.
22. Higgins, E.R.; Vink, J.S. Massive star evolution: Rotation, winds, and overshooting vectors in the mass-luminosity plane. I. A calibrated grid of rotating single star models. *Astron. Astrophys.* **2019**, *622*, A50.
23. Martinet, S.; Meynet, G.; Ekström, S.; Simón-Díaz, S.; Holgado, G.; Castro, N.; Georgy, C.; Eggenberger, P.; Buldgen, G.; Salmon, S.; et al. Convective core sizes in rotating massive stars. I. Constraints from solar metallicity OB field stars. *Astron. Astrophys.* **2021**, *648*, A126.
24. Higgins, E.R.; Vink, J.S. Stellar age determination in the mass-luminosity plane. *Mon. Not. R. Astron. Soc.* **2023**, *518*, 1158–1169.
25. Meakin, C.A.; Arnett, D. Turbulent Convection in Stellar Interiors. I. Hydrodynamic Simulation. *Astrophys. J.* **2007**, *667*, 448–475.
26. Gilet, C.; Almgren, A.S.; Bell, J.B.; Nonaka, A.; Woosley, S.E.; Zingale, M. Low Mach Number Modeling of Core Convection in Massive Stars. *Astrophys. J.* **2013**, *773*, 137. [CrossRef]
27. Cristini, A.; Meakin, C.; Hirschi, R.; Arnett, D.; Georgy, C.; Viallet, M.; Walkington, I. 3D hydrodynamic simulations of carbon burning in massive stars. *Mon. Not. R. Astron. Soc.* **2017**, *471*, 279–300.
28. Jones, S.; Andrassy, R.; Sandalski, S.; Davis, A.; Woodward, P.; Herwig, F. Idealized hydrodynamic simulations of turbulent oxygen-burning shell convection in 4π geometry. *Mon. Not. R. Astron. Soc.* **2017**, *465*, 2991–3010.
29. Andrassy, R.; Herwig, F.; Woodward, P.; Ritter, C. 3D hydrodynamic simulations of C ingestion into a convective O shell. *Mon. Not. R. Astron. Soc.* **2020**, *491*, 972–992.
30. Higl, J.; Müller, E.; Weiss, A. Calibrating core overshooting parameters with two-dimensional hydrodynamical simulations. *Astron. Astrophys.* **2021**, *646*, A133.
31. Rizzuti, F.; Hirschi, R.; Georgy, C.; Arnett, W.D.; Meakin, C.; Murphy, A.S. Realistic 3D hydrodynamics simulations find significant turbulent entrainment in massive stars. *Mon. Not. R. Astron. Soc.* **2022**, *515*, 4013–4019.
32. Brandenburg, A.; Svedin, A.; Vasil, G.M. Turbulent diffusion with rotation or magnetic fields. *Mon. Not. R. Astron. Soc.* **2009**, *395*, 1599–1606.
33. Anders, E.H.; Pedersen, M.G. *Supplemental Materials for "Convective Boundary Mixing in Main-Sequence Stars: Theory and Empirical Constraints"*; Zenodo: Geneva, Switzerland, 2023. [CrossRef]
34. Paxton, B.; Schwab, J.; Bauer, E.B.; Bildsten, L.; Blinnikov, S.; Duffell, P.; Farmer, R.; Goldberg, J.A.; Marchant, P.; Sorokina, E.; et al. Modules for Experiments in Stellar Astrophysics (MESA): Convective Boundaries, Element Diffusion, and Massive Star Explosions. *Astrophys. J. Suppl. Ser.* **2018**, *234*, 34.
35. Garaud, P. Double-Diffusive Convection at Low Prandtl Number. *Annu. Rev. Fluid Mech.* **2018**, *50*, 275–298. [CrossRef]
36. Salaris, M.; Cassisi, S. Chemical element transport in stellar evolution models. *R. Soc. Open Sci.* **2017**, *4*, 170192.
37. Georgy, C.; Saio, H.; Meynet, G. Blue supergiants as tests for stellar physics. *Astron. Astrophys.* **2021**, *650*, A128.
38. Gabriel, M.; Noels, A.; Montalbán, J.; Miglio, A. Proper use of Schwarzschild Ledoux criteria in stellar evolution computations. *Astron. Astrophys.* **2014**, *569*, A63.
39. Zahn, J.P. Convective penetration in stellar interiors. *Astron. Astrophys.* **1991**, *252*, 179–188.
40. Woo, J.H.; Demarque, P. Empirical Constraints on Convective Core Overshoot. *Astron. J.* **2001**, *122*, 1602–1606.
41. Freytag, B.; Ludwig, H.G.; Steffen, M. Hydrodynamical models of stellar convection. The role of overshoot in DA white dwarfs, A-type stars, and the Sun. *Astron. Astrophys.* **1996**, *313*, 497–516.
42. Herwig, F. The evolution of AGB stars with convective overshoot. *Astron. Astrophys.* **2000**, *360*, 952–968.
43. Weiss, A.; Schlattl, H. GARSTEC—the Garching Stellar Evolution Code. The direct descendant of the legendary Kippenhahn code. *Astrophys. Space Sci.* **2008**, *316*, 99–106. [CrossRef]
44. Paxton, B.; Bildsten, L.; Dotter, A.; Herwig, F.; Lesaffre, P.; Timmes, F. Modules for Experiments in Stellar Astrophysics (MESA). *Astrophys. J. Suppl. Ser.* **2011**, *192*, 3.

45. Paxton, B.; Cantiello, M.; Arras, P.; Bildsten, L.; Brown, E.F.; Dotter, A.; Mankovich, C.; Montgomery, M.H.; Stello, D.; Timmes, F.X.; et al. Modules for Experiments in Stellar Astrophysics (MESA): Planets, Oscillations, Rotation, and Massive Stars. *Astrophys. J. Suppl. Ser.* **2013**, *208*, 4.
46. Paxton, B.; Marchant, P.; Schwab, J.; Bauer, E.B.; Bildsten, L.; Cantiello, M.; Dessart, L.; Farmer, R.; Hu, H.; Langer, N.; et al. Modules for Experiments in Stellar Astrophysics (MESA): Binaries, Pulsations, and Explosions. *Astrophys. J. Suppl. Ser.* **2015**, *220*, 15.
47. Paxton, B.; Smolec, R.; Schwab, J.; Gautschy, A.; Bildsten, L.; Cantiello, M.; Dotter, A.; Farmer, R.; Goldberg, J.A.; Jermyn, A.S.; et al. Modules for Experiments in Stellar Astrophysics (MESA): Pulsating Variable Stars, Rotation, Convective Boundaries, and Energy Conservation. *Astrophys. J. Suppl. Ser.* **2019**, *243*, 10,
48. Roxburgh, I.W. A note on the boundary of convective zones in stars. *Mon. Not. R. Astron. Soc.* **1965**, *130*, 223. [CrossRef]
49. Prather, M.J.; Demarque, P. Convective Overshoot Mixing in Old Open Clusters. *Astrophys. J.* **1974**, *193*, 109–112. [CrossRef]
50. Dotter, A.; Chaboyer, B.; Jevremović, D.; Baron, E.; Ferguson, J.W.; Sarajedini, A.; Anderson, J. The ACS Survey of Galactic Globular Clusters. II. Stellar Evolution Tracks, Isochrones, Luminosity Functions, and Synthetic Horizontal-Branch Models. *Astron. J.* **2007**, *134*, 376–390.
51. Dotter, A.; Chaboyer, B.; Jevremović, D.; Kostov, V.; Baron, E.; Ferguson, J.W. The Dartmouth Stellar Evolution Database. *Astrophys. J. Suppl. Ser.* **2008**, *178*, 89–101.
52. Cassisi, S.; Salaris, M. A critical investigation on the discrepancy between the observational and the theoretical red giant luminosity function 'bump'. *Mon. Not. R. Astron. Soc.* **1997**, *285*, 593–603.
53. Salaris, M.; Cassisi, S. A new analysis of the red giant branch 'tip' distance scale and the value of the Hubble constant. *Mon. Not. R. Astron. Soc.* **1998**, *298*, 166–178.
54. Pietrinferni, A.; Cassisi, S.; Salaris, M.; Castelli, F. A Large Stellar Evolution Database for Population Synthesis Studies. I. Scaled Solar Models and Isochrones. *Astrophys. J.* **2004**, *612*, 168–190.
55. Pietrinferni, A.; Cassisi, S.; Salaris, M.; Castelli, F. A Large Stellar Evolution Database for Population Synthesis Studies. II. Stellar Models and Isochrones for an α-enhanced Metal Distribution. *Astrophys. J.* **2006**, *642*, 797–812.
56. Cordier, D.; Pietrinferni, A.; Cassisi, S.; Salaris, M. A Large Stellar Evolution Database for Population Synthesis Studies. III. Inclusion of the Full Asymptotic Giant Branch Phase and Web Tools for Stellar Population Analyses. *Astron. J.* **2007**, *133*, 468–478.
57. Percival, S.M.; Salaris, M.; Cassisi, S.; Pietrinferni, A. A Large Stellar Evolution Database for Population Synthesis Studies. IV. Integrated Properties and Spectra. *Astrophys. J.* **2009**, *690*, 427–439.
58. Pietrinferni, A.; Cassisi, S.; Salaris, M.; Percival, S.; Ferguson, J.W. A Large Stellar Evolution Database for Population Synthesis Studies. V. Stellar Models and Isochrones with CNONa Abundance Anticorrelations. *Astrophys. J.* **2009**, *697*, 275–282.
59. Hui-Bon-Hoa, A. The Toulouse Geneva Evolution Code (TGEC). *Astrophys. Space Sci.* **2008**, *316*, 55–60. [CrossRef]
60. Théado, S.; Alecian, G.; LeBlanc, F.; Vauclair, S. The new Toulouse-Geneva stellar evolution code including radiative accelerations of heavy elements. *Astron. Astrophys.* **2012**, *546*, A100.
61. Demarque, P.; Guenther, D.B.; Li, L.H.; Mazumdar, A.; Straka, C.W. YREC: The Yale rotating stellar evolution code. Non-rotating version, seismology applications. *Astrophys. Space Sci.* **2008**, *316*, 31–41.
62. Eggenberger, P.; Meynet, G.; Maeder, A.; Hirschi, R.; Charbonnel, C.; Talon, S.; Ekström, S. The Geneva stellar evolution code. *Astrophys. Space Sci.* **2008**, *316*, 43–54. [CrossRef]
63. Viallet, M.; Meakin, C.; Prat, V.; Arnett, D. Toward a consistent use of overshooting parametrizations in 1D stellar evolution codes. *Astron. Astrophys.* **2015**, *580*, A61.
64. Michielsen, M.; Pedersen, M.G.; Augustson, K.C.; Mathis, S.; Aerts, C. Probing the shape of the mixing profile and of the thermal structure at the convective core boundary through asteroseismology. *Astron. Astrophys.* **2019**, *628*, A76.
65. Michielsen, M.; Aerts, C.; Bowman, D.M. Probing the temperature gradient in the core boundary layer of stars with gravito-inertial modes. The case of KIC 7760680. *Astron. Astrophys.* **2021**, *650*, A175.
66. Christensen-Dalsgaard, J. ASTEC—the Aarhus STellar Evolution Code. *Astrophys. Space Sci.* **2008**, *316*, 13–24.
67. Monteiro, M.J.P.F.G.; Christensen-Dalsgaard, J.; Thompson, M.J. Seismic study of overshoot at the base of the solar convective envelope. *Astron. Astrophys.* **1994**, *283*, 247–262.
68. Demarque, P.; Woo, J.H.; Kim, Y.C.; Yi, S.K. Y^2 Isochrones with an Improved Core Overshoot Treatment. *Astrophys. J. Suppl. Ser.* **2004**, *155*, 667–674. [CrossRef]
69. Spada, F.; Demarque, P.; Kim, Y.C.; Boyajian, T.S.; Brewer, J.M. The Yale-Potsdam Stellar Isochrones. *Astrophys. J.* **2017**, *838*, 161.
70. Magic, Z.; Serenelli, A.; Weiss, A.; Chaboyer, B. On Using the Color-Magnitude Diagram Morphology of M67 to Test Solar Abundances. *Astrophys. J.* **2010**, *718*, 1378–1387.
71. Claret, A. Updating the theoretical tidal evolution constants: Apsidal motion and the moment of inertia. *Astron. Astrophys.* **2019**, *628*, A29.
72. Morel, P.; Lebreton, Y. CESAM: A free code for stellar evolution calculations. *Astrophys. Space Sci.* **2008**, *316*, 61–73.
73. Viani, L.S.; Basu, S. Examining the Relationship Between Convective Core Overshoot and Stellar Properties Using Asteroseismology. *Astrophys. J.* **2020**, *904*, 22.
74. Deheuvels, S. Probing core overshooting using asteroseismology. *Bull. Soc. R. Sci. Liege* **2019**, *88*, 84–105. [CrossRef]

75. Moravveji, E.; Townsend, R.H.D.; Aerts, C.; Mathis, S. Sub-inertial Gravity Modes in the B8V Star KIC 7760680 Reveal Moderate Core Overshooting and Low Vertical Diffusive Mixing. *Astrophys. J.* **2016**, *823*, 130. [CrossRef]
76. Claret, A.; Torres, G. The Dependence of Convective Core Overshooting on Stellar Mass: A Semi-empirical Determination Using the Diffusive Approach with Two Different Element Mixtures. *Astrophys. J.* **2017**, *849*, 18.
77. Tkachenko, A.; Pavlovski, K.; Johnston, C.; Pedersen, M.G.; Michielsen, M.; Bowman, D.M.; Southworth, J.; Tsymbal, V.; Aerts, C. The mass discrepancy in intermediate- and high-mass eclipsing binaries: The need for higher convective core masses. *Astron. Astrophys.* **2020**, *637*, A60.
78. Noels, A.; Montalban, J.; Miglio, A.; Godart, M.; Ventura, P. Overshooting and semiconvection: Structural changes and asteroseismic signatures. *Astrophys. Space Sci.* **2010**, *328*, 227–236. [CrossRef]
79. Unno, W. Anisotropy of Solar Convection. *Astrophys. J.* **1957**, *126*, 259. [CrossRef]
80. Böhm, K.H. The Mixing of Matter in the Layer Below the Outer Solar Convection Zone. *Astrophys. J.* **1963**, *138*, 297. [CrossRef]
81. Saslaw, W.C.; Schwarzschild, M. Overshooting from Stellar Convective Cores. *Astrophys. J.* **1965**, *142*, 1468. [CrossRef]
82. Zahn, J.P.; Toomre, J.; Latour, J. Nonlinear modal analysis of penetrative convection. *Geophys. Astrophys. Fluid Dyn.* **1982**, *22*, 159–193. [CrossRef]
83. Straus, J.M.; Blake, J.B.; Schramm, D.N. Effects of convective overshoot on lithium depletion in main-sequence stars. *Astrophys. J.* **1976**, *204*, 481–487. [CrossRef]
84. Spiegel, E.A. A Generalization of the Mixing-Length Theory of Turbulent Convection. *Astrophys. J.* **1963**, *138*, 216. [CrossRef]
85. Shaviv, G.; Salpeter, E.E. Convective Overshooting in Stellar Interior Models. *Astrophys. J.* **1973**, *184*, 191–200. [CrossRef]
86. Nordlund, A. On Convection in Stellar Atmospheres. *Astron. Astrophys.* **1974**, *32*, 407.
87. Maeder, A. Stellar evolution III: The overshooting from convective cores. *Astron. Astrophys.* **1975**, *40*, 303–310.
88. Cogan, B.C. Convective Overshooting in Main-Sequence Models. *Astrophys. J.* **1975**, *201*, 637–640. [CrossRef]
89. Ulrich, R.K. A Nonlocal Mixing-Length Theory of Convection for Use in Numerical Calculations. *Astrophys. J.* **1976**, *207*, 564–573. [CrossRef]
90. Langer, N. Non-local treatment of convection and overshooting from stellar convective cores. *Astron. Astrophys.* **1986**, *164*, 45–50.
91. Marcus, P.S.; Press, W.H.; Teukolsky, S.A. Multiscale model equations for turbulent convection and convective overshoot. *Astrophys. J.* **1983**, *267*, 795–821. [CrossRef]
92. Zhang, Q.S.; Li, Y. Turbulent Convection Model in the Overshooting Region. I. Effects of the Convective Mixing in the Solar Overshooting Region. *Astrophys. J.* **2012**, *746*, 50. [CrossRef]
93. Zhang, Q.S. A Simple Scheme to Implement a Nonlocal Turbulent Convection Model for Convective Overshoot Mixing. *Astrophys. J.* **2016**, *818*, 146.
94. Canuto, V.M. Stellar mixing. V. Overshooting. *Astron. Astrophys.* **2011**, *528*, A80. [CrossRef]
95. Kupka, F.; Montgomery, M.H. A-star envelopes: A test of local and non-local models of convection. *Mon. Not. R. Astron. Soc.* **2002**, *330*, L6–L10. [CrossRef]
96. Kupka, F.; Ahlborn, F.; Weiss, A. Stellar evolution models with overshooting based on 3-equation non-local theories I. Physical basis and the computation of the dissipation rate. *arXiv* **2022**, arXiv:2207.12296.
97. Chen, C.J. Response of an Optically Thin, Isothermal Atmosphere to a Convective Overshoot. *Sol. Phys.* **1974**, *37*, 53–62. [CrossRef]
98. Renzini, A. Some embarrassments in current treatments of convective overshooting. *Astron. Astrophys.* **1987**, *188*, 49–54.
99. Pratt, J.; Baraffe, I.; Goffrey, T.; Constantino, T.; Viallet, M.; Popov, M.V.; Walder, R.; Folini, D. Extreme value statistics for two-dimensional convective penetration in a pre-main sequence star. *Astron. Astrophys.* **2017**, *604*, A125.
100. Augustson, K.C.; Mathis, S. A Model of Rotating Convection in Stellar and Planetary Interiors. I. Convective Penetration. *Astrophys. J.* **2019**, *874*, 83.
101. Herwig, F.; Freytag, B.; Fuchs, T.; Hansen, J.P.; Hueckstaedt, R.M.; Porter, D.H.; Timmes, F.X.; Woodward, P.R. Convective and Non-Convective Mixing in AGB Stars. In *Why Galaxies Care about AGB Stars: Their Importance as Actors and Probes*; Kerschbaum, F., Charbonnel, C., Wing, R.F., Eds.; Astronomical Society of the Pacific Conference Series; Astronomical Society of the Pacific: San Francisco, CA, USA, 2007; Volume 378, p. 43.
102. Spiegel, E.A.; Veronis, G. On the Boussinesq Approximation for a Compressible Fluid. *Astrophys. J.* **1960**, *131*, 442. [CrossRef]
103. Lantz, S.R. Dynamical Behavior of Magnetic Fields in a Stratified, Convecting Fluid Layer. Ph.D. Thesis, Cornell University, New York, NY, USA, 1992.
104. Braginsky, S.I.; Roberts, P.H. Equations governing convection in earth's core and the geodynamo. *Geophys. Astrophys. Fluid Dyn.* **1995**, *79*, 1–97. [CrossRef]
105. Lantz, S.R.; Fan, Y. Anelastic Magnetohydrodynamic Equations for Modeling Solar and Stellar Convection Zones. *Astrophys. J. Suppl. Ser.* **1999**, *121*, 247–264. [CrossRef]
106. Jones, C.A.; Kuzanyan, K.M.; Mitchell, R.H. Linear theory of compressible convection in rapidly rotating spherical shells, using the anelastic approximation. *J. Fluid Mech.* **2009**, *634*, 291. [CrossRef]
107. Landau, L.D.; Lifshitz, E.M. Fluid Mechanics. 1987. Available online: https://www.sciencedirect.com/book/9780080339337/fluid-mechanics#book-info (accessed on 9 February 2023).
108. Grossmann, S.; Lohse, D. Scaling in thermal convection: A unifying theory. *J. Fluid Mech.* **2000**, *407*, 27–56.

109. Jones, C.A.; Mizerski, K.A.; Kessar, M. Fully developed anelastic convection with no-slip boundaries. *J. Fluid Mech.* **2022**, *930*, A13. [CrossRef]
110. Roxburgh, I.W. Integral constraints on convective overshooting. *Astron. Astrophys.* **1989**, *211*, 361–364.
111. Käpylä, P.J.; Rheinhardt, M.; Brandenburg, A.; Arlt, R.; Käpylä, M.J.; Lagg, A.; Olspert, N.; Warnecke, J. Extended Subadiabatic Layer in Simulations of Overshooting Convection. *Astrophys. J. Lett.* **2017**, *845*, L23.
112. Anders, E.H.; Jermyn, A.S.; Lecoanet, D.; Fuentes, J.R.; Korre, L.; Brown, B.P.; Oishi, J.S. Convective Boundary Mixing Processes. *Res. Notes Am. Astron. Soc.* **2022**, *6*, 41. [CrossRef]
113. Hurlburt, N.E.; Toomre, J.; Massaguer, J.M.; Zahn, J.P. Penetration below a Convection Zone. *Astrophys. J.* **1994**, *421*, 245. [CrossRef]
114. Lecoanet, D.; Schwab, J.; Quataert, E.; Bildsten, L.; Timmes, F.X.; Burns, K.J.; Vasil, G.M.; Oishi, J.S.; Brown, B.P. Turbulent Chemical Diffusion in Convectively Bounded Carbon Flames. *Astrophys. J.* **2016**, *832*, 71.
115. Couston, L.A.; Lecoanet, D.; Favier, B.; Le Bars, M. Dynamics of mixed convective-stably-stratified fluids. *Phys. Rev. Fluids* **2017**, *2*, 094804.
116. Anders, E.H.; Jermyn, A.S.; Lecoanet, D.; Brown, B.P. Stellar Convective Penetration: Parameterized Theory and Dynamical Simulations. *Astrophys. J.* **2022**, *926*, 169.
117. Aerts, C.; Augustson, K.; Mathis, S.; Pedersen, M.G.; Mombarg, J.S.G.; Vanlaer, V.; Van Beeck, J.; Van Reeth, T. Rossby numbers and stiffness values inferred from gravity-mode asteroseismology of rotating F- and B-type dwarfs. Consequences for mixing, transport, magnetism, and convective penetration. *Astron. Astrophys.* **2021**, *656*, A121.
118. Kippenhahn, R.; Weigert, A.; Weiss, A. *Stellar Structure and Evolution*; Springer: Cham, Switzerland, 2013. [CrossRef]
119. Brummell, N.H.; Clune, T.L.; Toomre, J. Penetration and Overshooting in Turbulent Compressible Convection. *Astrophys. J.* **2002**, *570*, 825–854. [CrossRef]
120. Rogers, T.M.; Glatzmaier, G.A. Penetrative Convection within the Anelastic Approximation. *Astrophys. J.* **2005**, *620*, 432–441. [CrossRef]
121. Browning, M.K.; Brun, A.S.; Toomre, J. Simulations of Core Convection in Rotating A-Type Stars: Differential Rotation and Overshooting. *Astrophys. J.* **2004**, *601*, 512–529.
122. Rempel, M. Overshoot at the Base of the Solar Convection Zone: A Semianalytical Approach. *Astrophys. J.* **2004**, *607*, 1046–1064. [CrossRef]
123. Rogers, T.M.; Glatzmaier, G.A.; Jones, C.A. Numerical Simulations of Penetration and Overshoot in the Sun. *Astrophys. J.* **2006**, *653*, 765–773.
124. Brun, A.S.; Miesch, M.S.; Toomre, J. Modeling the Dynamical Coupling of Solar Convection with the Radiative Interior. *Astrophys. J.* **2011**, *742*, 79. [CrossRef]
125. Singh, H.P.; Roxburgh, I.W.; Chan, K.L. A study of penetration at the bottom of a stellar convective envelope and its scaling relationships. *Astron. Astrophys.* **1998**, *340*, 178–182.
126. Saikia, E.; Singh, H.P.; Chan, K.L.; Roxburgh, I.W.; Srivastava, M.P. Examination of Scaling Relationships Involving Penetration Distance at the Bottom of a Stellar Convective Envelope. *Astrophys. J.* **2000**, *529*, 402–413. [CrossRef]
127. Hurlburt, N.E.; Toomre, J.; Massaguer, J.M. Nonlinear Compressible Convection Penetrating into Stable Layers and Producing Internal Gravity Waves. *Astrophys. J.* **1986**, *311*, 563. [CrossRef]
128. Kiraga, M.; Jahn, K.; Muthsam, H.J.; Stępień, K. 2D Computer Simulations of Stellar Convection Using a Three-Layer Model. *Acta Astron.* **1995**, *45*, 685–704.
129. Bazán, G.; Arnett, D. Two-dimensional Hydrodynamics of Pre–Core Collapse: Oxygen Shell Burning. *Astrophys. J.* **1998**, *496*, 316–332.
130. Dietrich, W.; Wicht, J. Penetrative Convection in Partly Stratified Rapidly Rotating Spherical Shells. *Front. Earth Sci.* **2018**, *6*, 189,
131. Cai, T. Upward Overshooting in Turbulent Compressible Convection. I. Effects of the Relative Stability Parameter, the Prandtl Number, and the Péclet Number. *Astrophys. J.* **2020**, *888*, 46. [CrossRef]
132. Cai, T. Upward Overshooting in Turbulent Compressible Convection. II. Simulations at Large Relative Stability Parameters. *Astrophys. J.* **2020**, *891*, 49. [CrossRef]
133. Tian, C.L.; Deng, L.C.; Chan, K.L. Numerical simulations of downward convective overshooting in giants. *Mon. Not. R. Astron. Soc.* **2009**, *398*, 1011–1022.
134. Käpylä, P.J. Overshooting in simulations of compressible convection. *Astron. Astrophys.* **2019**, *631*, A122.
135. Korre, L.; Garaud, P.; Brummell, N.H. Convective overshooting and penetration in a Boussinesq spherical shell. *Mon. Not. R. Astron. Soc.* **2019**, *484*, 1220–1237.
136. Brown, B.P.; Vasil, G.M.; Zweibel, E.G. Energy Conservation and Gravity Waves in Sound-proof Treatments of Stellar Interiors. Part I. Anelastic Approximations. *Astrophys. J.* **2012**, *756*, 109.
137. Herwig, F.; Freytag, B.; Hueckstaedt, R.M.; Timmes, F.X. Hydrodynamic Simulations of He Shell Flash Convection. *Astrophys. J.* **2006**, *642*, 1057–1074.
138. Woodward, P.R.; Herwig, F.; Lin, P.H. Hydrodynamic Simulations of H Entrainment at the Top of He-shell Flash Convection. *Astrophys. J.* **2015**, *798*, 49. [CrossRef]
139. Turner, J.S. The behaviour of a stable salinity gradient heated from below. *J. Fluid Mech.* **1968**, *33*, 183–200. [CrossRef]

140. Deardorff, J.W.; Willis, G.E.; Lilly, D.K. Laboratory investigation of non-steady penetrative convection. *J. Fluid Mech.* **1969**, *35*, 7–31. [CrossRef]
141. Kato, H.; Phillips, O.M. On the penetration of a turbulent layer into stratified fluid. *J. Fluid Mech.* **1969**, *37*, 643–655. [CrossRef]
142. Linden, P.F. The deepening of a mixed layer in a stratified fluid. *J. Fluid Mech.* **1975**, *71*, 385–405. [CrossRef]
143. Fernando, H.J.S. The formation of a layered structure when a stable salinity gradient is heated from below. *J. Fluid Mech.* **1987**, *182*, 525–541. [CrossRef]
144. Molemaker, M.J.; Dijkstra, H.A. The formation and evolution of a diffusive interface. *J. Fluid Mech.* **1997**, *331*, 199–229. [CrossRef]
145. Leppinen, D.M. The erosion of a salinity step by distributed and localized heat sources. *Numer. Heat Transf. Part A Appl.* **2003**, *44*, 625–644.
146. Fuentes, J.R.; Cumming, A. Penetration of a cooling convective layer into a stably-stratified composition gradient: Entrainment at low Prandtl number. *Phys. Rev. Fluids* **2020**, *5*, 124501.
147. Toppaladoddi, S.; Wettlaufer, J.S. Penetrative convection at high Rayleigh numbers. *Phys. Rev. Fluids* **2018**, *3*, 043501.
148. Arnett, D.; Meakin, C.; Young, P.A. Turbulent Convection in Stellar Interiors. II. The Velocity Field. *Astrophys. J.* **2009**, *690*, 1715–1729.
149. Mocák, M.; Müller, E.; Weiss, A.; Kifonidis, K. The core helium flash revisited. II. Two and three-dimensional hydrodynamic simulations. *Astron. Astrophys.* **2009**, *501*, 659–677.
150. Cristini, A.; Hirschi, R.; Meakin, C.; Arnett, D.; Georgy, C.; Walkington, I. Dependence of convective boundary mixing on boundary properties and turbulence strength. *Mon. Not. R. Astron. Soc.* **2019**, *484*, 4645–4664.
151. Staritsin, E.I. Turbulent entrainment at the boundaries of the convective cores of main-sequence stars. *Astron. Rep.* **2013**, *57*, 380–390. [CrossRef]
152. Scott, L.J.A.; Hirschi, R.; Georgy, C.; Arnett, W.D.; Meakin, C.; Kaiser, E.A.; Ekström, S.; Yusof, N. Convective core entrainment in 1D main-sequence stellar models. *Mon. Not. R. Astron. Soc.* **2021**, *503*, 4208–4220.
153. Jermyn, A.S.; Bauer, E.B.; Schwab, J.; Farmer, R.; Ball, W.H.; Bellinger, E.P.; Dotter, A.; Joyce, M.; Marchant, P.; Mombarg, J.S.G.; et al. Modules for Experiments in Stellar Astrophysics (MESA): Time-Dependent Convection, Energy Conservation, Automatic Differentiation, and Infrastructure. *arXiv* **2022**, arXiv:2208.03651.
154. Roxburgh, I.W. Convection and stellar structure. *Astron. Astrophys.* **1978**, *65*, 281–285.
155. Roxburgh, I.W. Limits on convective penetration from stellar cores. *Astron. Astrophys.* **1992**, *266*, 291–293.
156. Kitiashvili, I.N.; Kosovichev, A.G.; Mansour, N.N.; Wray, A.A. Dynamics of Turbulent Convection and Convective Overshoot in a Moderate-mass Star. *Astrophys. J. Lett.* **2016**, *821*, L17.
157. Baraffe, I.; Pratt, J.; Vlaykov, D.G.; Guillet, T.; Goffrey, T.; Le Saux, A.; Constantino, T. Two-dimensional simulations of solar-like models with artificially enhanced luminosity. I. Impact on convective penetration. *Astron. Astrophys.* **2021**, *654*, A126.
158. Singh, H.P.; Roxburgh, I.W.; Chan, K.L. Three-dimensional simulation of penetrative convection: Penetration below a convection zone. *Astron. Astrophys.* **1995**, *295*, 703.
159. Brun, A.S.; Strugarek, A.; Varela, J.; Matt, S.P.; Augustson, K.C.; Emeriau, C.; DoCao, O.L.; Brown, B.; Toomre, J. On Differential Rotation and Overshooting in Solar-like Stars. *Astrophys. J.* **2017**, *836*, 192.
160. Käpylä, P.J.; Korpi, M.J.; Stix, M.; Tuominen, I. Effects of rotation and input energy flux on convective overshooting. In *Convection in Astrophysics*; Kupka, F., Roxburgh, I., Chan, K.L., Eds.; Cambridge University Press: Cambridge, UK, 2007; Volume 239, pp. 437–442.
161. Hotta, H. Solar Overshoot Region and Small-scale Dynamo with Realistic Energy Flux. *Astrophys. J.* **2017**, *843*, 52.
162. Baraffe, I.; Clarke, J.; Morison, A.; Vlaykov, D.G.; Constantino, T.; Goffrey, T.; Guillet, T.; Le Saux, A.; Pratt, J. A study of convective core overshooting as a function of stellar mass based on two-dimensional hydrodynamical simulations. *Mon. Not. R. Astron. Soc.* **2023**, *519*, stad009. [CrossRef]
163. Pope, S.B. *Turbulent Flows*; Cambridge University Press: Cambridge, UK, 2000.
164. Viallet, M.; Meakin, C.; Arnett, D.; Mocák, M. Turbulent Convection in Stellar Interiors. III. Mean-field Analysis and Stratification Effects. *Astrophys. J.* **2013**, *769*, 1.
165. Currie, L.K.; Browning, M.K. The Magnitude of Viscous Dissipation in Strongly Stratified Two-dimensional Convection. *Astrophys. J. Lett.* **2017**, *845*, L17.
166. Julien, K.; Legg, S.; McWilliams, J.; Werne, J. Penetrative convection in rapidly rotating flows: Preliminary results from numerical simulation. *Dyn. Atmos. Ocean.* **1996**, *24*, 237–249. [CrossRef]
167. Julien, K.; Knobloch, E.; Rubio, A.M.; Vasil, G.M. Heat Transport in Low-Rossby-Number Rayleigh-Bénard Convection. *Phys. Rev. Lett.* **2012**, *109*, 254503. [CrossRef]
168. Aurnou, J.M.; Horn, S.; Julien, K. Connections between nonrotating, slowly rotating, and rapidly rotating turbulent convection transport scalings. *Phys. Rev. Res.* **2020**, *2*, 043115.
169. Pal, P.S.; Singh, H.P.; Chan, K.L.; Srivastava, M.P. Turbulent compressible convection with rotation—penetration above a convection zone. *Astrophys. Space Sci.* **2008**, *314*, 231–239.
170. Drobyshevski, E.M.; Yuferev, V.S. Topological pumping of magnetic flux by three-dimensional convection. *J. Fluid Mech.* **1974**, *65*, 33–44. [CrossRef]
171. Tobias, S.M.; Brummell, N.H.; Clune, T.L.; Toomre, J. Transport and Storage of Magnetic Field by Overshooting Turbulent Compressible Convection. *Astrophys. J.* **2001**, *549*, 1183–1203. [CrossRef]

172. Ziegler, U.; Rüdiger, G. Box simulations of rotating magnetoconvection. Effects of penetration and turbulent pumping. *Astron. Astrophys.* **2003**, *401*, 433–442. [CrossRef]
173. Fisher, G.H.; McClymont, A.N.; Chou, D.Y. The Stretching of Magnetic Flux Tubes in the Convective Overshoot Region. *Astrophys. J.* **1991**, *374*, 766. [CrossRef]
174. van Ballegooijen, A.A. The overshoot layer at the base of the solar convective zone and the problem of magnetic flux storage. *Astron. Astrophys.* **1982**, *113*, 99–112.
175. Racine, R. Photometry of M67 to M_{v} = +12. *Astrophys. J.* **1971**, *168*, 393. [CrossRef]
176. Torres-Peimbert, S. On the Ages of the Galactic Clusters NGC 188, M67 AND NGC 6791. *Bol. Obs. Tonantzintla Tacubaya* **1971**, *6*, 3–14.
177. Bell, R.A. The reddening, distance modulus, chemical composition and age of the galactic cluster NGC 752. *Mon. Not. R. Astron. Soc.* **1972**, *157*, 147–156. [CrossRef]
178. McClure, R.D.; Newell, B.; Barnes, J.V. PDS Photometry of the Open Cluster NGC 2420. *Publ. Astron. Soc. Pac.* **1978**, *90*, 170. [CrossRef]
179. Demarque, P.; Sarajedini, A.; Guo, X.J. The Gap in the Color-Magnitude Diagram of NGC 2420: A Test of Convective Overshoot and Cluster Age. *Astrophys. J.* **1994**, *426*, 165. [CrossRef]
180. Maeder, A.; Mermilliod, J.C. The extent of mixing in stellar interiors: Evolutionary models and tests based on the HR diagrams of 34 open clusters. *Astron. Astrophys.* **1981**, *93*, 136–149.
181. Kozhurina-Platais, V.; Demarque, P.; Platais, I.; Orosz, J.A.; Barnes, S. The Age of NGC 3680 and a Test of Convective Overshoot. *Astron. J.* **1997**, *113*, 1045–1056. [CrossRef]
182. Andersen, J.; Clausen, J.V.; Nordstrom, B. New Strong Evidence for the Importance of Convective Overshooting in Intermediate-Mass Stars. *Astrophys. J. Lett.* **1990**, *363*, L33. [CrossRef]
183. Vallenari, A.; Chiosi, C.; Bertelli, G.; Meylan, G.; Ortolani, S. Star clusters of the large magellanic cloud. III. CCD-photometry of NGC 2164. *Astron. Astrophys. Suppl. Ser.* **1991**, *87*, 517–540.
184. Vallenari, A.; Chiosi, C.; Bertelli, G.; Meylan, G.; Ortolani, S. Stars Clusters of the Large Magellanic Cloud: CCD Photometry of NGC 1831. *Astron. J.* **1992**, *104*, 1100. [CrossRef]
185. Chiosi, C.; Bertelli, G.; Meylan, G.; Ortolani, S. Globular clusters in the Large Magellanic Cloud: NGC 1866, a test for convective overshoot. *Astron. Astrophys.* **1989**, *219*, 167–191.
186. Bruntt, H.; Frandsen, S.; Kjeldsen, H.; Andersen, M.I. Strömgren photometry of the open clusters NGC 6134 and NGC 3680. *Astron. Astrophys. Suppl. Ser.* **1999**, *140*, 135–143. [CrossRef]
187. Woo, J.H.; Gallart, C.; Demarque, P.; Yi, S.; Zoccali, M. Testing Intermediate-Age Stellar Evolution Models with VLT Photometry of Large Magellanic Cloud Clusters. II. Analysis with the Yale Models. *Astron. J.* **2003**, *125*, 754–769.
188. Mucciarelli, A.; Origlia, L.; Ferraro, F.R. The Intermediate-Age Globular Cluster NGC 1783 in the Large Magellanic Cloud. *Astron. J.* **2007**, *134*, 1813.
189. Girardi, L.; Rubele, S.; Kerber, L. Discovery of two distinct red clumps in NGC 419: A rare snapshot of a cluster at the onset of degeneracy. *Mon. Not. R. Astron. Soc.* **2009**, *394*, L74–L78.
190. Nordstrom, B.; Andersen, J. Open clusters under the microscope. *Messenger* **1991**, *63*, 34–37.
191. Dinescu, D.I.; Demarque, P.; Guenther, D.B.; Pinsonneault, M.H. The Ages of the Disk Clusters NGC 188, M67, and NGC 752, Using Improved Opacities and Cluster Membership Data. *Astron. J.* **1995**, *109*, 2090. [CrossRef]
192. Michaud, G.; Richard, O.; Richer, J.; VandenBerg, D.A. Models for Solar Abundance Stars with Gravitational Settling and Radiative Accelerations: Application to M67 and NGC 188. *Astrophys. J.* **2004**, *606*, 452–465.
193. Viani, L.; Basu, S. Isochrones of M67 with an Expanded Set of Parameters. *Eur. Phys. J. Web Conf.* **2017**, *160*, 05005.
194. Bressan, A.; Marigo, P.; Girardi, L.; Salasnich, B.; Dal Cero, C.; Rubele, S.; Nanni, A. PARSEC: Stellar tracks and isochrones with the PAdova and TRieste Stellar Evolution Code. *Mon. Not. R. Astron. Soc.* **2012**, *427*, 127–145.
195. Dotter, A. MESA Isochrones and Stellar Tracks (MIST) 0: Methods for the Construction of Stellar Isochrones. *Astrophys. J. Suppl. Ser.* **2016**, *222*, 8.
196. Choi, J.; Dotter, A.; Conroy, C.; Cantiello, M.; Paxton, B.; Johnson, B.D. Mesa Isochrones and Stellar Tracks (MIST). I. Solar-scaled Models. *Astrophys. J.* **2016**, *823*, 102.
197. Johnston, C.; Tkachenko, A.; Aerts, C.; Molenberghs, G.; Bowman, D.M.; Pedersen, M.G.; Buysschaert, B.; Pápics, P.I. Binary asteroseismic modelling: Isochrone-cloud methodology and application to Kepler gravity mode pulsators. *Mon. Not. R. Astron. Soc.* **2019**, *482*, 1231–1246.
198. Johnston, C.; Aerts, C.; Pedersen, M.G.; Bastian, N. Isochrone-cloud fitting of the extended main-sequence turn-off of young clusters. *Astron. Astrophys.* **2019**, *632*, A74.
199. Milone, A.P.; Marino, A.F.; Di Criscienzo, M.; D'Antona, F.; Bedin, L.R.; Da Costa, G.; Piotto, G.; Tailo, M.; Dotter, A.; Angeloni, R.; et al. Multiple stellar populations in Magellanic Cloud clusters - VI. A survey of multiple sequences and Be stars in young clusters. *Mon. Not. R. Astron. Soc.* **2018**, *477*, 2640–2663.
200. Goudfrooij, P.; Girardi, L.; Bellini, A.; Bressan, A.; Correnti, M.; Costa, G. The Minimum Mass of Rotating Main-sequence Stars and its Impact on the Nature of Extended Main-sequence Turnoffs in Intermediate-age Star Clusters in the Magellanic Clouds. *Astrophys. J. Lett.* **2018**, *864*, L3.

201. Milone, A.P.; Bedin, L.R.; Piotto, G.; Anderson, J. Multiple stellar populations in Magellanic Cloud clusters. I. An ordinary feature for intermediate age globulars in the LMC? *Astron. Astrophys.* **2009**, *497*, 755–771.
202. Yang, W.; Meng, X.; Bi, S.; Tian, Z.; Li, T.; Liu, K. The Contributions of Interactive Binary Stars to Double Main-sequence Turnoffs and Dual Red Clump of Intermediate-age Star Clusters. *Astrophys. J. Lett.* **2011**, *731*, L37.
203. Bastian, N.; de Mink, S.E. The effect of stellar rotation on colour-magnitude diagrams: On the apparent presence of multiple populations in intermediate age stellar clusters. *Mon. Not. R. Astron. Soc.* **2009**, *398*, L11–L15.
204. Yang, W.; Tian, Z. The Effects of the Overshooting of the Convective Core on Main-sequence Turnoffs of Young- and Intermediate-age Star Clusters. *Astrophys. J.* **2017**, *836*, 102.
205. Bastian, N.; Kamann, S.; Cabrera-Ziri, I.; Georgy, C.; Ekström, S.; Charbonnel, C.; de Juan Ovelar, M.; Usher, C. Extended main sequence turnoffs in open clusters as seen by Gaia - I. NGC 2818 and the role of stellar rotation. *Mon. Not. R. Astron. Soc.* **2018**, *480*, 3739–3746.
206. Marino, A.F.; Przybilla, N.; Milone, A.P.; Da Costa, G.; D'Antona, F.; Dotter, A.; Dupree, A. Different Stellar Rotations in the Two Main Sequences of the Young Globular Cluster NGC 1818: The First Direct Spectroscopic Evidence. *Astron. J.* **2018**, *156*, 116.
207. Sun, W.; de Grijs, R.; Deng, L.; Albrow, M.D. Stellar Rotation and the Extended Main-sequence Turnoff in the Open Cluster NGC 5822. *Astrophys. J.* **2019**, *876*, 113.
208. Kamann, S.; Bastian, N.; Gossage, S.; Baade, D.; Cabrera-Ziri, I.; Da Costa, G.; de Mink, S.E.; Georgy, C.; Giesers, B.; Göttgens, F.; et al. How stellar rotation shapes the colour-magnitude diagram of the massive intermediate-age star cluster NGC 1846. *Mon. Not. R. Astron. Soc.* **2020**, *492*, 2177–2192.
209. Kamann, S.; Saracino, S.; Bastian, N.; Gossage, S.; Usher, C.; Baade, D.; Cabrera-Ziri, I.; de Mink, S.E.; Ekstrom, S.; Georgy, C.; et al. The effects of stellar rotation along the main sequence of the 100-Myr-old massive cluster NGC 1850. *Mon. Not. R. Astron. Soc.* **2023**, *518*, 1505–1521.
210. von Zeipel, H. The radiative equilibrium of a rotating system of gaseous masses. *Mon. Not. R. Astron. Soc.* **1924**, *84*, 665–683. [CrossRef]
211. Espinosa Lara, F.; Rieutord, M. Gravity darkening in rotating stars. *Astron. Astrophys.* **2011**, *533*, A43.
212. Lipatov, M.; Brandt, T.D.; Gossage, S. Rotational Variation Allows for Narrow Age Spread in the Extended Main-sequence Turnoff of Massive Cluster NGC 1846. *Astrophys. J.* **2022**, *934*, 105.
213. Russell, H.N. On the advance of periastron in eclipsing binaries. *Mon. Not. R. Astron. Soc.* **1928**, *88*, 641–643. [CrossRef]
214. Claret, A.; Gimenez, A. The effect of core overshooting and mass loss on the internal density concentration of main sequence stars. *Astron. Astrophys.* **1991**, *244*, 319.
215. Semeniuk, I.; Paczyński, B. Apsidal Motion in Binary Systems. III. Model Computations. *Acta Astron.* **1968**, *18*, 33.
216. Stothers, R. The apsidal-motion test for models of main-sequence stars. *Astrophys. J.* **1974**, *194*, 651–655. [CrossRef]
217. Mathis, J.S.; Odell, A.P. The apsidal constant and structure of alpha Virginis. *Astrophys. J.* **1973**, *180*, 517. [CrossRef]
218. Odell, A.P. The structure of Alpha Virginis. II. The apsidal constant. *Astrophys. J.* **1974**, *192*, 417–424. [CrossRef]
219. Shobbrook, R.R.; Herbison-Evans, D.; Johnston, I.D.; Lomb, N.R. Light variations in Spica. *Mon. Not. R. Astron. Soc.* **1969**, *145*, 131. [CrossRef]
220. Shobbrook, R.R.; Lomb, N.R.; Herbison-Evans, D. The short period light and velocity variations in Alpha Virginis. *Mon. Not. R. Astron. Soc.* **1972**, *156*, 165. [CrossRef]
221. Smith, M.A. The nonradial oscillations of Spica. I. Two commensurable modes. *Astrophys. J.* **1985**, *297*, 206–223. [CrossRef]
222. Smith, M.A. The non-radial oscillations of Spica. II. A "quasi-toroidal" mode. *Astrophys. J.* **1985**, *297*, 224–232. [CrossRef]
223. Harrington, D.; Koenigsberger, G.; Moreno, E.; Kuhn, J. Line-profile Variability from Tidal Flows in Alpha Virginis (Spica). *Astrophys. J.* **2009**, *704*, 813–830.
224. Tkachenko, A.; Matthews, J.M.; Aerts, C.; Pavlovski, K.; Pápics, P.I.; Zwintz, K.; Cameron, C.; Walker, G.A.H.; Kuschnig, R.; Degroote, P.; et al. Stellar modelling of Spica, a high-mass spectroscopic binary with a β Cep variable primary component. *Mon. Not. R. Astron. Soc.* **2016**, *458*, 1964–1976.
225. Bowman, D.M.; Vandenbussche, B.; Sana, H.; Tkachenko, A.; Raskin, G.; Delabie, T.; Vandoren, B.; Royer, P.; Garcia, S.; Van Reeth, T.; et al. The CubeSpec space mission. I. Asteroseismology of massive stars from time-series optical spectroscopy: Science requirements and target list prioritisation. *Astron. Astrophys.* **2022**, *658*, A96,
226. Claret, A.; Gimenez, A. The apsidal motion test of the internal stellar structure: Comparison between theory and observations. *Astron. Astrophys.* **1993**, *277*, 487–502.
227. Claret, A. The role of the stellar rotation on the internal constitution of PV Cassiopeiae. *Astron. Astrophys.* **2008**, *490*, 1103–1107. [CrossRef]
228. Wolf, M.; Zejda, M.; de Villiers, S.N. Apsidal motion in southern eccentric eclipsing binaries: GL Car, QX Car, NO Pup and V366 Pup. *Mon. Not. R. Astron. Soc.* **2008**, *388*, 1836–1842. [CrossRef]
229. North, P.; Gauderon, R.; Barblan, F.; Royer, F. VLT multi-object spectroscopy of 33 eclipsing binaries in the Small Magellanic Cloud. New distance and depth of the SMC, and a record-breaking apsidal motion. *Astron. Astrophys.* **2010**, *520*, A74.
230. Bulut, İ. Apsidal motion elements of six eccentric eclipsing binaries: V799 Cas, CO Cep, V1136 Cyg, V345 Lac, V364 Lac and V402 Lac. *New Astron.* **2013**, *21*, 22–26. [CrossRef]
231. Zasche, P.; Wolf, M. Apsidal motion and absolute parameters for five LMC eccentric eclipsing binaries. *Astron. Astrophys.* **2013**, *558*, A51,

232. Lacy, C.H.S.; Torres, G.; Fekel, F.C.; Muterspaugh, M.W.; Southworth, J. Absolute Properties of the Eclipsing Binary Star IM Persei. *Astron. J.* **2015**, *149*, 34. [CrossRef]
233. Bakış, V. Young eccentric binary KL CMa revisited in the light of spectroscopy. *New Astron.* **2015**, *40*, 14–19. [CrossRef]
234. Hong, K.; Lee, J.W.; Kim, S.L.; Koo, J.R.; Park, J.H.; Kim, C.H.; Lee, C.U.; Kim, H.W.; Kim, D.J.; Han, C. Absolute Dimensions and Apsidal Motions of Three Binary Systems in the Large Magellanic Cloud. *Astron. J.* **2019**, *158*, 185. [CrossRef]
235. Andersen, J.; Clausen, J.V.; Nordstrom, B.; Popper, D.M. Absolute dimensions of eclipsing binaries. VIII. V760 Scorpii. *Astron. Astrophys.* **1985**, *151*, 329–339.
236. Gimenez, A.; Kim, C.H.; Nha, I.S. Apsidal motion in the early-type eclipsing binaries CW Cephei, Y Cygni and AG Persei. *Mon. Not. R. Astron. Soc.* **1987**, *224*, 543–555. [CrossRef]
237. Bakış, V.; Bakış, H.; Demircan, O.; Eker, Z. Absolute dimensions and apsidal motion of the eccentric binary PT Velorum. *Mon. Not. R. Astron. Soc.* **2008**, *384*, 1657–1667. [CrossRef]
238. Değirmenci, Ö.L.; Gülmen, Ö.; Sezer, C.; Ibanoğlu, C.; Çakırlı, Ö. Up-to-date UBV light and O-C curves analyses of the eclipsing binary V477 Cygni. *Astron. Astrophys.* **2003**, *409*, 959–967. [CrossRef]
239. Bakiş, V.; Bulut, Á.; Bilir, S.; Bakiş, H.; Demircan, O.; Hensberge, H. Absolute Dimensions and Apsidal Motion of the Young Detached System LT Canis Majoris. *Publ. Astron. Soc. Jpn.* **2010**, *62*, 1291–1299.
240. Baroch, D.; Giménez, A.; Morales, J.C.; Ribas, I.; Herrero, E.; Perdelwitz, V.; Jordi, C.; Granzer, T.; Allende Prieto, C. Absolute dimensions and apsidal motion of the eclipsing binaries V889 Aquilae and V402 Lacertae. *Astron. Astrophys.* **2022**, *665*, A13.
241. Claret, A.; Giménez, A.; Baroch, D.; Ribas, I.; Morales, J.C.; Anglada-Escudé, G. Analysis of apsidal motion in eclipsing binaries using TESS data. II. A test of internal stellar structure. *Astron. Astrophys.* **2021**, *654*, A17.
242. Guinan, E.F.; Ribas, I.; Fitzpatrick, E.L.; Giménez, Á.; Jordi, C.; McCook, G.P.; Popper, D.M. Eclipsing Binaries as Astrophysical Laboratories: Internal Structure, Core Convection, and Evolution of the B-Star Components of V380 Cygni. *Astrophys. J.* **2000**, *544*, 409–422.
243. Claret, A. The massive and evolved EBS V380 Cygni: A case of critical evolution. *Astron. Astrophys.* **2003**, *399*, 1115–1119. [CrossRef]
244. Rosu, S.; Rauw, G.; Nazé, Y.; Gosset, E.; Sterken, C. Apsidal motion in massive eccentric binaries: The case of CPD-41° 7742, and HD 152218 revisited. *Astron. Astrophys.* **2022**, *664*, A98.
245. Groenewegen, M.A.T.; Lamers, H.J.G.L.M.; Pauldrach, A.W.A. The winds of O-stars. II. The terminal velocities of stellar winds ofO-type stars. *Astron. Astrophys.* **1989**, *221*, 78–88.
246. Herrero, A.; Kudritzki, R.P.; Vilchez, J.M.; Kunze, D.; Butler, K.; Haser, S. The mass and helium discrepancy in massive young stars. In *The Atmospheres of Early-Type Stars*; Heber, U., Jeffery, C.S., Eds.; Springer: Cham, Switzerland, 1992; Volume 401, p. 21. [CrossRef]
247. Gronbech, B.; Gyldenkerne, K.; Jorgensen, H.E. Four-colour photometry of eclipsing binaries. VII. SZ Cen, light curves, photometric elements, absolute dimensions and determination of helium content. *Astron. Astrophys.* **1977**, *55*, 401–409.
248. Clausen, J.V. Absolute dimensions of eclipsing binaries. XIX. BW Aquarii: A late F-typeindicator of overshooting. *Astron. Astrophys.* **1991**, *246*, 397.
249. Fitzpatrick, E.L.; Garmany, C.D. The H-R Diagram of the Large Magellanic Cloud and Implications for Stellar Evolution. *Astrophys. J.* **1990**, *363*, 119. [CrossRef]
250. Hunter, I.; Lennon, D.J.; Dufton, P.L.; Trundle, C.; Simón-Díaz, S.; Smartt, S.J.; Ryans, R.S.I.; Evans, C.J. The VLT-FLAMES survey of massive stars: Atmospheric parameters and rotational velocity distributions for B-type stars in the Magellanic Clouds. *Astron. Astrophys.* **2008**, *479*, 541–555. .:20078511. [CrossRef]
251. Brott, I.; de Mink, S.E.; Cantiello, M.; Langer, N.; de Koter, A.; Evans, C.J.; Hunter, I.; Trundle, C.; Vink, J.S. Rotating massive main-sequence stars. I. Grids of evolutionary models and isochrones. *Astron. Astrophys.* **2011**, *530*, A115.
252. Vink, J.S.; Brott, I.; Gräfener, G.; Langer, N.; de Koter, A.; Lennon, D.J. The nature of B supergiants: Clues from a steep drop in rotation rates at 22 000 K. The possibility of Bi-stability braking. *Astron. Astrophys.* **2010**, *512*, L7.
253. Pavlovski, K.; Tamajo, E.; Koubský, P.; Southworth, J.; Yang, S.; Kolbas, V. Chemical evolution of high-mass stars in close binaries—II. The evolved component of the eclipsing binary V380Cygni. *Mon. Not. R. Astron. Soc.* **2009**, *400*, 791–804.
254. Tkachenko, A.; Degroote, P.; Aerts, C.; Pavlovski, K.; Southworth, J.; Pápics, P.I.; Moravveji, E.; Kolbas, V.; Tsymbal, V.; Debosscher, J.; et al. The eccentric massive binary V380 Cyg: Revised orbital elements and interpretation of the intrinsic variability of the primary component*. *Mon. Not. R. Astron. Soc.* **2014**, *438*, 3093–3110.
255. Fekel, F.C. Chromospherically Active Stars. VIII. HD 155683 = V972 Herculis: Observational Constraints on Evolutionary Theory. *Astron. J.* **1991**, *101*, 1489. [CrossRef]
256. Andersen, J.; Clausen, J.V.; Nordstrom, B.; Gustafsson, B.; Vandenberg, D.A. Absolute dimensions of eclipsing binaries. XIII. AI Phoenicis: A casestudy in stellar evolution. *Astron. Astrophys.* **1988**, *196*, 128–140.
257. Andersen, J.; Clausen, J.V.; Magain, P. Absolute dimensions of eclipsing binaries. XIV. UX Mensae. *Astron. Astrophys.* **1989**, *211*, 346–352.
258. Claret, A.; Torres, G. The dependence of convective core overshooting on stellar mass. *Astron. Astrophys.* **2016**, *592*, A15. [CrossRef]
259. Schroder, K.P.; Pols, O.R.; Eggleton, P.P. A critical test of stellar evolution and convective core 'overshooting' by means of zeta Aurigae systems. *Mon. Not. R. Astron. Soc.* **1997**, *285*, 696–710. [CrossRef]

260. Ribas, I.; Jordi, C.; Giménez, Á. The mass dependence of the overshooting parameter determined from eclipsing binary data. *Mon. Not. R. Astron. Soc.* **2000**, *318*, L55–L59. [CrossRef]
261. Claret, A. Does convective core overshooting depend on stellar mass?. Tests using double-lined eclipsing binaries. *Astron. Astrophys.* **2007**, *475*, 1019–1025. [CrossRef]
262. Claret, A.; Torres, G. The Dependence of Convective Core Overshooting on Stellar Mass: Reality Check and Additional Evidence. *Astrophys. J.* **2019**, *876*, 134.
263. Costa, G.; Girardi, L.; Bressan, A.; Marigo, P.; Rodrigues, T.S.; Chen, Y.; Lanza, A.; Goudfrooij, P. Mixing by overshooting and rotation in intermediate-mass stars. *Mon. Not. R. Astron. Soc.* **2019**, *485*, 4641–4657.
264. Constantino, T.; Baraffe, I. Significant uncertainties from calibrating overshooting with eclipsing binary systems. *Astron. Astrophys.* **2018**, *618*, A177.
265. Meng, Y.; Zhang, Q.S. Calibrating the Updated Overshoot Mixing Model on Eclipsing Binary Stars: HY Vir, YZ Cas, χ^2 Hya, and VV Crv. *Astrophys. J.* **2014**, *787*, 127.
266. Stancliffe, R.J.; Fossati, L.; Passy, J.C.; Schneider, F.R.N. Confronting uncertainties in stellar physics: Calibrating convective overshooting with eclipsing binaries. *Astron. Astrophys.* **2015**, *575*, A117.
267. Andersen, J. Accurate masses and radii of normal stars. *Astron. Astrophys. Rev.* **1991**, *3*, 91–126. [CrossRef]
268. Valle, G.; Dell'Omodarme, M.; Prada Moroni, P.G.; Degl'Innocenti, S. Calibrating convective-core overshooting with eclipsing binary systems. The case of low-mass main-sequence stars. *Astron. Astrophys.* **2016**, *587*, A16.
269. Valle, G.; Dell'Omodarme, M.; Prada Moroni, P.G.; Degl'Innocenti, S. Statistical errors and systematic biases in the calibration of the convective core overshooting with eclipsing binaries. A case study: TZ Fornacis. *Astron. Astrophys.* **2017**, *600*, A41.
270. Valle, G.; Dell'Omodarme, M.; Prada Moroni, P.G.; Degl'Innocenti, S. Overshooting calibration and age determination from evolved binary systems. A statistical investigation on biases and random variability. *Astron. Astrophys.* **2018**, *615*, A62.
271. Pols, O.R.; Tout, C.A.; Schroder, K.P.; Eggleton, P.P.; Manners, J. Further critical tests of stellar evolution by means of double-lined eclipsing binaries. *Mon. Not. R. Astron. Soc.* **1997**, *289*, 869–881. [CrossRef]
272. Mahy, L.; Sana, H.; Abdul-Masih, M.; Almeida, L.A.; Langer, N.; Shenar, T.; de Koter, A.; de Mink, S.E.; de Wit, S.; Grin, N.J.; et al. The Tarantula Massive Binary Monitoring. III. Atmosphere analysis of double-lined spectroscopic systems. *Astron. Astrophys.* **2020**, *634*, A118.
273. de Mink, S.E.; Cantiello, M.; Langer, N.; Pols, O.R.; Brott, I.; Yoon, S.C. Rotational mixing in massive binaries. Detached short-period systems. *Astron. Astrophys.* **2009**, *497*, 243–253.
274. Martins, F.; Mahy, L.; Hervé, A. Properties of six short-period massive binaries: A study of the effects of binarity on surface chemical abundances. *Astron. Astrophys.* **2017**, *607*, A82.
275. Pavlovski, K.; Southworth, J.; Tkachenko, A.; Van Reeth, T.; Tamajo, E. High-mass eclipsing binaries: A testbed for models of interior structure and evolution—Accurate fundamental properties and surface chemical composition for V1034 Sco, GL Car, V573 Car and V346 Cen. *arXiv* **2023**, arXiv:2301.04215.
276. Graczyk, D.; Pietrzyński, G.; Thompson, I.B.; Gieren, W.; Pilecki, B.; Konorski, P.; Villanova, S.; Górski, M.; Suchomska, K.; Karczmarek, P.; et al. The Late-type Eclipsing Binaries in the Large Magellanic Cloud: Catalog of Fundamental Physical Parameters. *Astrophys. J.* **2018**, *860*, 1.
277. Eker, Z.; Bilir, S.; Soydugan, F.; Gökçe, E.Y.; Soydugan, E.; Tüysüz, M.; Şenyüz, T.; Demircan, O. The Catalogue of Stellar Parameters from the Detached Double-Lined Eclipsing Binaries in the Milky Way. *Publ. Astron. Soc. Aust.* **2014**, *31*, e024.
278. Veramendi, M.E.; González, J.F. Accurate absolute parameters of the binary system V4089 Sgr. *New Astron.* **2015**, *34*, 266–270.
279. Kjurkchieva, D.; Vasileva, D.; Atanasova, T. Orbital Parameters of the Eclipsing Detached Kepler Binaries with Eccentric Orbits. *Astron. J.* **2017**, *154*, 105. [CrossRef]
280. Graczyk, D.; Pietrzyński, G.; Thompson, I.B.; Gieren, W.; Pilecki, B.; Konorski, P.; Udalski, A.; Soszyński, I.; Villanova, S.; Górski, M.; et al. The Araucaria Project. The Distance to the Small Magellanic Cloud from Late-type Eclipsing Binaries. *Astrophys. J.* **2014**, *780*, 59.
281. Pilecki, B.; Graczyk, D.; Pietrzyński, G.; Gieren, W.; Thompson, I.B.; Freedman, W.L.; Scowcroft, V.; Madore, B.F.; Udalski, A.; Soszyński, I.; et al. Physical parameters and the projection factor of the classical Cepheid in the binary system OGLE-LMC-CEP-0227. *Mon. Not. R. Astron. Soc.* **2013**, *436*, 953–967.
282. Pilecki, B.; Graczyk, D.; Gieren, W.; Pietrzyński, G.; Thompson, I.B.; Smolec, R.; Udalski, A.; Soszyński, I.; Konorski, P.; Taormina, M.; et al. The Araucaria Project: The First-overtone Classical Cepheid in the Eclipsing System OGLE-LMC-CEP-2532. *Astrophys. J.* **2015**, *806*, 29.
283. Gieren, W.; Pilecki, B.; Pietrzyński, G.; Graczyk, D.; Udalski, A.; Soszyński, I.; Thompson, I.B.; Prada Moroni, P.G.; Smolec, R.; Konorski, P.; et al. The Araucaria Project: A Study of the Classical Cepheid in the Eclipsing Binary System OGLE LMC562.05.9009 in the Large Magellanic Cloud. *Astrophys. J.* **2015**, *815*, 28.
284. Graczyk, D.; Pietrzyński, G.; Thompson, I.B.; Gieren, W.; Pilecki, B.; Udalski, A.; Soszyński, I.; Kołaczkowski, Z.; Kudritzki, R.P.; Bresolin, F.; et al. The Araucaria Project: An Accurate Distance to the Late-type Double-lined Eclipsing Binary OGLE SMC113.3 4007 in the Small Magellanic Cloud. *Astrophys. J.* **2012**, *750*, 144.
285. Pietrzyński, G.; Graczyk, D.; Gieren, W.; Thompson, I.B.; Pilecki, B.; Udalski, A.; Soszyński, I.; Kozłowski, S.; Konorski, P.; Suchomska, K.; et al. An eclipsing-binary distance to the Large Magellanic Cloud accurate to two per cent. *Nature* **2013**, *495*, 76–79.

286. Torres, G.; Claret, A.; Pavlovski, K.; Dotter, A. Capella (α Aurigae) Revisited: New Binary Orbit, Physical Properties, and Evolutionary State. *Astrophys. J.* **2015**, *807*, 26.
287. Hełminiak, K.G.; Graczyk, D.; Konacki, M.; Pilecki, B.; Ratajczak, M.; Pietrzyński, G.; Sybilski, P.; Villanova, S.; Gieren, W.; Pojmański, G.; et al. Orbital and physical parameters of eclipsing binaries from the ASAS catalogue - VIII. The totally eclipsing double-giant system HD 187669. *Mon. Not. R. Astron. Soc.* **2015**, *448*, 1945–1955.
288. Buzasi, D.; Catanzarite, J.; Laher, R.; Conrow, T.; Shupe, D.; Gautier, T.N.I.; Kreidl, T.; Everett, D. The Detection of Multimodal Oscillations on α Ursae Majoris. *Astrophys. J. Lett.* **2000**, *532*, L133–L136.
289. Walker, G.; Matthews, J.; Kuschnig, R.; Johnson, R.; Rucinski, S.; Pazder, J.; Burley, G.; Walker, A.; Skaret, K.; Zee, R.; et al. The MOST Asteroseismology Mission: Ultraprecise Photometry from Space. *Publ. Astron. Soc. Pac.* **2003**, *115*, 1023–1035. [CrossRef]
290. Auvergne, M.; Bodin, P.; Boisnard, L.; Buey, J.T.; Chaintreuil, S.; Epstein, G.; Jouret, M.; Lam-Trong, T.; Levacher, P.; Magnan, A.; et al. The CoRoT satellite in flight: Description and performance. *Astron. Astrophys.* **2009**, *506*, 411–424.
291. Baglin, A.; Auvergne, M.; Barge, P.; Deleuil, M.; Michel, E.; CoRoT Exoplanet Science Team. CoRoT: Description of the Mission and Early Results. In *Transiting Planets*; Pont, F., Sasselov, D., Holman, M.J., Eds.; Cambridge University Press: Cambridge, UK, 2009; Volume 253, pp. 71–81. [CrossRef]
292. Borucki, W.J.; Koch, D.; Basri, G.; Batalha, N.; Brown, T.; Caldwell, D.; Caldwell, J.; Christensen-Dalsgaard, J.; Cochran, W.D.; DeVore, E.; et al. Kepler Planet-Detection Mission: Introduction and First Results. *Science* **2010**, *327*, 977. [CrossRef]
293. Koch, D.G.; Borucki, W.J.; Basri, G.; Batalha, N.M.; Brown, T.M.; Caldwell, D.; Christensen-Dalsgaard, J.; Cochran, W.D.; DeVore, E.; Dunham, E.W.; et al. Kepler Mission Design, Realized Photometric Performance, and Early Science. *Astrophys. J. Lett.* **2010**, *713*, L79–L86.
294. Howell, S.B.; Sobeck, C.; Haas, M.; Still, M.; Barclay, T.; Mullally, F.; Troeltzsch, J.; Aigrain, S.; Bryson, S.T.; Caldwell, D.; et al. The K2 Mission: Characterization and Early Results. *Publ. Astron. Soc. Pac.* **2014**, *126*, 398.
295. Weiss, W.W.; Rucinski, S.M.; Moffat, A.F.J.; Schwarzenberg-Czerny, A.; Koudelka, O.F.; Grant, C.C.; Zee, R.E.; Kuschnig, R.; Mochnacki, S.; Matthews, J.M.; et al. BRITE-Constellation: Nanosatellites for Precision Photometry of Bright Stars. *Publ. Astron. Soc. Pac.* **2014**, *126*, 573.
296. Ricker, G.R.; Winn, J.N.; Vanderspek, R.; Latham, D.W.; Bakos, G.Á.; Bean, J.L.; Berta-Thompson, Z.K.; Brown, T.M.; Buchhave, L.; Butler, N.R.; et al. Transiting Exoplanet Survey Satellite (TESS). *J. Astron. Telesc. Instrum. Syst.* **2015**, *1*, 014003. [CrossRef]
297. Aerts, C.; Christensen-Dalsgaard, J.; Kurtz, D.W. *Asteroseismology*; Springer: Cham, Switzerland, 2010. [CrossRef]
298. Chaplin, W.J.; Miglio, A. Asteroseismology of Solar-Type and Red-Giant Stars. *Annu. Rev. Astron. Astrophys.* **2013**, *51*, 353–392. [CrossRef]
299. Aerts, C.; Mathis, S.; Rogers, T.M. Angular Momentum Transport in Stellar Interiors. *Annu. Rev. Astron. Astrophys.* **2019**, *57*, 35–78.
300. Bowman, D.M. Asteroseismology of high-mass stars: New insights of stellar interiors with space telescopes. *Front. Astron. Space Sci.* **2020**, *7*, 70.
301. Holdsworth, D.L. The roAp Stars Observed by the Kepler Space Telescope. *Front. Astron. Space Sci.* **2021**, *8*, 31.
302. Christensen-Dalsgaard, J. Solar structure and evolution. *Living Rev. Sol. Phys.* **2021**, *18*, 2.
303. Aerts, C. Probing the interior physics of stars through asteroseismology. *Rev. Mod. Phys.* **2021**, *93*, 015001.
304. Guzik, J.A. Highlights of Discoveries for δ Scuti Variable Stars From the Kepler Era. *Front. Astron. Space Sci.* **2021**, *8*, 55.
305. Kurtz, D.W. Asteroseismology Across the Hertzsprung-Russell Diagram. *Annu. Rev. Astron. Astrophys.* **2022**, *60*, 31–71. [CrossRef]
306. Houdek, G.; Gough, D.O. An asteroseismic signature of helium ionization. *Mon. Not. R. Astron. Soc.* **2007**, *375*, 861–880.
307. Roxburgh, I.W.; Vorontsov, S.V. Acoustic wave reflection by stellar cores: Can it be seen in the autocorrelation function of p-mode measurements? *Mon. Not. R. Astron. Soc.* **2007**, *379*, 801–806. [CrossRef]
308. Cunha, M.S.; Metcalfe, T.S. Asteroseismic Signatures of Small Convective Cores. *Astrophys. J.* **2007**, *666*, 413–422.
309. Cunha, M.S.; Brandão, I.M. Probing tiny convective cores with the acoustic modes of lowest degree. *Astron. Astrophys.* **2011**, *529*, A10.
310. Silva Aguirre, V.; Basu, S.; Brandão, I.M.; Christensen-Dalsgaard, J.; Deheuvels, S.; Doğan, G.; Metcalfe, T.S.; Serenelli, A.M.; Ballot, J.; Chaplin, W.J.; et al. Stellar Ages and Convective Cores in Field Main-sequence Stars: First Asteroseismic Application to Two Kepler Targets. *Astrophys. J.* **2013**, *769*, 141.
311. Deheuvels, S.; Michel, E.; Goupil, M.J.; Marques, J.P.; Mosser, B.; Dupret, M.A.; Lebreton, Y.; Pichon, B.; Morel, P. Survival of a convective core in low-mass solar-like pulsator HD 203608. *Astron. Astrophys.* **2010**, *514*, A31.
312. Roxburgh, I.W. Present Problems of the Solar Interior. *Sol. Phys.* **1985**, *100*, 21. [CrossRef]
313. Mowlavi, N. A peculiar effect of core overshooting on the internal structure of low mass stars. In *IAU Colloq. 137: Inside the Stars*; Weiss, W.W., Baglin, A., Eds.; Astronomical Society of the Pacific Conference Series; Astronomical Society of the Pacific: San Francisco, CA, USA, 1993; Volume 40, p. 454.
314. Moździerski, D.; Pigulski, A.; Kołaczkowski, Z.; Michalska, G.; Kopacki, G.; Carrier, F.; Walczak, P.; Narwid, A.; Stęślicki, M.; Fu, J.N.; et al. Ensemble asteroseismology of pulsating B-type stars in NGC 6910. *Astron. Astrophys.* **2019**, *632*, A95.
315. Deheuvels, S.; Brandão, I.; Silva Aguirre, V.; Ballot, J.; Michel, E.; Cunha, M.S.; Lebreton, Y.; Appourchaux, T. Measuring the extent of convective cores in low-mass stars using Kepler data: Toward a calibration of core overshooting. *Astron. Astrophys.* **2016**, *589*, A93.

316. Bellinger, E.P.; Angelou, G.C.; Hekker, S.; Basu, S.; Ball, W.H.; Guggenberger, E. Fundamental Parameters of Main-Sequence Stars in an Instant with Machine Learning. *Astrophys. J.* **2016**, *830*, 31. [CrossRef]
317. Mombarg, J.S.G.; Van Reeth, T.; Aerts, C. Constraining stellar evolution theory with asteroseismology of γ Doradus stars using deep learning. Stellar masses, ages, and core-boundary mixing. *Astron. Astrophys.* **2021**, *650*, A58. [CrossRef]
318. Dupret, M.A.; Thoul, A.; Scuflaire, R.; Daszyńska-Daszkiewicz, J.; Aerts, C.; Bourge, P.O.; Waelkens, C.; Noels, A. Asteroseismology of the β Cep star HD 129929. II. Seismic constraints on core overshooting, internal rotation and stellar parameters. *Astron. Astrophys.* **2004**, *415*, 251–257. .:20034143. [CrossRef]
319. Ausseloos, M.; Scuflaire, R.; Thoul, A.; Aerts, C. Asteroseismology of the β Cephei star ν Eridani: Massive exploration of standard and non-standard stellar models to fit the oscillation data. *Mon. Not. R. Astron. Soc.* **2004**, *355*, 352–358. [CrossRef]
320. Mazumdar, A.; Briquet, M.; Desmet, M.; Aerts, C. An asteroseismic study of the β Cephei star β Canis Majoris. *Astron. Astrophys.* **2006**, *459*, 589–596. .:20064980. [CrossRef]
321. Briquet, M.; Morel, T.; Thoul, A.; Scuflaire, R.; Miglio, A.; Montalbán, J.; Dupret, M.A.; Aerts, C. An asteroseismic study of the β Cephei star θ Ophiuchi: Constraints on global stellar parameters and core overshooting. *Mon. Not. R. Astron. Soc.* **2007**, *381*, 1482–1488.
322. Desmet, M.; Briquet, M.; Thoul, A.; Zima, W.; De Cat, P.; Handler, G.; Ilyin, I.; Kambe, E.; Krzesinski, J.; Lehmann, H.; et al. An asteroseismic study of the β Cephei star 12 Lacertae: Multisite spectroscopic observations, mode identification and seismic modelling. *Mon. Not. R. Astron. Soc.* **2009**, *396*, 1460–1472.
323. Aerts, C.; Briquet, M.; Degroote, P.; Thoul, A.; van Hoolst, T. Seismic modelling of the β Cephei star HD 180642 (V1449 Aquilae). *Astron. Astrophys.* **2011**, *534*, A98.
324. Briquet, M.; Aerts, C.; Baglin, A.; Nieva, M.F.; Degroote, P.; Przybilla, N.; Noels, A.; Schiller, F.; Vučković, M.; Oreiro, R.; et al. An asteroseismic study of the O9V star HD 46202 from CoRoT space-based photometry. *Astron. Astrophys.* **2011**, *527*, A112.
325. Briquet, M.; Neiner, C.; Aerts, C.; Morel, T.; Mathis, S.; Reese, D.R.; Lehmann, H.; Costero, R.; Echevarria, J.; Handler, G.; et al. Multisite spectroscopic seismic study of the β Cep star V2052 Ophiuchi: Inhibition of mixing by its magnetic field. *Mon. Not. R. Astron. Soc.* **2012**, *427*, 483–493.
326. Walczak, P.; Daszyńska-Daszkiewicz, J.; Pamyatnykh, A.A.; Zdravkov, T. The hybrid B-type pulsator γ Pegasi: Mode identification and complex seismic modelling. *Mon. Not. R. Astron. Soc.* **2013**, *432*, 822–831.
327. Moravveji, E.; Aerts, C.; Pápics, P.I.; Triana, S.A.; Vandoren, B. Tight asteroseismic constraints on core overshooting and diffusive mixing in the slowly rotating pulsating B8.3V star KIC 10526294. *Astron. Astrophys.* **2015**, *580*, A27.
328. Schmid, V.S.; Aerts, C. Asteroseismic modelling of the two F-type hybrid pulsators KIC 10080943A and KIC 10080943B. *Astron. Astrophys.* **2016**, *592*, A116.
329. Daszyńska-Daszkiewicz, J.; Pamyatnykh, A.A.; Walczak, P.; Colgan, J.; Fontes, C.J.; Kilcrease, D.P. Interpretation of the BRITE oscillation data of the hybrid pulsator ν Eridani: A call for the modification of stellar opacities. *Mon. Not. R. Astron. Soc.* **2017**, *466*, 2284–2293.
330. Sánchez Arias, J.P.; Córsico, A.H.; Althaus, L.G. Asteroseismology of hybrid δ Scuti-γ Doradus pulsating stars. *Astron. Astrophys.* **2017**, *597*, A29.
331. Buysschaert, B.; Aerts, C.; Bowman, D.M.; Johnston, C.; Van Reeth, T.; Pedersen, M.G.; Mathis, S.; Neiner, C. Forward seismic modeling of the pulsating magnetic B-type star HD 43317. *Astron. Astrophys.* **2018**, *616*, A148.
332. Aerts, C.; Pedersen, M.G.; Vermeyen, E.; Hendriks, L.; Johnston, C.; Tkachenko, A.; Pápics, P.I.; Debosscher, J.; Briquet, M.; Thoul, A.; et al. Combined asteroseismology, spectroscopy, and astrometry of the CoRoT B2V target HD 170580. *Astron. Astrophys.* **2019**, *624*, A75.
333. Khalack, V.; Lovekin, C.; Bowman, D.M.; Kobzar, O.; David-Uraz, A.; Paunzen, E.; Sikora, J.; Lenz, P.; Kochukhov, O.; Holdsworth, D.L.; et al. Rotational and pulsational variability in the TESS light curve of HD 27463. *Mon. Not. R. Astron. Soc.* **2019**, *490*, 2102–2111.
334. Hendriks, L.; Aerts, C. Deep Learning Applied to the Asteroseismic Modeling of Stars with Coherent Oscillation Modes. *Publ. Astron. Soc. Pac.* **2019**, *131*, 108001.
335. Wu, T.; Li, Y. High-precision Asteroseismology in a Slowly Pulsating B Star: HD 50230. *Astrophys. J.* **2019**, *881*, 86.
336. Fedurco, M.; Paunzen, E.; Hümmerich, S.; Bernhard, K.; Parimucha, Š. Pulsational properties of ten new slowly pulsating B stars. *Astron. Astrophys.* **2020**, *633*, A122.
337. Wu, T.; Li, Y.; Deng, Z.m.; Lin, G.f.; Song, H.f.; Jiang, C. Asteroseismic Analyses of Slowly Pulsating B Star KIC 8324482: Ultraweak Element Mixing beyond the Central Convective Core. *Astrophys. J.* **2020**, *899*, 38. [CrossRef]
338. Pedersen, M.G. On the Diversity of Mixing and Helium Core Masses of B-type Dwarfs from Gravity-mode Asteroseismology. *Astrophys. J.* **2022**, *930*, 94.
339. Niemczura, E.; Walczak, P.; Mikołajczyk, P.; Schöller, M.; Hummel, C.A.; Hubrig, S.; Różański, T. Seismic modelling of the pulsating mercury-manganese star HD 29589. *Mon. Not. R. Astron. Soc.* **2022**, *514*, 5640–5658. [CrossRef]
340. Szewczuk, W.; Walczak, P.; Daszyńska-Daszkiewicz, J.; Moździerski, D. Seismic modelling of a very young SPB star - KIC 8264293. *Mon. Not. R. Astron. Soc.* **2022**, *511*, 1529–1543.
341. Pedersen, M.G. Internal Rotation and Inclinations of Slowly Pulsating B Stars: Evidence of Interior Angular Momentum Transport. *Astrophys. J.* **2022**, *940*, 49.
342. Angelou, G.C.; Bellinger, E.P.; Hekker, S.; Mints, A.; Elsworth, Y.; Basu, S.; Weiss, A. Convective boundary mixing in low- and intermediate-mass stars - I. Core properties from pressure-mode asteroseismology. *Mon. Not. R. Astron. Soc.* **2020**, *493*, 4987–5004.

343. Lecoanet, D.; Bowman, D.M.; Van Reeth, T. Asteroseismic inference of the near-core magnetic field strength in the main-sequence B star HD 43317. *Mon. Not. R. Astron. Soc.* **2022**, *512*, L16–L20.
344. Pedersen, M.G.; Aerts, C.; Pápics, P.I.; Rogers, T.M. The shape of convective core overshooting from gravity-mode period spacings. *Astron. Astrophys.* **2018**, *614*, A128.